OPTICAL AND MAGNETIC PROPERTIES OF RARE EARTH DOPED α-Fe_2O_3 FOR FUTURE BIO-IMAGING APPLICATIONS

by

LANGUTANI EULENDA MATHEVULA

Submitted in accordance with the requirements for
the degree of

DOCTOR OF PHILOSOPHY

in the subject

Physics

at the

UNIVERSITY OF SOUTH AFRICA

SUPERVISOR: Prof M. S Dhlamini

CO-SUPERVISOR: Prof B. M Mothudi

April 2018

DECLARATION

"I declare that **optical and magnetic properties of rare earth doped α-Fe_2O_3 for future bio-imaging applications** is my own work and that all the sources that I have used or quoted have been indicated and acknowledged by means of complete references".

April 2018

_____ _____

SIGNATURE DATE

DEDICATION

This thesis is dedicated to my mother Tsakani Joyce Mahlaule, who has given me support ever since I started with school and never give up. Na mi rhandza mhani.

AKNOWLEDGEMENT

Firstly, I thank GOD Almighty for giving me the strength to even start the project. It was by his grace and favour that I get to finish the project, as nothing is impossible with him.

The project was made, financially successful by the National Research Foundation (NRF) and the University of South Africa. Thank you for funding me to conduct the project.

The project wouldn't be completed if it wasn't for my supervisor, Prof M.S Dhlamini (UNISA). Thank you for accepting me as your student and believing in me to finish the project. Your constant guidance is really appreciated.

I appreciate the support from my co-supervisor Prof B.M Mothudi (UNISA), thank you very much for your guidance throughout the project.

I greatly appreciate the support from Dr L. L. Noto for working with me and helping me with data interpretation. I thank you for the skills you have instilled in me to interpret data and also your suggestions on the project to be successful.

I would also like to use this opportunity to express my gratitude to the following people:
Prof M.L Lekala, Chair of Physics department, for welcoming me to the department, making me feel at home and ensuring my studies go smoothly.
Prof S. Ray, for your assistance with XPS.
Dr P.S Mbule, for assisting in sol-gel synthesis technique.
Dr M. Khenfouch, for assisting with XRD.
Dr S. Sarma, for assisting with FTIR and Microwave synthesis technique.
Prof T. Kroon (University of Free State), for assisting with the up-conversion measurements, I greatly appreciative your patience with the measurements.

Thank you to fellow students for your contribution to my work, our discussions really made a great impact on the project.

Lastly, I would like to thank my family, especially my mother Tsakani Mahlaule. Thank you so much for your undying support throughout my life. Your support has really made me to work hard to achieve my goal and not disappoint you. To my late grandparents, you have shown us that education is key to success; I have made it thus far because of your constant reminder that one need to be educated. To my siblings Khensani, Nkateko and Mbuyelo, thank you for your support, thank you for being my friends and encouraging me not to give up and allowing me to be a role model to you. To all my relatives, thank you for your support. It was not easy at all, but GOD has saw us through, Thank you, Ndza khensa swinene.

ABSTRACT

Imaging techniques have been developed for decades for the detection of biomolecules in biomedicine cells, in vitro or in living cells and organisms. The application however, often constrained by the available probes, whose optical properties may limit the imaging possibilities. It is very essential to improve the sensitivity of these devices by enhancing efficiency to detection. Recently, Fe_3O_4 has been used primarily in cancer theranostic application such as magnetic resonance imaging (MRI). However, its toxicity towards normal cells has been pointed out by scientific communities, when they are involved in in vitro (helics) cancer treatment. In this work, we have chosen to use α-Fe_2O_3, because it has proven to be less toxic than Fe_3O_4. Hematite is antiferromagnetic (AFM) at room temperature with a small canted moment lying within the crystal symmetry plane. At low temperature, hematite undergoes a magnetic phase transition from weak ferromagnetic (WFM) to a pure antiferromagnetic configuration (AF), which is known as the Morin transition. This magnetic property makes it possible for hematite to be applied in imaging technique. To enhance the optical properties, the α-Fe_2O_3 is doped with lanthanide ions due to their unique optical properties. Incorporation of these rare earth ions, enable the α-Fe_2O_3 to have enhance luminescence properties.

These lanthanide-doped nanoparticles (UCNPs) undergoes up-conversion process which have remarkable ability to combine two or more low energy photons to generate a singly high energy photon by an anti-stokes process and hold great promise for bio-imaging. These nanoparticles exhibit excellent photostability, continuous emission capability and sharp multi-peak line emission. With near infrared excitation, light scattering by biological tissues is substantially reduced. α-Fe_2O_3 have been singly and co-doped with Holmium, Thulium, and Ytterbium by both sol-gel and microwave methods. The doping of these lanthanides have shown improved luminescent properties of α-Fe_2O_3. The up-conversion has been observed from co-doping Thulium and Ytterbium. This work is a proof of concept to show the up-conversion in α-Fe_2O_3. However, the up-conversion intensity is low about 200000 CPS maximum observed, this could be due to the nature of the host structure quenching the luminescence. There is rather, a need to increase the intensity for the maximum application to be achieved.

KEYWORDS

α-Fe_2O_3, Intrinsic defect, Extrinsic defect, sol-gel, microwave, band gap, Thermoluminescence, Lanthanides, photoluminescence, up-conversion, magnetic properties

TABLE OF CONTENT

LIST OF FIGURES

List of Tables

Chapter1: Literature Review

1.1 The Iron oxide

1.1.1 Introduction

The field of nanostructured materials has been growing steady during recent years. In the area such as processing, an important progress has been made that allow the production of large quantities of materials, and a more precise control of chemical structure [1]. Metal oxides plays a very important role in many areas of chemistry, physics and material science. Oxides of compounds with a large diversity are formed from these metal elements. A vast number of structural geometries with an electronic structure that can exhibit metallic, semiconductor or insulator character can be adopted from these metal oxides. In the field of nanotechnology, the goal is to make nanostructures or nanoarrays with special properties with respect to those of bulk or single particle species [2].

These nanostructured materials are solids composed of structural elements, mostly crystallites, with characteristic size of few nanometers [3]. When the particle size decreases to the sub-micrometer regime, the physical and chemical properties of these solids changes. The relative number of atoms at the surfaces and interferences increases with decreasing size, making surface effects very important in small solids. The properties of intergranular matter are often vastly different from normal bulk matter. The lattice constants also changes when the size decreases, even though these changes are small they often lead to important modifications in many physical properties [4]. Many oxides exhibit this phenomenon i.e. ZnO, VO_2, Fe_2O_3, ZrO_2, Al_2O_3, TiO_2 etc. In our work we focus on iron oxide (α-Fe_2O_3).

Iron oxides are common compounds, which are widespread in nature and can be readily synthesized in the laboratory. For centuries magnetic iron oxides have served humans, where the application of small iron oxide nanoparticles as contrast agents for in vitro (helix) diagnosis has been practiced for nearly half a century [5]. Iron oxides are one of the most important transition metal oxides of technological importance. It has sixteen pure phases. These are $Fe(OH)_3$, $Fe(OH)_2$,

$Fe_5HO_8 \cdot 4H_2O$, Fe_3O_4, FeO, five polymorphs of FeOOH and four of Fe_2O_3. The trivalent state, low stability and brilliant colors are the interesting characteristics of these compounds. $Fe_8O_8(OH)(SO_4) \cdot nH_2O$ and $(Fe^{3+})_2O_3 \cdot 0.5H_2O$ are poorly crystalline whereas all the rest of iron oxide are crystalline [6]. Of all the iron oxides α-Fe_2O_3, γ-Fe_2O_3, β-Fe_2O_3 and Fe_3O_4 are the most studied. α-Fe_2O_3 (Hematite), shown in Fig 1.1 is the most stable iron oxide under ambient conditions [7].

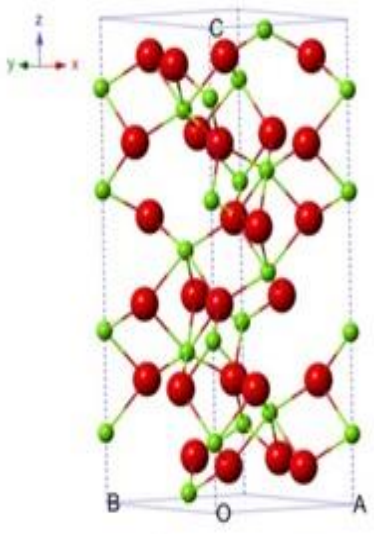

Figure 1. 1 Crystal structure and crystallographic data of Hematite (green ball is Fe^{3+} and red ball is O^{2-}) [5].

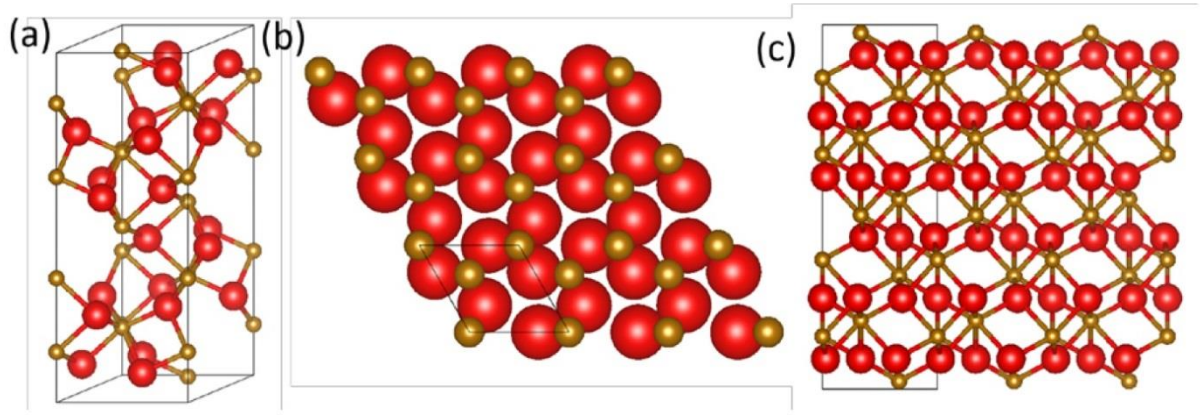

Figure 1. 2 Hematite. (a) The hexagonal unit cell of α-Fe_2O_3 contains 6 formula units. O^{2-} anions are red, Fe_{oct}^{3+} cations are brown. (b) $Feoct^{3+}$ cations occupy two thirds of the octahedral interstitial sites between hexagonal close packed O^{2-} planes (drawn in space filling style with unit cell indicated). (c) Side view of the α-Fe_2O_3 structure that shows how the Fe_{oct}^{3+} cations are not coplanar [8].

α-Fe_2O_3 is isostructural with corundum, α-AlO_3. It has a hexagonal unit cell with a = 0.5034 nm and c = 1.375 nm. There are six formula units per unit cell. The miller indices are (hkil) in the hexagonal symmetry, where i may be replaced by a dot as h + k = -i. The indexing of hematite may also be a rhombohedral system. a_{rh} = 0.5427 nm and α = 55.3° and there are two formula units per cell for rhombohedral system [9]. Since the structure is similar to that of the corundum, it consists of a dense arrangement of Fe^{3+} ions in octahedral coordination with oxygen in hexagonal closed-packing. In addition, the structure can be described as the stacking of sheets of octahedraly coordinated Fe^{3+} ions between two closed-packed layers of oxygen. Each of the oxygen is bonded to only two Fe ions since Fe is in a trivalent state, only two out of three available oxygen octahedrons are occupied. For the structure to be neutral with no charge excess or deficit, this arrangement is essential. The strong covalent bonds are the one that hold together the Fe-O sheets [6].

1.1.2 Magnetic Properties

The iron atom has a strong magnetic moment due to four unpaired electrons (Fe=$4s^2 5d^6$) in its 3*d* orbitals. When crystals are formed from iron atoms, different magnetic states can arise. In paramagnetic state, the individual atomic magnetic moments are randomly aligned with respect to each other, and the crystal has a zero net magnetic moment. If this crystal is subjected to an external magnetic field, some of these moments will align, and the crystal will attain a small net magnetic moment. In a ferromagnetic crystal, all the individual moments are aligned even without an external field. A ferrimagnetic crystal, on the other hand, has a net magnetic moment from two types of atoms with moments of different strengths that are arranged in an antiparallel fashion. If the antiparallel magnetic moments are of the same magnitude, then the crystal is antiferromagnetic and possesses no net magnetic moment, these different magnetic moments are shown in figure 1.3 [10].

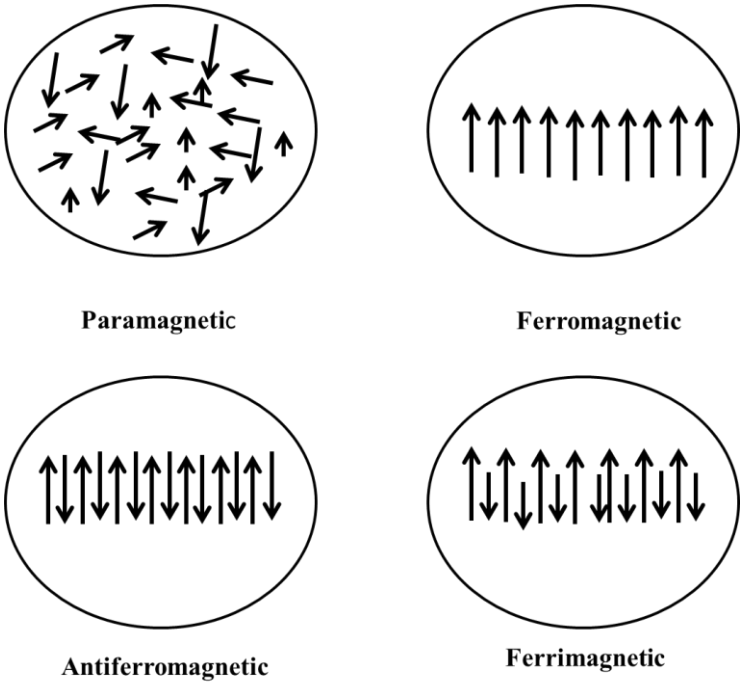

Figure 1. 3 Alignment of individual atomic magnetic moments in different types of materials [10].

Microscopically crystalline α-Fe_2O_3 (hematite) has the corundum crystal structure. It orders anti-ferromagnetically at its Neel temperature T_N (948 < T< 963 K) and it undergoes a spin-flip transition at the Morin temperature, T_M = 263 K: between T_N and T_M α-Fe_2O_3 is a canted antiferromagnet with the spin perpendicular to the trigonal axis, except for a slight canting out of the basal plane, which results in a small net magnetic moments (weak ferromangnetism). Below T_M, the spins lie along the axis and the material behaves as a pure uniaxial antiferromagnet [11]. Bulk magnetite is a ferromagnetic spinel with a high curie temperature of 858 K at $T_c \approx 125$ K. The bulk Fe_3O_4 shows electrical, magnetic and other anomalies, which indicate a phase transition known as the Verwey transition. Also Fe_3O_4 has an isotropic point at 130 K where the first magneto crystalline anisotropy K_1 passes through zero [12]. Maghemite is ferromagnetic at room temperature, unsuitable at high temperatures, and loses its susceptibility with time. However, it can be stabilized by doping with other metal ions. Its curie temperature is difficult to determine experimentally because maghemite undergoes an irreversible crystallographic change to hematite at ~ 673.15K, with a consequent dramatic loss of magnetization. However, the Curie temperature is believed to be between 820 K and 986 K. Maghemite particles smaller than 10 nm are superparamagnetic at room temperature. Aggregation of ultrafine maghemite particles sometimes

leads to magnetic coupling between particles and ordering of magnetic moment, which is termed superferromagnetism [10]. Maghemite nanoparticles are the best candidates as base elements for designing molecular or cellular imaging contrast agent: their transverse relaxivity is far greater than for any other compounds and each targeted particle contains many thousands of iron atoms [13]. On the other hand, hematite has the striking optical properties, its color, which was known for years but not studied in details until the work by Kerker et al [14]. for colloidal hematite. Hund, Ryde and Matijevic correlated the color to particle size and shape [15]

1.1.3 Optical Properties

The variety of colors exhibited by the iron oxides result from different types of electronic transitions [16]. The red and yellow iron oxides absorb strongly in the UV region and are weakly absorbing in the visible/near IR region. The optical spectra of the iron oxides from the diffusely reflected radiation in the UV-VIS-NIR range cover the range between 200 and 1000 nm. Structural and other properties are reflected in these spectra. They are the results of three types of electronic transitions: (1) Fe^{III} crystal to ligand field transitions, (2) interactions between magnetically coupled Fe^{III} ions and (3) ligand (oxygen)-metal charge transfer excitation from the O (2p) non-bonding valence band to the Fe (3d) ligand field orbitals, or in some cases between Fe^{II} and Fe^{III}. The vivid colors of most of the iron oxides are caused by the absorption in the visible region [9].

Excitation from the ground state $^6A_1$ to the excited ligand field state is involved in the ligand field (d-d) transition. These transitions are spin forbidden and are tend to be weak. Because of the magnetic coupling of the next to the nearest neighbor Fe^{III} in the crystal structure, iron oxide intensities are high. The coupling could also lead to simultaneous excitation of two cationic centers by one photon [17]. The transitions mainly responsible for absorption of visible light is the charge transfer transitions involving Fe^{III} – O or Fe^{II} – Fe^{III}. The absorption band produced is centered in the near UV, one side of which extends into the visible region. The overlain of the band in the visible is due to the ligand field transition (between 550 and 900 nm) and double excitation processes at 450 nm. Owing to the interaction between the Fe^{III} – Fe^{II} pairs the d-d transitions are the one that contribute more to the color of iron oxides than would be expected [9].

P. Mallick and B. N. Dash reported on the UV-Visible of α-Fe_2O_3 nanoparticles annealed at different temperatures, shown in Fig 1.4. The spectrum was divided into three regions: region I

(250 – 400 nm), region II (400 – 600 nm) and region III (600 – 780 nm). Region I is attributed to the ligand-to-metal charge-transfer (LMCT) transitions (direct transitions) with combined contributions from the Fe^{3+} ligand field transitions $^6A_1(^6S)$ to $^4T_1(^4P)$ at 290–310 nm, $^6A1(^6S)$ to $^4E(^4D)$ and $^6A1(^6S)$ to $^4T_1(^4D)$ at 360–380 nm. The absorption band in region II is associated with the double excitation processes of $^6A1(^6S)+^6A_1(^6S)$ to $^4T_1(^4G)+^4T1(^4G)$ at 485–550 nm, and is most likely overlapped by the contributions from $^6A_1(^6S)$ to ^4E, $^4A_1(^4G)$ ligand field transitions at 430 nm and the charge-transfer band tail. This inter-band transition is primarily responsible for the red colour of hematite. Region III corresponds to the $^6A_1(^6S)$ to $^4T_2(^4G)$ ligand field transition at about 640 nm [7]. Iron oxide can be doped with metals or rare earth ions, thereby introducing defects into the material.

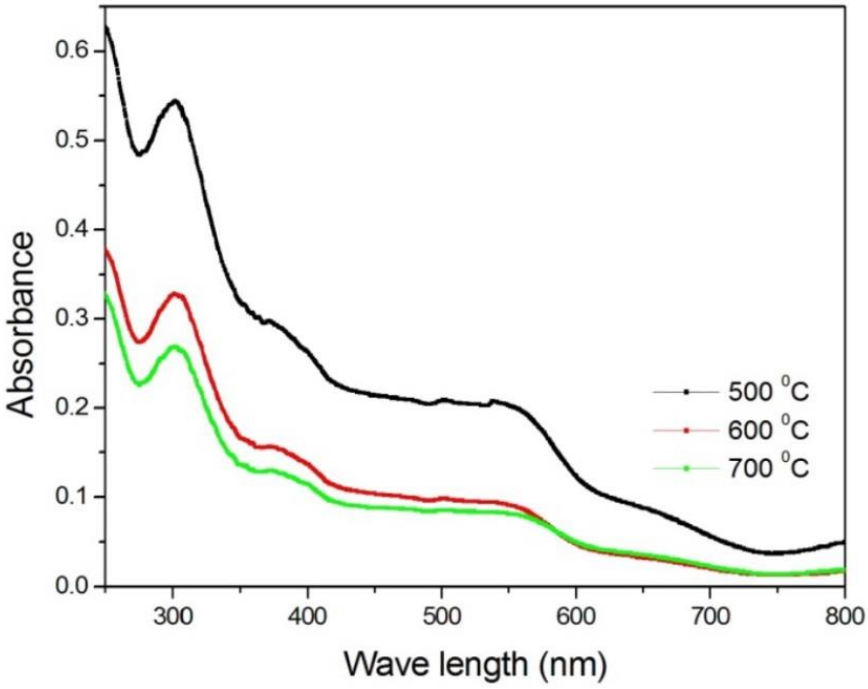

Figure 1. 4 Variation of absorption coefficient of α -Fe_2O_3 nanoparticles annealed at 500, 600 and 700 ℃ with wavelength [7].

1.1.4 Point defects of α-Fe_2O_3

Hematite has an indirect band gap of ≈ 2.2 eV that is of d-d origin, and a direct optical gap of 2.7 eV. Dieckmann in 1993 [8] reviewed the knowledge of point defects and diffusion in α-Fe_2O_3, where it was concluded that oxygen vacancies are dominant defects between 1373 K and 1573 K. A tracer diffusion of ^{57}Fe and ^{18}O measurements revealed that oxygen diffusion is faster than that

of Fe. Catlon et.al proposed that electronic disorder outweighs ionic diffusion and is responsible for electric conductivity; however, in general it seems that both V_o and interstitial Fe can form. V_o, which leads to enhanced carrier concentration, has been a defective α-Fe_2O_3, which was prepared under poor O_2 environment. It has been concluded that these defects are most likely responsible for charge carriers under ambient condition, since Fe interstitial and vacancies form donor and acceptors states, respectively [8]. Joohee Lee and Seungwu Han investigated native point defects in Fe_2O_3 theoretically using ab initio method based on the GGA + U formation. Vacancies and interstitial of Fe and O atoms were considered as well as the electron polaron as Fe^{II} defects as the host Fe^{III} site. The Fe interstitial and O vacancy were found to form donor and acceptor levels close to band edges, respectively, thereby allowing for charge carrier at room temperature. Oxygen deficiency under high temperature equilibrium conditions was further determined and find excellent agreement with experimental. The oxygen vacancy is mostly neutral and the Fe interstitial is responsible for electron carriers [18].

1.2 Band gap theory of semiconductors

When a compound is formed by atoms coming together, their atom orbital energies mix to form molecular orbital energies. As more atoms begin to mix and more molecular orbitals are formed, many of these energy levels are expected to be very close to each other, or even completely degenerate, in energy. Therefore, a band of energy is formed by these energy levels. A semiconductor will actually act as insulator at absolute zero according to band theory. It will then act as a semiconductor above the absolute zero temperature and yet still staying below the melting point of the solid. A semiconductor is known by the fully occupied valence band and unoccupied conduction band as shown in Fig 1.5, with the small gap between these bands. It takes certain amount of energy to excite an electron from the valence band to conduction band. Upon irradiation by photons with greater energy than the band gap, an electron in a semiconductor will be promoted from the valence band, leaving a ‘hole’ in a valence band. The ‘hole’ will therefore behave as a ‘particle’ with a certain effective mass and positive charge. The band state of the electron-hole pair is called ‘exciton’ [19]. Luis Brus has developed the relation between the size and the band gap energy of semiconductor nanocrystals by applying the particle in sphere model approximation to the bulk Wannier Hamiltonian [20].

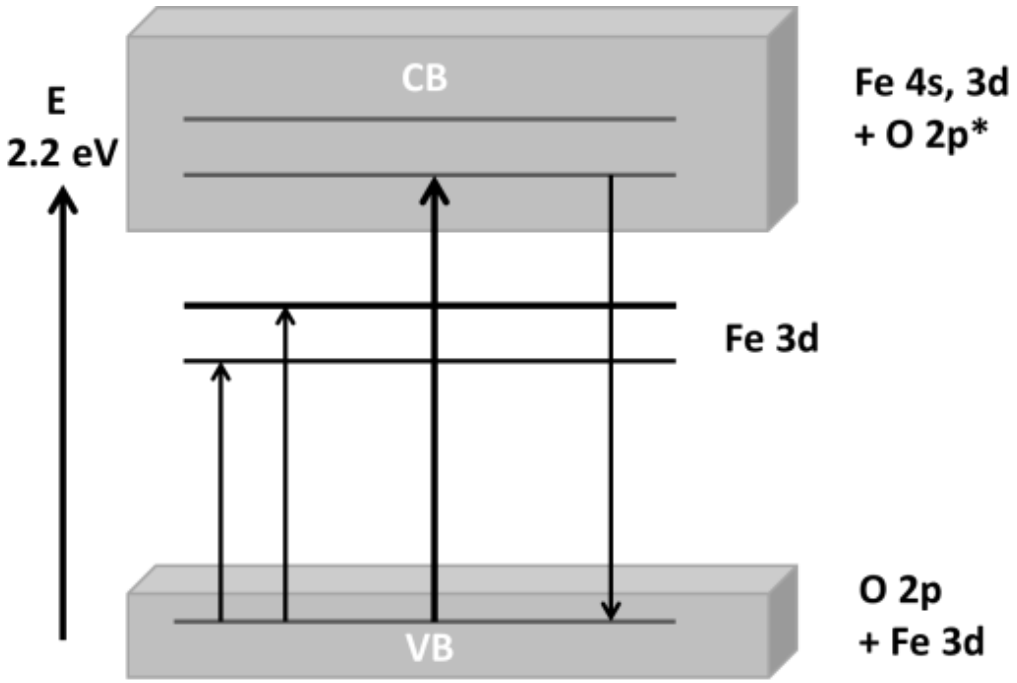

Figure 1. 5 Schematic illustration of the electronic band structure of iron oxides [19].

Inorganic metal and semiconductor nanoparticles are zero dimensional nanomaterials. With semiconductor quantum dots (Qd) being the most extensively developed and studied [21]. Their unique size (1-10 nm) and shape dependent optical and electronic properties differing from the bulk and form the atomic level are attributed to the 3-dimensional quantum confinement effect.

The lowest eigenvalue in a quantum confined system according to the approximation is given by

$$\mathbf{E_{g,Qd} = E_{g,b} + \left(\frac{\hbar^2}{8R^2}\right)\left(\frac{1}{me} + \frac{1}{mh}\right) - \left(\frac{1.8e^2}{4\pi\varepsilon_0\varepsilon R}\right)}, \qquad (1.1)$$

where the first two energy terms are the band energies of the quantum dot and bulk solid, respectively. R is the quantum dot radius, m_e is the effective mass of the electron in the solid, e is the elementary charge of the electron, $\hbar$ is planks constant, m_h is the effective mass of the hole in the solid, and ε is the dielectric constant of the solid. The middle and the last terms represent the exciton of a 'particle-in-a-box-like' and coulomb attraction of the electron-hole pair, respectively. From the equation it can be seen that as the dimension (R) decreases, the band gap increases, which is shown in Fig 1.6. [22]. Semiconductor nanomaterials can be doped of metals or rare earth ions to engineer or manipulate certain properties for a particular application.

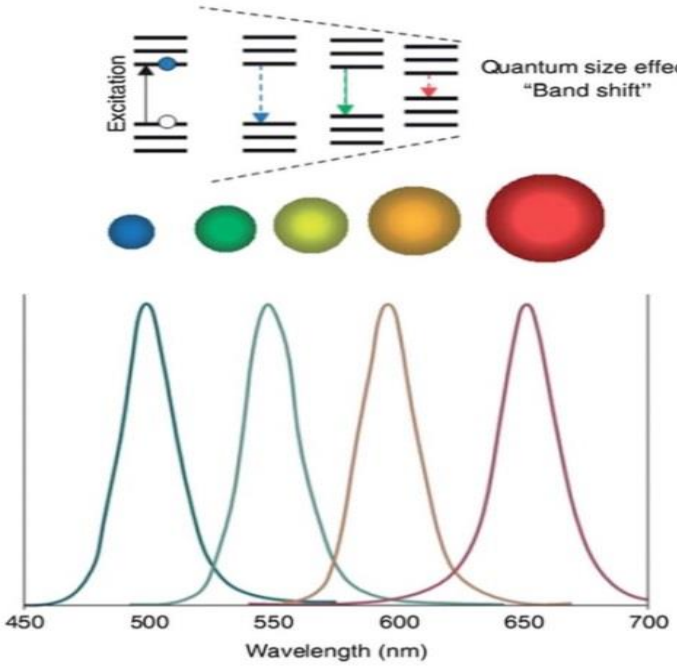

***Figure 1. 6** Size-dependent PL colors of semiconductor QDs [21].*

1.3 Properties of lanthanide doped nanoparticles

The incomplete 4f shell which produces a very large number of low-lying levels enables the rare earths to have the most complicated spectra of any of the element. Their transition gives many-line spectrum without any apparent regularity. Even the prominent feature, which is the multiples, of the spectra of the transition elements is in general unrecognizable. This has caused a neglect of the rare earth spectra. However, recently there has been a renewed attention by researchers towards the rare earths because of their growing importance [23]. The fascinating optical properties of the trivalent lanthanides ions, Ln^{3+}, originate from the special features of the electronic $[Xe]4f^n$ configurations (n = 0 – 14). A rich number of electronic states are generated by these configuration, of which the number is given by [14!/n!(14 – n)!], translating to 3003 for Eu^{3+} and Tb^{3+}, for example. Due to the shielding of the 4f orbitals by the filled $5s^25p^6$ subshell, the energies of these levels are well defined, and they are little sensitive to the chemical environments in which the lanthanides ions are inserted [24].

The energy levels of the $4f^n$ configurations of lanthanides ions were extensively measured in various host lattices, these measurements were carried out by Dieke and co-workers in the 1950s

and 1960s. The energy levels diagrams (Fig 1.7) are referred to as 'Dieke diagram'. The energies of the J multiplets vary by only a small amount in different host crystals which makes the diagram very useful [25].

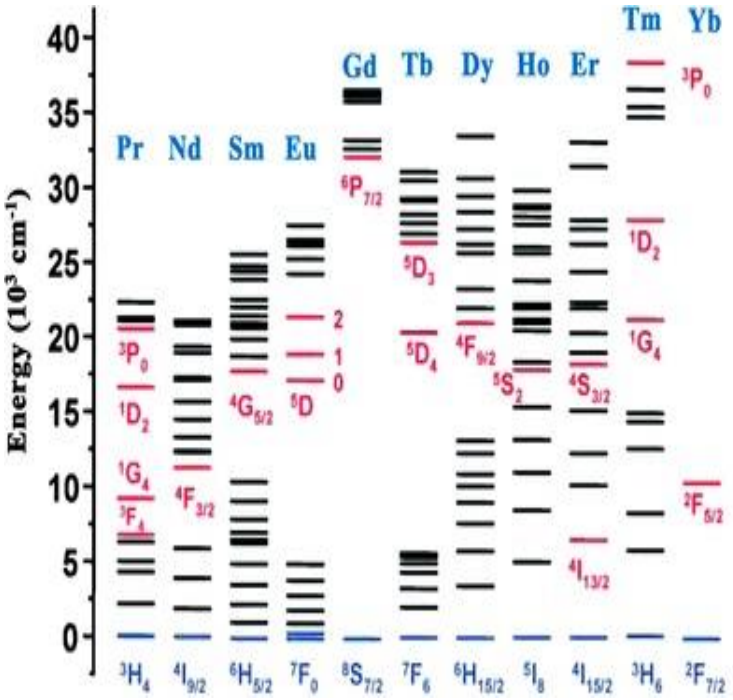

Figure 1. 7 Partial $4f^n$ energy diagrams for Ln^{3+} ions. The main luminescent levels are drawn in red, while the ground states are indicated in blue [26].

The trivalent lanthanide (Ln^{3+}) activated luminescent materials are widely used for solid state lasers, luminescence lamps, photonic devices, bio-imaging etc. Ln^{3+} ions in solids are enabled by their unique electronic structure to emit photon efficiency in the spectral region from UV to Vis to IR [27].

Ln^{3+} is involved in three types of transitions, Ligand to metal charge transfer (LMCT), 4f – 5d, and intra-configurational 4f – 4f. The former two usually occurs at higher energies which makes them irrelevant for bio-applications, so only the latter is discussed. The detrimental effect on the emissive properties of easily reducible Ln^{3+} ions (e. g Eu^{3+}, Sm^{3+}, or Tb^{3+}) may be caused by the low-lying LMCT state. Some ions are found to be fluorescent ($\Delta S = 0$), some are phosphorescent ($\Delta S > 0$), and some are both. Ln^{3+} on their own do not give off light, however when inserted into a chemical environment, non-centrosymmetric interaction allows the mixing of electronic state of

opposite parity into the 4f wave functions and electric dipole (ED) transition become partly allowed, which are termed induced ED transition. The intensity of some of the transitions is particularly sensitive to the nature of the metal-ion environment, and these transitions are called hypersensitive [24].

1.4 Luminescence

Luminescence is a phenomenon in which the electronic state of a substance is excited by some kind of external energy and excitation energy is given off as light. It is divided into phosphorescence and fluorescence. Where, in phosphorescence a light emission from a substance continues for few seconds, minutes or hours after the excitation radiation has ceased, while in fluorescence, emission stops suddenly after radiation has stopped [28]. Luminescence includes a wide variety of light emitting processes which derive their names from the varied sources of energy that power them. Electroluminescence is produced by the passage of an electric current through an ionized gas. Chemiluminescence derives its energy from chemical reaction. Chathodoluminescence light is generated from exposure of substances to cathode rays. Photoluminescence derives its energy from the absorption of photon energy [29].

The inorganic materials luminescence is composed of the following processes: (1) absorption and excitation, (2) energy transfer, and (3) emission. Most luminescent materials consist of a host material to which certain dopant ions, also termed activators, are added. The host lattice plays two distinctive roles in this case: as a passive matrix to define the spatial locations of the activator ions; and as an active participant in the luminescence process, exerting its own specific influence on the spectroscopic behavior of the activator. In the latter, it helps to shape the structure of the energy levels of the activator and also introduce vibrations of various energies, the so called phonons, which influence the kinetics of the luminescence phenomena [30]. Luminescence can be classified as intrinsic and extrinsic type. Intrinsic luminescence is related to intrinsic properties of the crystals that have different types of structural defects. An extrinsic luminescence is activated by impurities such as transition metals or rare earth elemental ions [29].

1.4.1 Intrinsic luminescence

Three kinds of intrinsic photoluminescence: band-to-band, exciton and cross-luminescence. The recombination of an electron in the conduction band with a hole in the valence band results in band-to-band transition and can only be observed in a very pure crystal at relatively high temperature. The Fermi level which is an important concept in solid state material is defined as the energy level at which the probability of occupation by an electron is ½. For an intrinsic semiconductor, the Fermi level lies at the mid-point of the band gap. The distribution of electron within the solid is therefore changed by doping, and hence changes the Fermi level. For an n-type semiconductor, the Fermi level lies just below the conduction band, whereas for a p-type semiconductor it lies just above the valence band [31]. Luminescence occurs when a material absorbs radiation that brings about the transition of electrons from the valence band to the conduction band, which is then followed by radiative recombination of electrons [32]. The latter de-excitation of the electrons back to the valence band occurs via a luminescence center, which converts their energy to electromagnetic wave. These luminescence centers can either be intrinsic defects or extrinsic defects [33]. When an atom in a matrix is displaced from its original position to an interstitial position, it creates an intrinsic defect, where it generates a point defect leaving behind a vacancy effect [34]. When the electrons are excited from the valence band to the conduction band, the radiation is absorbed by a material within an intrinsic defect, leaving behind positively charged holes in the valence band.

1.4.2 Extrinsic luminescence

Extrinsic defects are intentionally incorporated dopants into a host matrix, in order to generate a luminescence center. When the excited electrons de-excite to the luminescence center, it de-excite to the lower state of the center radiatively, giving electromagnetic wave with different wavelength depending on the ion adopted for luminescence center , D represents donor level and A acceptor level, as shown in Fig 1.8 [35]. Usually oxides based phosphors are employed to get efficient up and down conversion luminescence properties. Up-conversion is a process by which two or more low energy photons are converted into high-energy photon. Down conversion is a process by which one high-energy photon is converted into two or more lower energy photons [36].

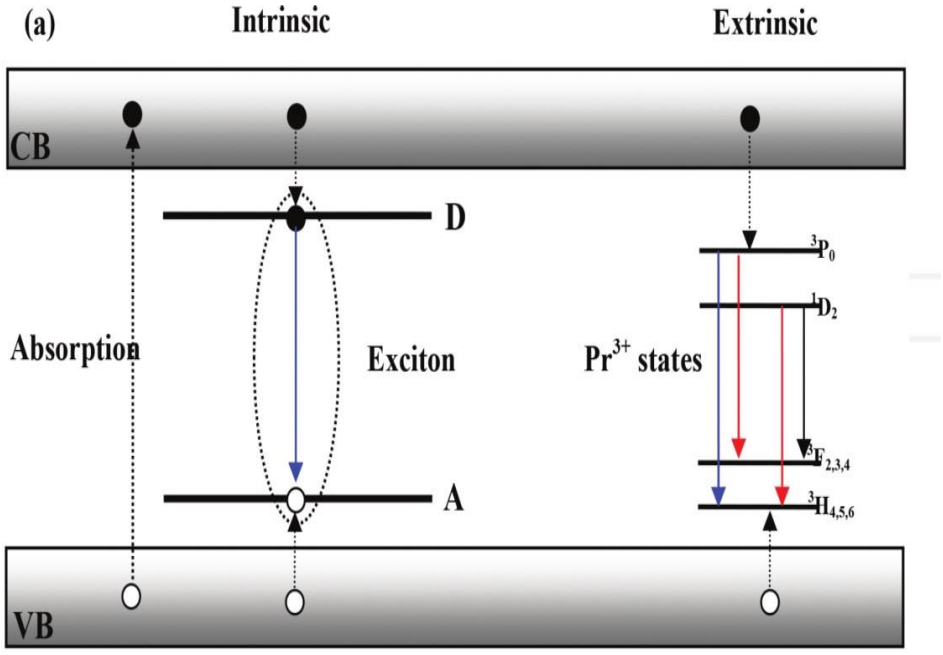

Figure 1. 8 A schematic diagram showing an emission from both intrinsic and extrinsic defects [35].

1.5 Up-conversion nanoparticles

Up-conversion refers to a nonlinear optical process that converts two or more low-energy pump photons to a higher-energy output photon [37]. The infrared radiation is absorbed by the materials and up-converted to emit in the visible spectrum through a series of real as opposed to virtual levels as in conventional two-photon dyes. The mechanism of up-conversion can be described as either sequential excitation of the same atom or excitation of two centers and subsequent energy transfer [38]. The emission of Up-conversion nanoparticles (UCNPs) consists of sharp lines characteristic of atomic transitions in a well-ordered matrix. Using different rare earth dopants, including Er^{3+}, a large number of distinctive emission spectra can be obtained that can be tailored to the photosensitizer excitation spectra. The sequential 2 photon nature of the excitation process is the main advantage, which gives rise to the very low power levels associated with up-conversion [39].

UCNPs hold a great promise for a broad range of application ranging from high-resolution bio-imaging to modern photovoltaic technology, because of their remarkable ability to combine two or more low energy photons to generate a single high energy photon by an anti-Stokes process.

When excited by near infrared (NIR) wavelength, there is substantial reduction of light scattering by biological tissues. This reduction enables a depth penetration in tissue much larger than that obtained under UV or Vis excitation. The advantages of exciting with NIR is that it eliminates background interference from either endogenous fluorophores or non-specifically bound probes, thus enabling quantitative analysis of molecular interaction in biological samples [40].

The 4f – 4f orbital electronic transition with concomitant wave function localized within a single lanthanide ion give rise to upconversion photoluminescence. The outer complete 5s and 5p shells that shield the 4f electrons, results in line-like sharp emission, which exhibit high resistance to photobleaching, and photochemical degradation. The intra – 4f electronic transition of lanthanide are electric dipole forbidden by quantum mechanical selection rule, which, however, are relaxed due to local crystal field – induced intermixing of the f states with higher electronic configuration. The very long lifetime for energy levels of lanthanide ions are yielded by the primary forbidden nature of the 4f – 4f transitions thus favoring the occurrence of sequential excitations in the excited state of a single lanthanide ions as well as permitting favorable ion – ion interactions in the excited state to allow energy transfers between two or more lanthanide ions. These resulting features of lanthanides dopants determine the basic UC mechanisms [41].

1.5.1 Down mechanisms

Down-conversion is a stoke emission process resulting from an excited lanthanide ion embedded in a host lattice. Whereas, an anti-stoke emission process which the sequential absorption of two or more photons leads to the emission of light at a shorter wavelength (higher energy) than excited wavelength is called up-conversion [42]. Down conversion and different up-conversion luminescence mechanisms have been recognized either alone or in combination. Two basic mechanisms are widely used, excited state absorption (ESA) and Energy transfer up-conversion (ETU).

(i) Down-conversion

In a down-conversion mechanism, an incident irradiation is absorbed by an active material and converted to lower energy (longer wavelength) photon as shown in Fig 1.9.

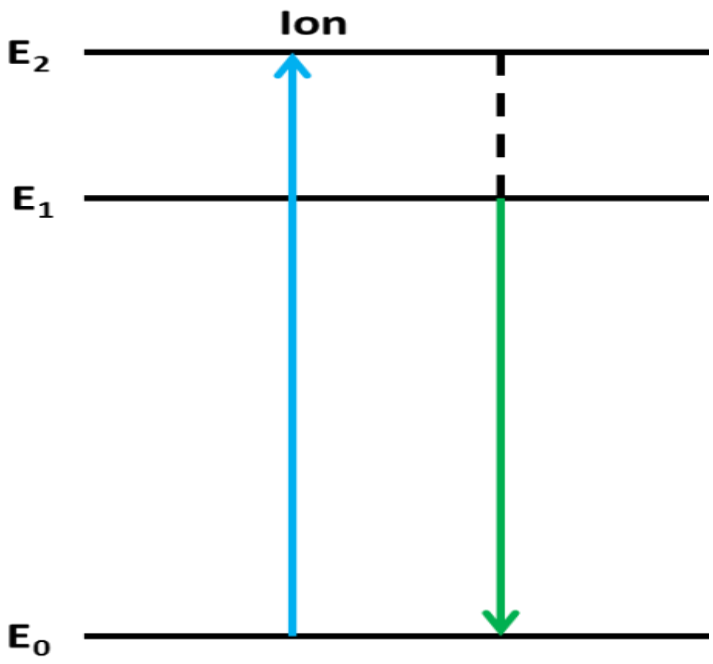

Figure 1. 9 Down-conversion for lanthanide-doped nanoparticles [42].

1.5.2 Up-conversion mechanisms

(ii) ESA

ESA up-conversion (Fig 1.10.) occurs upon excitation by sequentially absorbing one or more photons from the ground state to intermediate reservoir stage, and finally populate the excited state. An ion is first excited to the E_1 state from ground state upon absorption of photon, a second pump photon promote the ion from E_1 to higher energy photon E_2, before it decays to the ground state E_0 [43].

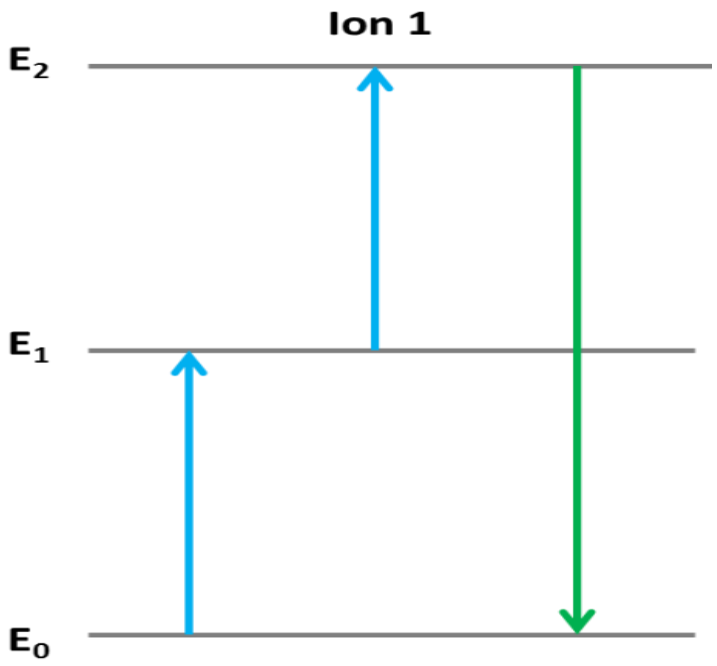

Figure 1. 10 Excited state absorption up-conversion process for lanthanide-doped up-conversion nanoparticles [42].

(iii) ETU

In ETU process two ions are involved. One ion absorbs the energy and transfer to the other ion. The already excited ion is excited to higher energy state by the transferred energy, which results in the emission of higher energy photon, as shown in Fig 1.11 [44].

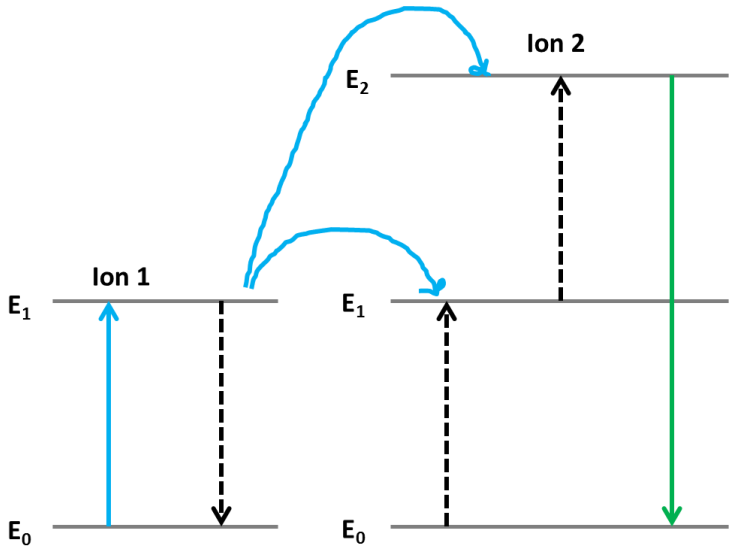

Figure 1. 11 Energy transfer up-conversion processes for lanthanide-doped up-conversion nanoparticles [43].

Lanthanides ions with a ladder-like energy level structure are suitable for the single doping system including Er^{3+} and Ho^{3+}, which are currently the most effective activators.

Lanthanide ions such as Er^{3+} ions doped into a well suitable host materials are well known for up-conversion emission, absorbing in the NIR range (980 nm) and emitting green (550 nm) and red (670 nm) visible light. When Er^{3+} ions are co-doped with Yb^{3+} ions, they show a high quantum yield for NIR absorption and is applied for sensitizing and enhancing the emission intensity Fig 1.12 (b). Since the lanthanide doped nanophosphors are known for their emission of the NIR light under NIR excitation, the excited Yb^{3+}ions which has a higher absorption efficiency than Er^{3+} ions can therefore transfer its energy to the Er^{3+} ions which results in the excitation of $^4I_{11/2}$ level. The non-radiative decay to the $^4I_{13/2}$ level follows the energy transfer and further radiative decay to the ground level under emission of 1.5 μm light Fig 1.12 (c). This emission in the NIR light under 980 nm excitation recently has shown growing interest for biomedical application due to the so called biological window, which is a wavelength ranging from 650 to 1350 nm where light has its maximum depth of penetration in tissues [45].

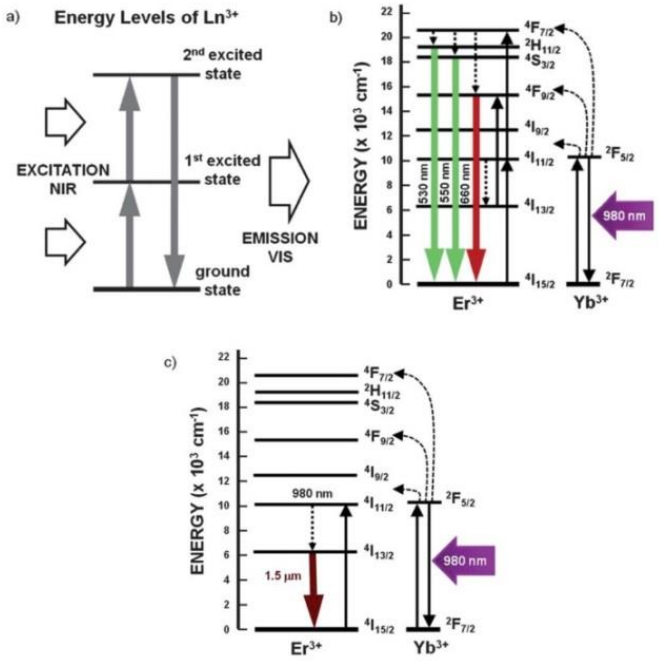

Figure 1. 12 (a) Principle of up-conversion emission. (b) Up-conversion emission of visible light and (c) NIR emission under NIR excitation of an Er^{3+} and Yb^{3+} doped host matrix [45].

1.5.2.1 Holmium ion (Ho^{3+})

Holmium is a rare-earth metal, the 4f shell lack four electrons of being filled. The $6s^2$ and $5d^1$ electrons are believed to enter the conduction band leaving a tri-positive ion core. The 4f shell however is deeply embedded in the ion's interior and is screened from the crystalline environment by the filled $5s^2$ and $3p^6$ shell so that the configuration of the ion core is approximately described by the spectroscopic state $^5I_8$. The magnetic moments result because of the unpaired electrons in the 4f shell. In the paramagnetic region, the holmium magnetic susceptibility gives of the values for the total effective magnetic moments of $10.6\mu_B$ to $10.9\mu_B$, while measurement of the saturation magnetization gives values between $10.0\mu_B$ and $10.34\mu_B$.

Holmium has a hexagonal close-packed structure and the magnetic moment is found in three magnetic phases. The structure is paramagnetic with magnetic moment oriented at random above the Néel temperature of 131.4°K. It is antiferromagnetic with the average moment aligned in the basal plane to the next between the Néel temperature and the Curie point of 19.4°K, but as one proceeds from one basal to the next, the direction of the average moment rotates. Below the Curie point the structure is ferromagnetic with a conical spiral with a moment of $1.7\mu_B$ in the basal planes [46]. Ho^{3+} has one of the highest magnetic moments of all elements (10.6 μ_b) and also exhibit characteristic luminescence [47]. Ho^{3+} is a good candidate for up-conversion processes because it has many long-lived intermediate metastable levels, from which ESA can take place as shown in Fig 1.13. There are several high-lying metastable levels that can give rise to transitions at various wavelengths in the visible and UV regions. However, most up-conversion studies on Ho^{3+} - doped materials focused on infrared and visible regions [48]. Ho^{3+} has two main up-conversion bands of green and red emission at 541 and 647 nm, corresponding to the transition $^5S_2/^5F_4$–$^5I_8$ and $^5F_5$–$^5I_8$, respectively [49].

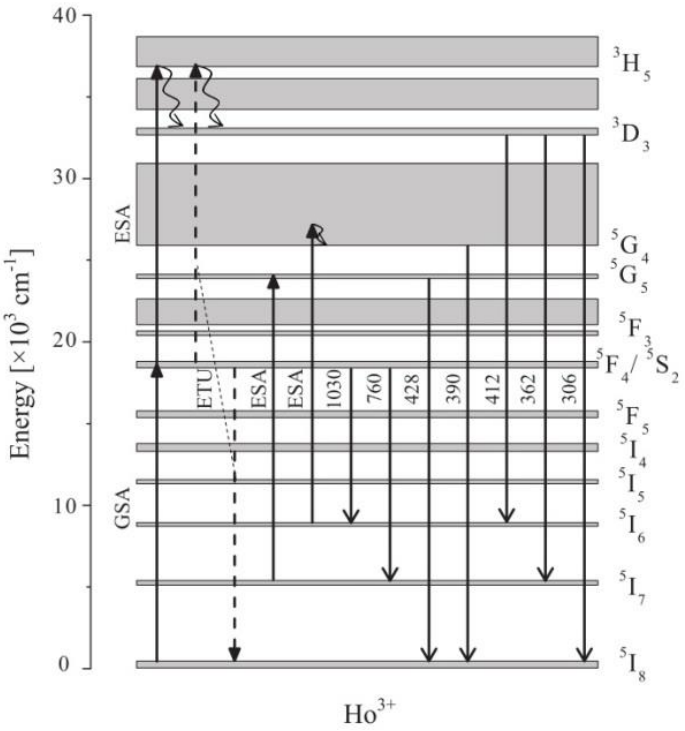

Figure 1. 13 Partial energy-level diagrams of Ho3+ ions and proposed up-conversion emission mechanism [50].

1.5.1.2. Thulium (Tm^{3+})

Tm^{3+} is the first Lanthanide ion from which up-conversion has been observed [50]. Thulium(III) complexes are mainly known for their combined weak visible/red/NIR emission from the $^1G_4$ state, which lies at 21,200 cm^{-1} and thus requires near-UV absorbing antenna chromophores. The emission bands from this state are situated at 480, 650 and 770 nm. Recently, emission has been detected from the $^3F_4$ state with emission bands at 790 and 1,465 nm. These $^3F_4$ emissions can be sensitized through visibly absorbing tropolonate ligands that have triplet energies that are too low for sensitization of the $^1G_4$ emissions. This NIR thulium(III) can also be sensitized by azulene-type chromophores, which have a moderate absorption in the red part of the visible light [51].

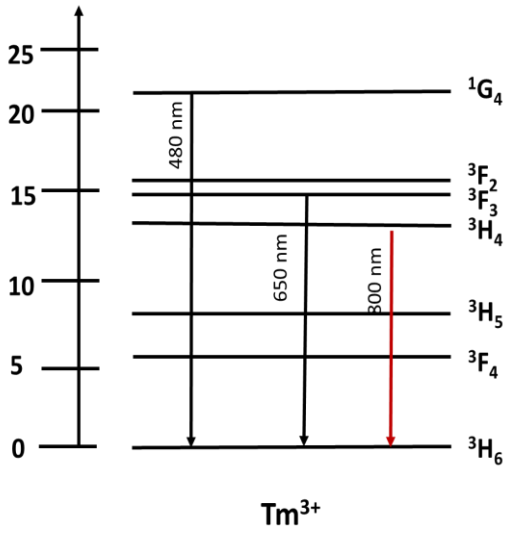

Figure 1. 14 Partial energy-level diagrams of Tm^{3+} ions and proposed up-conversion emission mechanism [51].

1.5.1.3. Ytterbium (Yb^{3+})

To increase the absorption of light, ytterbium ions are widely used as sensitizer. They possess a high absorption cross section and its $^2F_{5/2}$ energy level overlaps ion energy with $^4I_{1/2}$ energy level of erbium. This energy overlap derives to a very good resonant energy transfer between these two ions and the consequently greater efficiency of erbium luminescence generation. This makes ytterbium an ideal sensitizer ion for erbium [50], thereby making it possible to measure the UPC luminescence. Yb^{3+} has the advantage to present only two multiplets: the ground-state level $^2F_{7/2}$ and the excited-state level $^2F_{5/2}$, corresponding to the highly efficiency absorption in the range of 900 nm- 1000 nm. this particular energy level structure is highly desirable for efficient absorption of commercially available laser diode emitting around 980 nm and avoiding any undesirable excited-state absorption under intense optical pumping [52].

Tm^{3+} -doped materials generates blue up-conversion emission from the electronic transitions $^1D_2 \rightarrow {}^3F_4$ and $^1G_4 \rightarrow {}^3H_6$ around 450 and 480 nm, respectively. The energy transfer between Yb^{3+} and Tm^{3+} ions are well known. Yb^{3+} and Tm^{3+} are co-doped to significantly increase up-conversion yield owing to an efficient energy transfer from ytterbium to thulium. The advantage of Yb^{3+} ions are that they absorb in the near-infrared region around 940- 980 nm, where laser diodes work efficiently. Yb^{3+} ions are good sensitizer for Tm^{3+} ions, for which laser operation has already been

achieved in the blue region by up-conversion around 480 nm, and in the infrared region around 1.5μm, 1.9μm and 2.3μm [53].

By pumping 940 nm only Yb^{3+} ions are excited, the electronic population was excited from the ground state $^2F_{7/2}$ to the $^2F_{5/2}$ energy level. There is also a simultaneous interaction of two Yb^{3+} ions in the excited state $^2F_{5/2}$, which transferred its energy to the $^1G4$ energy level of Tm^{3+} ions ($^2F_{5/2} + {}^2F_{5/2} + {}^3H_6 \rightarrow {}^2F_{7/2} + {}^2F_{7/2} + {}^1G_4$). The decay from the $^1G_4$ to the $^3H_6$ and $^3F_4$ levels generated the emissions at 476 and 650 nm, respectively. The emissions at 802 nm and 1.48 μm were generated due to the decay from the $^3H_4$ to the $^3H_6$ and $^3F_4$ levels, respectively [53]. This process is shown in Fig 1.15.

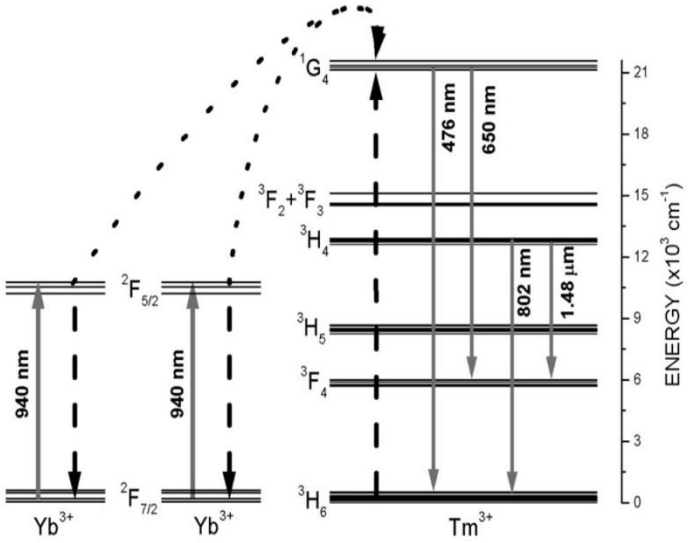

Figure 1. 15 Diagram of the implied energy levels of thulium and ytterbium ions in the energy transfer [53].

1.6 Applications of α-Fe_2O_3 nanoparticles

α-Fe_2O_3 nanoparticle has many applications in magnetic sealing, oscillation damping, position sensing, ultra-high density magnetic storage media, clinical diagnosis and treatment, imaging, photovoltaic, detection and separation [54]. The photovoltaic efficient properties have been demonstrated by the design of thin films of hematite consisting of crystalline arrays of oriented nanorods. They exhibit substantial photocurrent efficiency due to a better transport and collection of photogenerated electrons through a designed path as well as better physical and structural match between the n-type semiconductor material, the diameter of its nano building blocks and the

minority carrier diffusion length [55]. Fig 1.16 shows the coupled photoelectrocatalytic oxidation of H_2O to O_2 at a semiconductor anode and O_2 reduction to water at a biocathode comprising an O_2 reducing enzyme immobilized on an inexpensive carbon- cloth cathode [56].

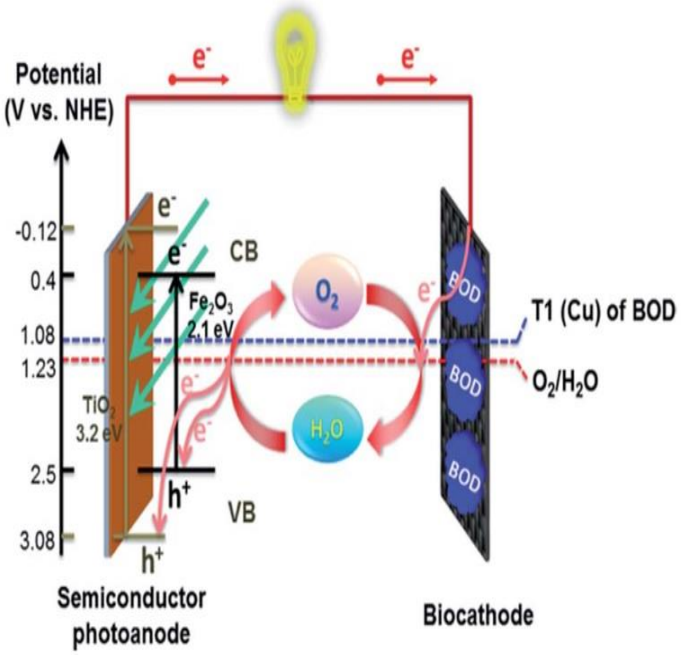

Figure 1. 16 Schematic representation of the operation principle of a bio- photovoltaic cell consisting of a semiconductor photo-anode and an O^{2-}reducing bilirubin oxidase/carbon cloth bio-cathode [56].

In our work, we focus on the optical/fluorescence bio-imaging application. Fluorescence imaging among various modalities for bio-imaging is of special interest because of its low cost, high sensitivity and high spatial resolution. Auto-fluorescence, high light scattering and absorption of the different tissues and blood components are the fundamental barriers to fluorescence imaging of a tissue in the case of a real-time *in vivo* detection. These endogenous absorbers passed a high absorption characteristic between 200 nm and 650 nm and thus prevent light penetrating deep into the tissues in the visible range, this phenomenon is shown in Fig 1.17. The auto-fluorescence of the tissues also limits the signal-to-noise ratio and hampers detection of the fluorescence imaging agents. These intrinsic limitations have stimulated the development of fluorescence probes with absorption and emission maxima in the 650 – 1450 nm range, where tissues have minimal absorption and fluorescence[19].

The benefits of using UCL for biological applications are their sharp emission lines, long lifetime, and photo stability. The advantage for using UCL in microscopy is that they reduce photo-bleaching and high scattering problem in tissue without requiring highly complicated and high cost-second laser and photo-multiplier tubes [44]. Since rare earth UC nanoparticles are able to produce narrow bands emissions with higher energy after the excitation by continuous-wave near infrared lasers, they are endowed with large anti-stokes shifts and less possibility for spectral overlapping [57]. The unique physiochemical properties of rare earth doped α-Fe_2O_3 allow them the potential roles in biological applications. The special properties that can play a role in biological application are the particle size, size distribution, shape, and surface area, with the particle size being the most important characteristic. The particle not only affects the physical properties but also affect biological outcome after nanoparticles (NPs) were injected into the human body. For NPs to be rapidly cleared due to ex-osmosis, the particle size should be less than 10 nm. For particles more than 200 nm, the NPs are not easily mechanically filtered by the spleen in the reticuloendothelial system, leading to decrease in blood circulation time. Ideal particle size for the biological application is in the particle range of 10 – 100 nm, where they have the longest blood circulation time. The particles volume is small enough to escape the phagocytosis of the reticuloendothelial system and penetrate into capillary vessels in body tissues, which ensure an effective distribution in specific tissues [58].

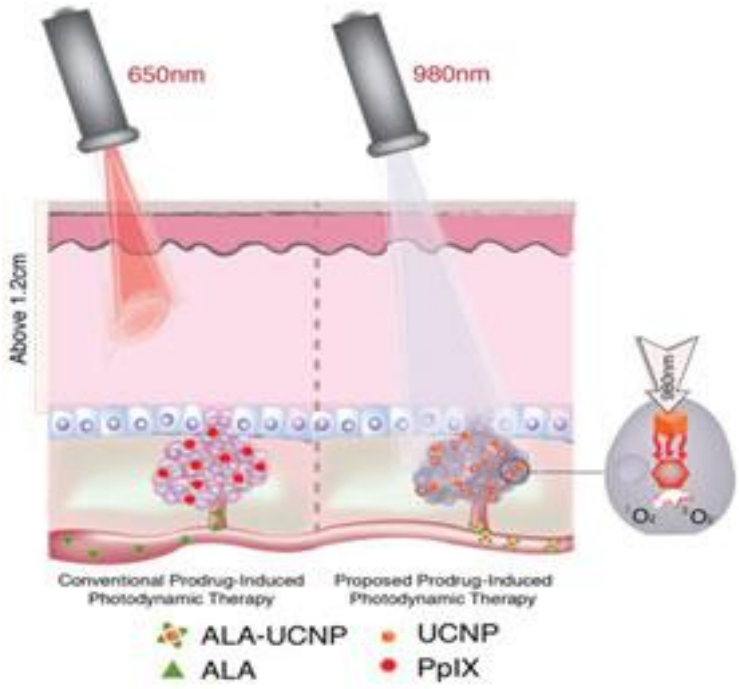

Figure 1. 17 Up-conversion nanoparticles that can convert near infrared light into red light can be used to extend photodynamic therapy for some cancer found in deep tissues [59].

Fig 1.18 shows the combined new type of nanoparticles with a food and drug administration (FDA) approved photodynamic therapy to effectively kill deep-set cancer cells *in vivo* with minimal damage to surrounding tissues and fewer side effects than chemotherapy. In this therapy, the patient is given a non-toxic light sensitive, in our case it would be rare earth doped α-Fe_2O_3 nanoparticles, which is absorbed by all body cells, including cancerous ones. Red laser light specifically tuned to the drug molecules are sensitively turned on to tumor area. When the light interact with the photosensitive drug, it produces a highly reactive form of oxygen that kills the malignant cancer cells while leaving most neighboring cells unharmed [59].

The aim of this work is to develop a novel, non-invasive, low-cost infrared imaging technique that would improve upon current methods, because this technique may function as a diagnostic tool due to the specific bio-conjugation of these nanoparticles to human outer surface makers. This require a comprehensive investigation to archive the new nanomaterial with imaging ability. This work focuses on the doping (Ho and Tm) and co-doping (Ho:Yb and Tm:Yb) of α-Fe_2O_3 . The chosen rare earth has been widely investigated due to their ability to convert low energy photons to high-energy photons via the up-conversion process.

The objectives of the current work are:

- To synthesize and characterize Fe_2O_3 nanoparticles using sol-gel and microwave methods
- Dope Fe_2O_3 with rare earth ions and characterize the doped nanoparticles
- To investigate the optical and magnetic properties of both un-doped and doped Fe_2O_3
- Investigate the energy transfer between the host and the dopant

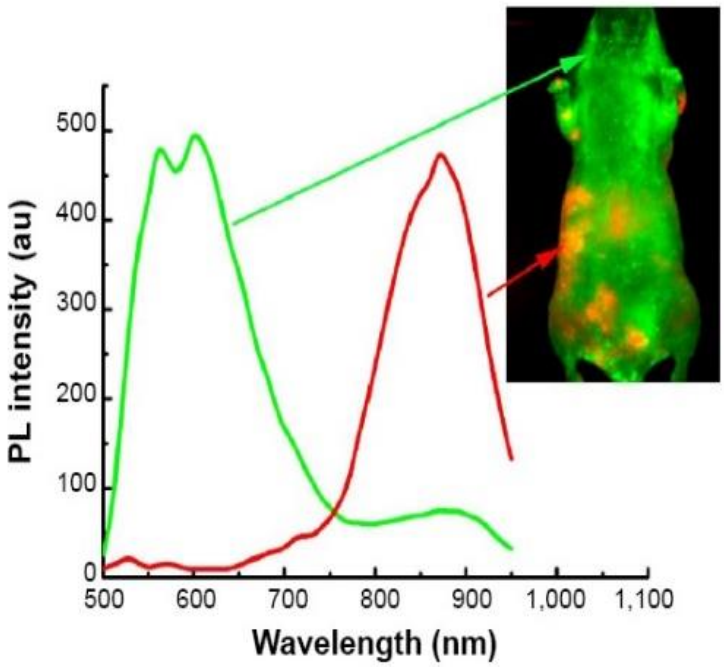

Figure 1. 18 In vivo imaging of pancreatic tumor-bearing mouse injected with multiple system antrophy (MSA)-functionalized NIR Quantum dots (QDs) [60].

References

[1] M. L. Trudeau and J. Y. Ying, "Nanocrystalline materials in catalysis and electrocatalysis: Structure tailoring and surface reactivity," *Nanostructured Mater.*, vol. 7, no. 1–2, pp. 245–258, 1996.

[2] M. J. A. Fernández-garcia and Rodriguez, "Metal Oxide Nanoparticles," *Nanomater. Inorg. Bioinorg. Perspect.*, no. October, p. 60, 2007.

[3] H. Gleiter, "Nanostructured Materials : State of Teie Art and Perspectives," *Pergamon Nan&tructurcd Mater.*, vol. 6, no. 6, pp. 3–14, 1995.

[4] P. Ayyub, V. R. Palkar, S. Chattopadhyay, and M. Multani, "Effect of crystal size reduction on lattice symmetry and cooperative properties," *Phys. Rev. B*, vol. 51, no. 9, pp. 6135–6138, 1995.

[5] W. Wu, Z. Wu, T. Yu, C. Jiang, and W.-S. Kim, "Recent progress on magnetic iron oxide nanoparticles: synthesis, surface functional strategies and biomedical applications," *Sci. Technol. Adv. Mater.*, vol. 16, no. 2, p. 23501, 2015.

[6] M. Mohapatra and S. Anand, "Synthesis and applications of nano-structured iron oxides / hydroxides – a review," vol. 2, no. 8, pp. 127–146, 2010.

[7] P. Mallick and B. N. Dash, "X-ray Diffraction and UV-Visible Characterizations of α-Fe2O3 Nanoparticles Annealed at Different Temperature," *Nanosci. Nanotechnol.*, vol. 3, no. 5, pp. 130–134, 2013.

[8] G. S. Parkinson, "Iron oxide surfaces," *Surf. Sci. Rep.*, vol. 71, no. 1, pp. 272–365, 2016.

[9] R. M. Cornell and U. Schwertmann, *The Iron Oxides*. 2003.

[10] A. S. Teja and P. Y. Koh, "Synthesis, properties, and applications of magnetic iron oxide nanoparticles," *Prog. Cryst. Growth Charact. Mater.*, vol. 55, no. 1–2, pp. 22–45, 2009.

[11] R. D. Zysler, D. Fiorani, and A. M. Testa, "Investigation of magnetic properties of

interacting Fe2O3 nanoparticles," *J. Magn. Magn. Mater.*, vol. 224, no. 1, pp. 5–11, 2001.

[12] V. N. Nikiforov, Y. A. Koksharov, S. N. Polyakov, A. P. Malakho, A. V. Volkov, M. A. Moskvina, G. B. Khomutov, and V. Y. Irkhin, "Magnetism and Verwey transition in magnetite nanoparticles in thin polymer film," *J. Alloys Compd.*, vol. 569, pp. 58–61, 2013.

[13] Y. Gossuin, S. Disch, Q. L. Vuong, P. Gillis, R. P. Hermann, J. H. Park, and M. J. Sailor, "NMR relaxation and magnetic properties of superparamagnetic nanoworms," *Contrast Media Mol. Imaging*, vol. 5, no. 6, pp. 318–322, 2010.

[14] M. Kerker, P. Scheiner, D. D. Cooke, and J. P. Kratohvil, ''Absorption and Index and Color of Colloidal Hematite,'' *J. Colloid Interface Sci*., vol.71, pp. 176–87, 1979

[15] J. Wang, W. B. White, and J. H. Adair, "Optical properties of hydrothermally synthesized hematite particulate pigments," *J. Am. Ceram. Soc.*, vol. 88, no. 12, pp. 3449–3454, 2005.

[16] J. Torrent and V. Barron, "Diffuse reflectance spectroscopy of iron oxides," *Encycl. Surf. Colloid Sci.*, pp. 1438–1446, 2002.

[17] Y. Yamanoi, S. Nakashima, and M. Katsura, "Temperature dependence of refectance spectra and color values of hematite by in situ, high-temperature visible micro-spectroscopy," *Am. Mineral.*, vol. 94, no. 1, pp. 90–97, 2009.

[18] J. Lee and S. Han, "Thermodynamics of native point defects in α-Fe2O3: an ab initio study.," *Phys. Chem. Chem. Phys.*, vol. 15, no. 43, pp. 18906–14, 2013.

[19] L. Lacroix, F. Delpech, C. Nayral, S. Lachaize, and B. Chaudret, "New generation of magnetic and luminescent nanoparticles for in vivo real-time imaging.," *Interface Focus*, vol. 3, no. 3, p. 20120103, 2013.

[20] E. O. Chukwuocha, M. C. Onyeaju, and T. S. T. Harry, "Theoretical Studies on the Effect of Confinement on Quantum Dots Using the Brus Equation," *World J. Condens. Matter Phys.*, vol. 2, no. May, pp. 96–100, 2012.

[21] S. Suresh, "Semiconductor Nanomaterials, Methods and Applications: A Review," *Nanosci. Nanotechnol.*, vol. 3, no. 3, pp. 62–74, 2013.

[22] J. Mirzaei, M. Reznikov, and T. Hegmann, "Quantum dots as liquid crystal dopants," *J.*

Mater. Chem., vol. 22, no. 42, p. 22350, 2012.

[23] G. H. Dieke, H. M. Crosswhite, and B. Dunn, "Emission Spectra of the Doubly and Triply Ionized Rare Earths," *J. Opt. Soc. Am.*, vol. 51, no. 8, p. 820, 1961.

[24] J. C. G. Bünzli, "Lanthanide luminescence for biomedical analyses and imaging," *Chem. Rev.*, vol. 110, no. 5, pp. 2729–2755, 2010.

[25] P. S. Peijzel, A. Meijerink, R. T. Wegh, M. F. Reid, and G. W. Burdick, "A complete 4fn energy level diagram for all trivalent lanthanide ions," *J. Solid State Chem.*, vol. 178, no. 2 SPEC. ISS., pp. 448–453, 2005.

[26] Yongsheng Liu, Datao Tu, Haomiao Zhua and Xueyuan Chen, "*Lanthanide-doped luminescent nanoprobes: controlled synthesis, optical spectroscopy, and bioapplications*", Chem. Soc. Rev., vol. 42, pp. 6924, 2013

[27] H. Dong, L. D. Sun, and C. H. Yan, "Energy transfer in lanthanide upconversion studies for extended optical applications," *Chem Soc Rev*, vol. 44, no. 6, pp. 1608–1634, 2015.

[28] M. S. Dhlamini, "Luminescent Properties of Synthesized PbS Nanoparticle Phosphors," 2008.

[29] I. Remarks, A. Of, and L. Techniques, "Luminescence : An Introduction," *Luminescence*, pp. 1–6, 1852.

[30] C. R. Cornejo, "Luminescence Rare Earth Earth Ion-Doped Ion - Doped Oxide Oxide Compounds," Luminescence - An outlook on the phenomena and their applocations, pp. 33-63, 2016.

[31] M. Chirita and I. Grozescu, "Fe_2O_3 – Nanoparticles , Physical Properties and Their Photochemical And Photoelectrochemical Applications," *Chem Bull Politeh. Univ Timsisoara*, vol. 54, no. 68, pp. 1–8, 2009.

[32] I. Light, "CHAPTER 1 PHOSPHORS – AN OVERVIEW," pp. 1–31.

[33] L. L. Noto and A. Sciences, "Persistent luminescence mechanism of tantalite phosphors," 2014.

[34] J. W. Morris, " Defects in Crystals," in *Materials Science*, pp. 76–107.

[35] Hendrik. C. Swart. Luyanda L. Noto, Pontsho. S. Mbule, Bakang M. Mothudi, and and Mokhotjwa. S. Dhlamini "The Dynamics of Luminescence ," Luminescence -An outlook on the phenomena and their application,chapter 2, pp13-32, 2016.

[36] S. Cells, "Up and Down - conversion for Solar Cells Publications," vol. 8111, no. 23, pp. 2012–2013, 2017.

[37] Y. Liu, D. Tu, H. Zhu, and X. Chen, "Lanthanide-doped luminescent nanoprobes: controlled synthesis, optical spectroscopy, and bioapplications," *Chem. Soc. Rev.*, vol. 42, no. 16, p. 6924, 2013.

[38] S. Heer, K. Kömpe, H. U. Güdel, and M. Haase, "Highly efficient multicolour upconversion emission in transparent colloids of lanthanide-doped NaYF4 nanocrystals," *Adv. Mater.*, vol. 16, no. 23–24, pp. 2102–2105, 2004.

[39] B. Ungun, R. K. Prud'homme, S. J. Budijon, J. Shan, S. F. Lim, Y. Ju, and R. Austin, "Nanofabricated upconversion nanoparticles for photodynamic therapy.," *Opt. Express*, vol. 17, no. 1, pp. 80–86, 2009.

[40] and X. L. Sanyang Han, Renren Deng, Xiaoji Xie, "Enhancing Luminescence in Lanthanide-Doped Upconversion Nanoparticles," *Angew. Chem. Int. Ed*, pp. 2–16, 2014.

[41] G. Chen, H. Qiu, P. N. Prasad, and X. Chen, "Upconversion nanoparticles: Design, nanochemistry, and applications in Theranostics," *Chem. Rev.*, vol. 114, no. 10, pp. 5161–5214, 2014.

[42] W. Yang, X. Li, D. Chi, and H. Zhang, "Lanthanide-doped upconversion materials : emerging applications for photovoltaics and photocatalysis," *Nanotechnol. 25*, vol. 482001, no. 25, p. 482001, 2014.

[43] J. Chen and J. X. Zhao, "Upconversion nanomaterials: Synthesis, mechanism, and applications in sensing," *Sensors*, vol. 12, no. 3, pp. 2414–2435, 2012.

[44] D. H. Kim and J. U. Kang, "Review : Upconversion microscopy for biological applications," *Microsc. Sci. Technol. Appl. Educ.*, pp. 571–582, 2010.

[45] E. Hemmer, N. Venkatachalam, H. Hyodo, A. Hattori, Y. Ebina, H. Kishimoto, and K. Soga, "Upconverting and NIR emitting rare earth based nanostructures for NIR-bioimaging.," *Nanoscale*, vol. 5, no. 207890, pp. 11339–61, 2013.

[46] D. T. Keating, "Theory and Measurement of the X-Ray Satellite Reflections in Holmium Due to the Aspherical <math display='inline'> <mn>4</mn> <mi>f</mi> </math> Charge Density," *Physical Review*, vol. 178, no. 2. pp. 732–742, 1969.

[47] M. Bloemen, S. Vandendriessche, V. Goovaerts, W. Brullot, M. Vanbel, S. Carron, N. Geukens, T. Parac-Vogt, and T. Verbiest, "Synthesis and characterization of holmium-doped iron oxide nanoparticles," *Materials (Basel).*, vol. 7, no. 2, pp. 1155–1164, 2014.

[48] F. Qin, Y. Zheng, Y. Yu, Z. Cheng, P. S. Tayebi, W. Cao, and Z. Zhang, "Ultraviolet and violet upconversion luminescence in Ho3+-doped Y2O3 ceramic induced by 532-nm CW laser," *J. Alloys Compd.*, vol. 509, no. 4, pp. 1115–1118, 2011.

[49] X. Li, F. Zhang, and D. Zhao, "Lab on upconversion nanoparticles: optical properties and applications engineering via designed nanostructure," *Chem. Soc. Rev.*, vol. 44, no. 6, pp. 1291–1716, 2015.

[50] J-C. G. Bunzli and and Claude piguet, "Taking advantage of luminescent lanthanide ions," *Chem. Soc. Rev.*, vol. 34, pp. 1048–1077, 2005.

[51] H. Wang and T. Nann, *Springer Series on Fluorescence*, vol. 7, no. July 2010. 2011.

[52] Jun Chang, Gang-Ding Peng, Qing-Pu Wang, "Ytterbium-Codoping in Thulium Doped Silica Fiber", *Progress In Electromagnetics Research Symposium*. Vol.1, no.4,pp.62-66, 2005,

[53] F. Gu ¨ ell a, R. Sole , Jna. Gavalda, M. Aguilo, M. Gala,F.Dı´az, J. Masson, " Upconversion luminescence of Tm^{3+} sensitized by Yb^{3+} ions in monoclinic $KGd(WO_4)_2$ single crystals", *Optical Materials*., vol.30., no. 2, pp. 222-226, 2007

[54] A. S. Al-Kady, M. Gaber, M. M. Hussein, and E. Z. M. Ebeid, "Structural and fluorescence quenching characterization of hematite nanoparticles," *Spectrochim. Acta - Part A Mol. Biomol. Spectrosc.*, vol. 83, no. 1, pp. 398–405, 2011.

[55] D. Liu, H. Yu, Y. Duan, Q. Li, and Y. Xuan, “New Insight into the Angle Insensitivity of Ultrathin Planar Optical Absorbers for Broadband Solar Energy Harvesting,” *Nat. Publ. Gr.*, no. August, pp. 1–8, 2016.

[56] L. Zhang, I. Álvarez-Martos, A. Vakurov, and E. E. Ferapontova, “Seawater operating bio-photovoltaic cells coupling semiconductor photoanodes and enzymatic biocathodes,” *Sustain. Energy Fuels*, vol. 1, no. 4, pp. 842–850, 2017.

[57] H. Dong, L. D. Sun, and C. H. Yan, “Basic understanding of the lanthanide related upconversion emissions,” *Nanoscale*, vol. 5, no. 13, pp. 5703–5714, 2013.

[58] F. Assa, H. Jafarizadeh-Malmiri, H. Ajamein, N. Anarjan, H. Vaghari, Z. Sayyar, and A. Berenjian, “A biotechnological perspective on the application of iron oxide nanoparticles,” *Nano Res.*, vol. 9, no. 8, pp. 2203–2225, 2016.

[59] J. Fessended, “Tuning light to kill deep cancer tumors Nanoparticles developed at UMass Medical School advance potential clinical application for photodynamic therapy,” *UMass Med. Sch. Commun.*, 2014.

[60] G. Lin, X. Wang, Y. F, and Y. KT, “Passive tumor targeting and imaging by using quantum dots,” *Int. J. Nanomedicine*, vol. 10, pp. 335–345, 2015.

Chapter 2: Synthesis and characterization techniques

2.1. Introduction

Oxides can be synthesized by all known wet chemical methods but to tailor the particle size in nano range and morphology towards a particular application still remains a challenge [1]. The synthesis of magnetic nanoparticles in the past decade has been intensively developed not only for its fundamental scientific interest but also for many technological applications: among others, medical application such as targeted drug delivery, contrast agent in magnetic resonance imaging, and magnetic ink for jet printers. To control the monodisperse size is very important because the properties of the nanocrystals strongly depend upon the dimension of the nanoparticle [2]. There is a large number of methods described for the synthesis of magnetic iron oxide [3]. The methods includes: (1) co-precipitation; is simple methods of synthesizing magnetite and other ferrite nanoparticles from ferric and ferrous salts such as nitrates, chlorides, sulfates, perchlorates, etc. With the appropriate ratios of the precursor salts, it is possible to obtain narrow size distribution of spherical nanoparticle. (2) Micro emulsion; in the micro emulsion method, co-precipitation occurs in the aqueous phase of water-in-oil emulsions controlling the particle size and size distribution in the desired proportions. Particles of a great variety of ferrites including magnetite and bismuth ferrite have been successfully prepared by this method. (3) Ball milling; by ball milling, the mechanosynthesis of nanostructures is promoted by the mechanical activation of the chemical reactions involved in the formation of the oxides. Wustite nanoparticles from metallic iron and hematite have been prepared by this method. (4) Sol gel process; the sol-gel process uses metallic alkoxides as precursors; it allows the preparation of ceramic nanoparticles of a great variety of compounds, including ellipsoidal single-crystalline nanoparticles of hematite and polycrystalline spherical nanoparticles of hematite. With a proper reduction-reoxidation process, magnetite and maghemite nanoparticles that retain their shape can be obtained [4]. (5) Microwave method; microwaves couple directly with the molecules of the entire reaction mixture, leading to a rapid rise in temperature. Since the process is not limited by the thermal conductivity of the vessel, the result is an instantaneous localized superheating of any substance that will respond to

either dipole rotation or ionic conduction of the two fundamental mechanisms for transferring energy from microwaves to the substance(s) being heated [5].

In this work, we have chosen to use sol-gel method as well as microwave method and the methods are discussed in detail in the next sections. The common methods of crystal growth are grouped into two, the vapor deposition and liquid to crystal growth. The earlier, Vapor Phased deposition includes; Evaporation Molecular Beam Epitaxy (MBE), Sputtering, Chemical Vapor Deposition (CVD) and Atomic Layer Deposition (ALD). The latter, Liquid Based Growth includes; Chemical Solution Deposition, Electrochemical Deposition, Chemical Bath Deposition (CBD), Successive Ionic Layer Adsorption and Reaction (SILAR), Langmuir- Blodgett films and Self Assembled Monolayers (SAM) and Sol gel method [6]. Even though there are several means to grow crystals, as mentioned above, however our interest is on Sol-gel method and microwave synthesis. Both methods allows us to control the size of the material. Sol-gel takes longer to prepare and microwave only takes few minutes. The nanomaterials were then characterized to obtain the structural, optical and luminescent information. Several techniques were used to achieve this goal, such as X-ray diffraction, scanning electron microscopy, photoluminescence spectroscopy, thermoluminescence spectroscopy, ultraviolet-visible absorption spectroscopy, X-Ray photoelectron spectroscopy, vibrational electron microscopy. Better understanding of each of the techniques are outlines in this chapter.

Synthesis methods:

2.2. Advantages of sol-gel

Sol-gel method is based on a well-established colloidal chemistry technology, which offers a possibility to produce various materials with novel, predefined properties in a simple process and at relatively low process cost. The sol is a name of a colloidal solution made of solid particles few hundred nm in diameter, suspended in a liquid phase and the gel can be considered as a solid macromolecule immersed in a solvent [7].

For the production of new porous nanomaterials, with well-defined structures and complex shapes, sol-gel method has been widely used by researchers. The method is known for being relatively

simple and it allows the control of the distribution of the components in molecules, through pre-orientation applications of the networks. Thus, potential applications of the materials synthesized by this method can be competitive [8]. The French chemist, J. J. Ebelmen in 1842, synthesized uranium oxide by heating the corresponding hydroxide [9]. In 1950, Ro and co-workers made the sol gel silica powders popular in the market by changing the traditional sol-gel process into the synthesis of new ceramic oxide. Thereafter, in 1971, the production process of low-bulk density silica (TEOS) in the presence of cationic surfactants was patented [8].

The processing steps involved in making sol-gel derived α-Fe_2O_3 are as follows: step 1 is a mixing step of a suspension of a sol, which is formed by mixing of colloidal particles in water at a pH that prevent precipitation.

$$\mathbf{Fe(NO_3)_3.9H_2O + 6\ H_2O \rightarrow Fe(H_2O)_6^{3+} + 3\ NO_3}$$

Step 2, the liquid alkoxide precursor is hydrolyzed by mixing with water

$$\mathbf{Fe(H_2O)_6^{3+} \rightarrow FeOOH + H + 4\ H_2O}$$

Step 3 a condensation takes place to form α-Fe2O3

$$\mathbf{2\ FeOOH \rightarrow \alpha\text{-}Fe_2O_3 + 2\ H_2O}$$

The physical characteristics of the gel network depends upon the size of particles and extent of cross-linking prior to gelation. The viscosity increases sharply at gelation, and a solid object results in the shape of the mold. The aging of the gel involves maintaining the cast object for a period, hours to days, completely immersed in liquid. Polycondensation continues along with localized solution during aging and reprecipitation of the gel network, which increases the thickness of interparticle necks and decrease porosity. The strength of the gel thereby increases with aging. An aged gel must develop sufficient strength to resist cracking during drying. During drying the liquid is then removed from the interconnected pore networks [10]. The sol-gel method can results in different structures of the nanomaterials powders [11], thin film [12]and fibers [13].

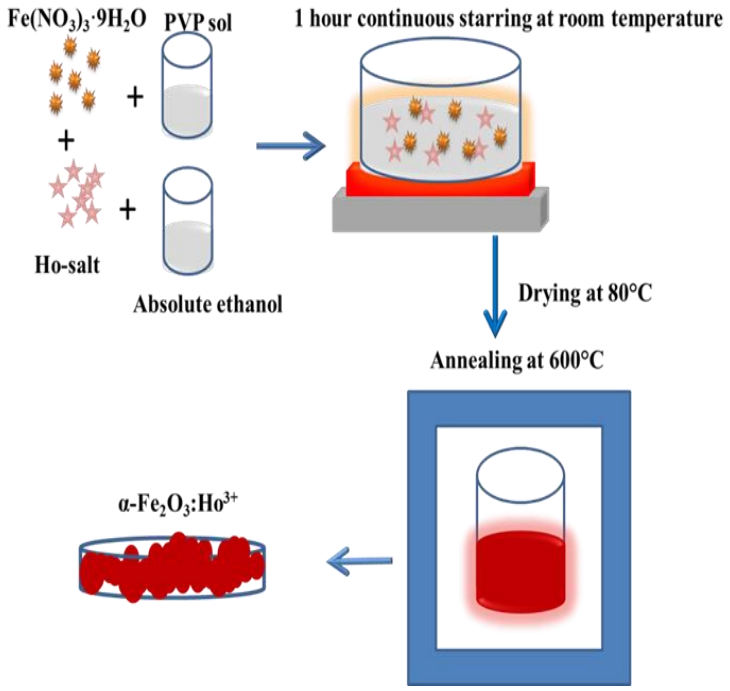

Figure 2. 1 Schematic representation of sol-gel processes.

Sol-gel have the following advantages:

- Provides excellent adhesion between the metallic substrate and the top coat by producing thin bond coating.
- Produce thick coating to provide corrosion protection.
- Easily shape materials into complex geometries in a gel state.
- Also produce highly pure products because of the organo-metallic precursor of the desired ceramic oxides that can be mixed, dissolved in a specified solvent and hydrolyzed into a sol, and subsequently a gel. The resulting composition can be highly controlled.
- And it is cost effective [14].

2.3 Advantages of microwave Synthesis

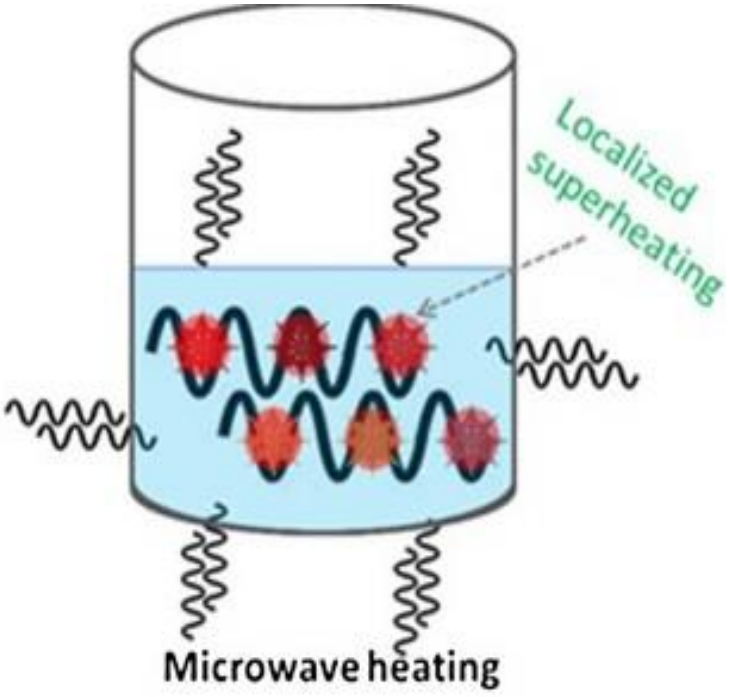

Figure 2. 2 ***Microwave heating mechanism [18].***

A microwave is a form of electromagnetic energy, which is defined in a measurements of frequency as 300 to 300000 Megahertz which falls at the lower end of the electromagnetic spectrum, corresponding to wavelength of 1 cm to 1 m. The microwave region of the electromagnetic spectrum lies between infrared and radio frequencies. The RADAR transmissions uses the wavelength between 1 cm and 25 cm, and the rest is used for telecommunications. Most commercial and domestic microwaves ovens operates at 2450 MHz (12.25 cm) to avoid interference with the RADAR and telecommunications activities [15]. Microwave heating has become widely used as a rapid heating method for the synthesis of magnetic iron oxide nanoparticles. As compared to conventional heating methods, microwave heating reduces the reaction time and increases product yield [16]. Microwave radiation heats materials through much more efficient dielectric heating, and this occurs as molecular dipoles attempt to align with the alternating electric field. Hence, the heating phenomenon depends on a substance's ability to absorb microwaves and convert the energy to heat; generally, more polar solvents, reagents, and catalysts are more efficiently heated. Microwave preparations in the case of nanoparticles synthesis has yield greater control of size and disparity as well as enhanced crystallinity [17].

In microwave synthesis, the microwave couples directly with the molecules of the entire reaction, leading to rapid rise in temperature, as shown in Fig 2.2. Since the thermal conductivity of the vessel is not limited, the results are instantaneous localized superheating of any substance that will respond to either dipole rotation or ionic conductivity- which are the two fundamental mechanism for transferring energy from microwaves to the substance being heated. The Arrhenius equation ($k = Ae^{-Ea/RT}$) determines the rate of reaction, where T is the absolute temperature that controls the kinetics of the reaction. The microwave radiation directly activate most molecules that possess a dipole or are ionic. Since energy transfer occurs in less than a nanosecond (10^{-9} s), the molecules are unable to completely relax or reach equilibrium. This then creates a state of non-equilibrium that results in a high instantaneous temperature (T_i) of molecules and is a function of microwave power input. Thus, the greater the intensity of microwave power being administered to a chemical reaction, the higher and more consistent T_i will be [5]. Microwave also have the following advantages: Exhibit order of magnitude enhancement in reaction rate as compared to conventional system. Microwave reactor can be operated in various ways, such as by varying the rate at which the temperature is increased, microwave power, stirring of the reaction system. Use of microwave saves energy because of fast kinetics, rapid heating, and short reaction time [19]

Characterization techniques:

2.4. X-Ray Diffraction

X-ray diffraction (XRD) is an efficient analytical technique used to determine crystal phases, and it can also be used to determine the grain size, lattice constants, strain analysis and degree of crystallinity in a mixture of amorphous and crystalline substance [20]. In XRD, the electrons around the atom will start to oscillate with the same frequency as the incoming beam when the x-ray beam hits an atom. A destructive interference will occur in almost all the directions, that is, the combining waves are out of phase and there is no resultant energy leaving the solid sample. However, the atoms in a crystal are arranged in a regular pattern, and in a very few directions we will have constructive interference. The waves will be in phase and there will be well-defined x-ray beam leaving the sample at various directions. Hence, a diffracted beam may be described as a beam composed of a large number of scattered rays mutually reinforcing one another [21].

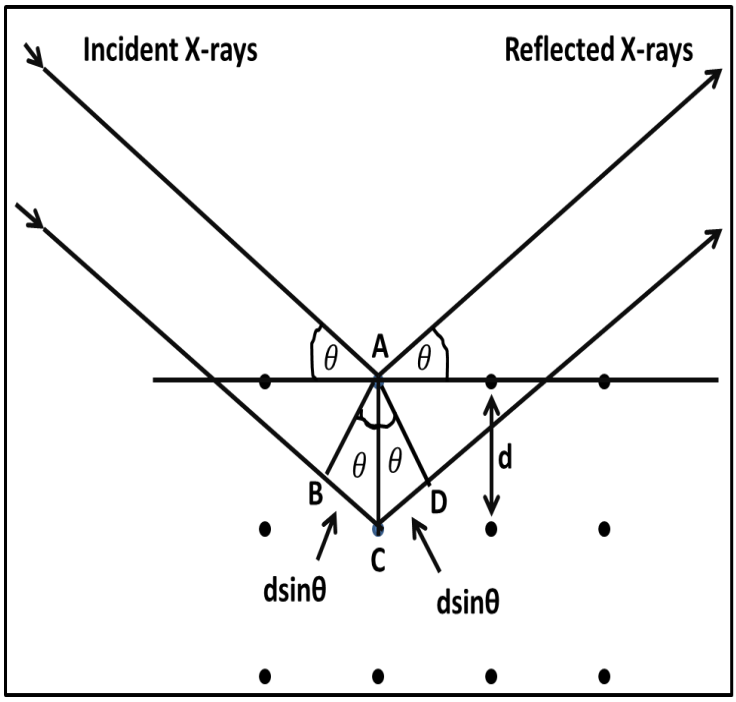

Figure 2. 3 Scatter and diffraction from an ordered arrangement of atoms [22].

Fig 2.3 shows the construction needed to derive Bragg's law. This is a central law to the analysis of diffraction data. It relates the angle θ (at which there is a maximum in diffracted intensity) to the wavelength λ of x-rays and the inter-layer distance d between the planes of atom/ ions/ molecules in the lattice. The interplanar spacing, *d*, sets the difference in path length for the ray scattered from the top plane and the ray scattered from the bottom plane. From Fig 2.3, the path length is 2*d* sin*θ*. Constructive wave interference occurs when the difference in path length for the top and the bottom rays is equal to one wavelength, λ:

$$2d \sin\theta = \lambda. \qquad 2.1$$

The right side of Eq. 1 sometimes is multiplied by an integer, n, since this condition also provides constructive interference. In our conversion, we set n = 1. When the path length difference of nλ between adjacent planes, *d*, is changed, a diffraction pattern from a material typically contains many distinct peaks, each corresponding to a different interplanar spacing, *d*. For a cubic crystal with lattice parameter a_0, the interplanar spacing, d_{hkl}, of planes labelled by miller indices (*hkl*) are [22]:

$$d_{hkl} = \frac{a_0}{\sqrt{h2+k2+l2}}. \quad 2.2$$

Diffraction experiments are generally made at a fixed wavelength; thus a measure of the diffraction angle will allow the associated *d*- spacing to be calculated. When a crystal with a fixed 2*d* spacing receives an incident beam, according to Bragg's law, each unique wavelength will be diffracted at a unique diffraction angle. Thus, when the diffraction angle 2θ is known, then wavelength of the incident beam can be determined, if the *d*-spacing of the crystal is known [23].

2.5. Transmission Electron Microscopy

Transmission electron microscopy (TEM) (Fig 2.4) is a technique used to analyze the morphology, defects, crystallographic structure, particle size and the elemental composition of the specimen. In this technique, the beam of electrons transmits through an extremely thin specimen, and then interacts with the specimen when passing through it. From the interaction of the electrons that are eventually transmitted through the specimen, an image is formed, which is magnified and focused onto an imaging device, such as CCD camera. TEM uses the electrons as a light source, which their much lower wavelength are making it possible to get a resolution that is a thousand times better than that of a light microscope [20].

The TEM possibility of high magnification has made it a valuable tool in medical, biological and material sciences research. The specimen must be thin in this case and able to withstand the high vacuum present inside the instrument's sample chamber [24]. If the specimen is thicker, fewer electrons are forward scattered and more are backscattered. The backscattered electrons are the only remnants of the incident beam for bulk, non-transparent specimen. [25].

The system can also be used for the determination of the electron diffraction patterns of the crystalline structures. A crystalline material interacts with the electron beam mostly by diffraction rather than absorption. The intensity of the transmitted beam is affected by the volume and density of the material through, which it passes. The intensity of the diffraction depends on the orientation of the planes of atoms in a crystal relative to the electron beam. At certain angles the electron beam is diffracted strongly from the axis of the incoming beam, while at other angles the beam is largely transmitted [24].

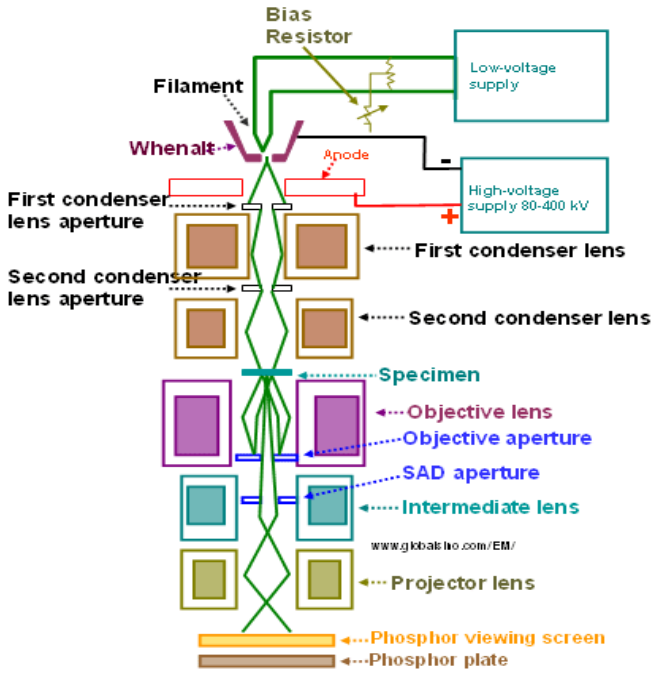

Figure 2. 4 Schematic representative of transmission electron microscopy [26].

2.6. Scanning Electron Microscopy

Scanning Electron Microscopy (SEM) is an instrument for observing and analysing the surface microstructure of a bulk sample using a finely focused beam of energetic electrons. An electron-optical system is used to form the electron probe which may be scanned across the surface of the sample in a raster pattern. Various signals are generated through the interaction of the beam with the sample. These signals may be collected or organized with the application of appropriate detectors. For imaging, the signal amplitude obtained at each position in the raster pattern may be assembled to form an image [27].The microscope commonly uses a lanthanum hexaboride filament as the source of electrons, and its vacuum is often achieved by pumping the system with a turbo molecular and an ion pumps. The technique can provide information about the material, topology and morphology. If the system is equipped with an energy dispersive x-ray spectrometer (EDS), it can also provide information about chemical composition of the material [28]. The SEM electron column consist of an electron gun, two or more electromagnetic lenses operating in vacuum. The electron gun generate free electrons and accelerate these electrons to energies in the range 1 – 40 KeV in the SEM. The focused electron probe on the specimen which is small is

created by the electron lenses. For an image to be produced the electron beam is focused into a fine probe and scanned across the surface of the specimen with the help of scanning coil. The signal in the form of electromagnetic radiation is emitted when the accelerated electrons struck each point of the specimen [29].

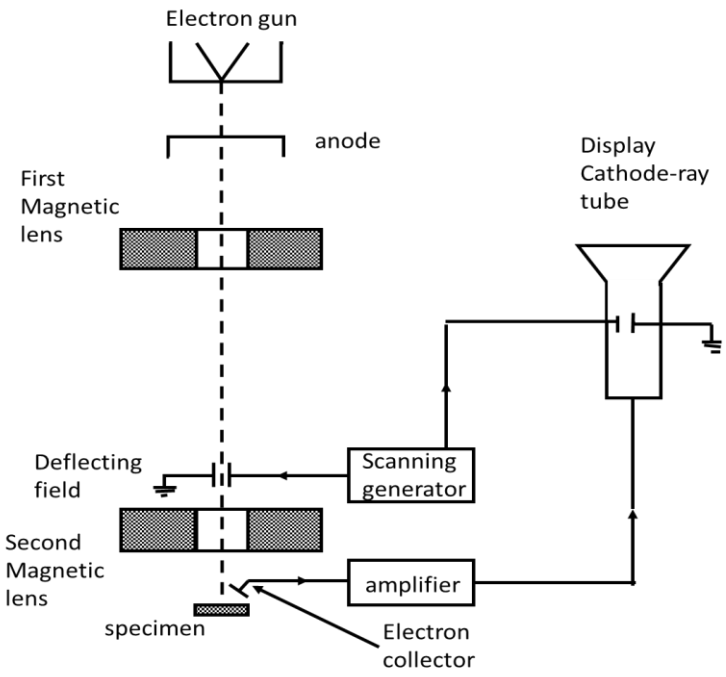

Figure 2. 5 The reduced form of the scanning electron microscopy. Many variants are possible on this basic theme such as different lenses, guns, deflecting field, detectors, amplifiers and display schemes, but all of these items must be present in one form or another [31].

The basic principle of the SEM is that, when the beam of electrons interacts with the specimen, the electrons are scattered within the specimen and gradually lose their energy, then they are absorbed in the specimen. Depending on the electron energy, the atomic number of the elements making up the specimen and the density of the constituent atoms: the scattering range of the electrons inside the specimen is different. When the incident beam enters the specimen, it produces secondary electrons from the emission of the valence electrons of the constituent atoms in the specimen. Since the energy of the secondary electrons is very small, the specimen quickly absorbs those generated at a deep region. Only those generated at the top of the specimen are emitted

outside of the specimen. Thus, the secondary electrons are used to observe the topography of the specimen surface [30]. The advantages of the scanning electron microscope evolve from the fact that the surface of a solid specimen is available for experimentation, including simple observation, at a resolution much better than that of the optical microscope and with a depth of field that is orders of magnitude greater [31].

2.7. X-Ray Photoelectron Spectroscopy

For compositional and chemical state analysis, x-ray photoelectron spectroscopy (XPS) has been widely used because it is a versatile surface and analytical technique. The XPS technique causes very little charging in samples, since the x-rays are used for the incident beam and thus it is useful for both electrically conductive and non-conductive materials. For the electron energies that are normally used in XPS, the attenuation lengths are about 1 – 10 monolayers for the emission angles normal to the surface [32]. When an experiment is carried out in an XPS, the sample is exposed to the flux of nearly monoenergetic radiation with mean energy *hv,* and then observing the resultant emission of photoelectrons, whose kinetic energies will be described most simply by the photoelectric equation, these phenomena are shown in Fig 2.6:

$$h\nu = E_b{}^{V}{}_{(K)} + E_{kin} \qquad 2.3$$

Where, $E_b{}^{V}(K)$ is the binding energy and E_{kin} is the photoelectron kinetic energy. Both Auger lines and secondary electrons, in general will also be emitted from the sample, however, it is possible to distinguish these electrons from true photoelectrons. The kinetic energy, directions of emission with respect to the sample and the exciting radiation are the three fundamental properties characterizing each emitted photoelectron [33].

XPS spectrum is presented as the photoelectron counts as a function of binding energy, which is achieved by just measuring the kinetic energy of the photo electrons accelerated up the column of hemispherical analyser. All elements can be detected except for H and He. The binding energies of the photoelectrons depend on the chemical environment of the atoms. The information about chemical state of the elements are given by the accurate measurements of the exact peak position [34].

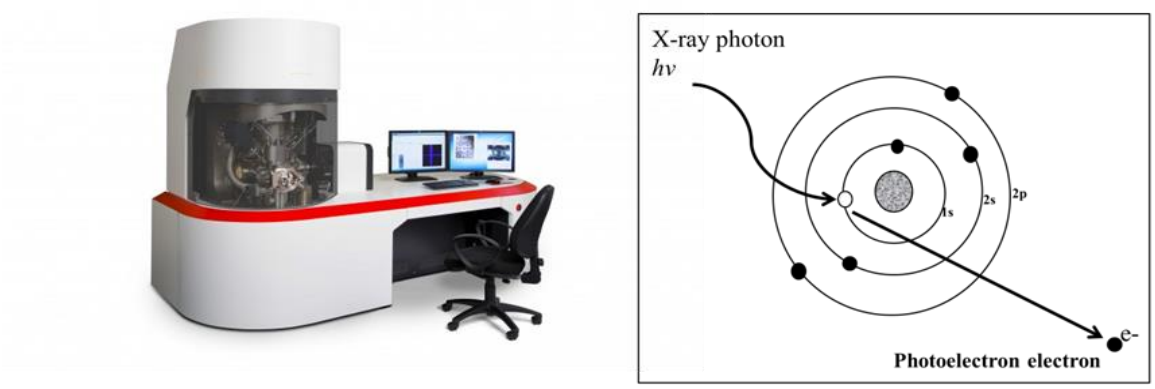

Figure 2. 6 (a) X-ray photoelectron spectroscopy image and (b) the XPS process [33].

2.8. UV-Vis Spectroscopy

A number of processes can occur when radiation interacts with matter, these include, reflection, scattering, absorption, fluorescence/phosphorescence and photochemical reactions (as shown in Fig 2.7). The UV-Visible spectroscopy is designed to detect the transmitted and reflected radiation by a sample in order to provide an indication of the amount of the absorbed radiation. The total potential energy of a molecule generally is represented as the sum of its electronic, vibrational and rotational energies:

$$E_{total} = E_{elctronic} + E_{vibrational} + E_{rotational} \quad 2.4$$

The amount of energy a molecule possesses in each form is not a continuous but a series of discrete levels or states. The difference in energy among the different states is in the following order [35]:

$$E_{electronic} > E_{vibrational} > E_{rotational} \quad 2.5$$

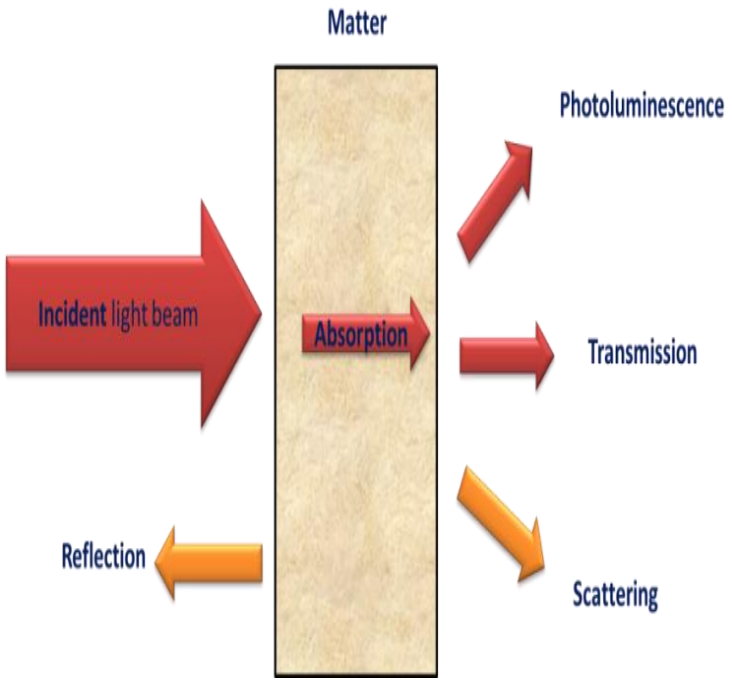

Figure 2. 7 UV-Vis phenomena when the incident light beam interact with matter [36].

When the light passes through a sample, the amount of light absorbed is the difference between the incident radiation (I_0) and transmitted radiation (I). The amount of light absorbed is expressed as either transmittance or absorbance. Transmittance usually is given in terms of a fraction of 1 or as a percentage and is defined as follows [37]:

$$T = \frac{I}{I_0} \text{ or } \%T = \left(\frac{I}{I_0}\right) * 100 \qquad 2.6$$

Absorbance is defined as follows:

$$A = -\log T \qquad 2.7$$

The spectrophotometer consists of a light source, a filter, a monochromator, beam splitter, a cuvette for sample solution, a photoelectric detector and a digital display (as shown in Fig 2.8). It also consists of two devices, a spectrometer and a photometer. A spectrometer, produces a desired range of wavelength of light. A beam of light is transmitted from a collimator that passes through a monochromator to split it into several components of wavelength. The only desired wavelength

is then transmitted by a wavelength selector. A photometer, then detect the amount of photons that is absorbed and then sends a signal to a digital display [38].

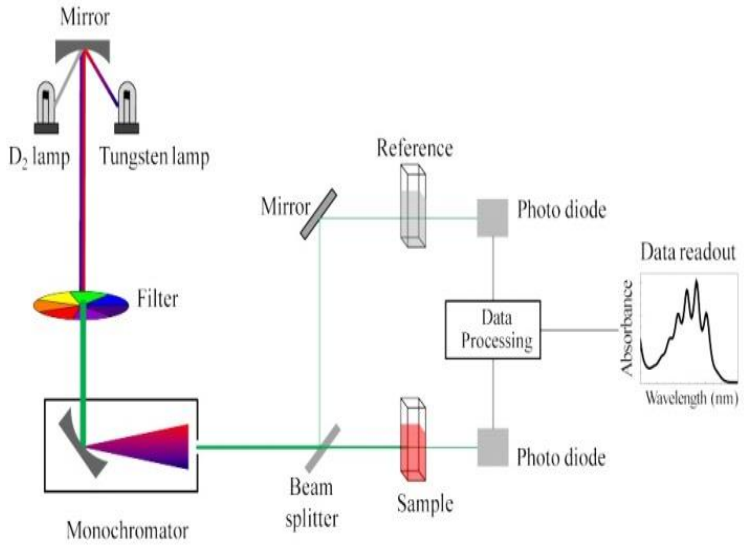

Figure 2. 8 Basic schematic representation of spectrophotometer [39].

2.9. Photoluminescence Spectroscopy (Fluorolog3)

Photoluminescence is defined as the spontaneous emission of light from a material under optical excitation. It can therefore be used to provide detailed information on discrete electronic states involving both intrinsic and extrinsic defects. This is achieved by applying an external light with energy $h\nu \approx E_G$, where E_G denotes the energy band gap, and detecting the re-emitted photons [40]. During this process a light is irradiated onto a sample, where it is absorbed and imparts excess energy into the material in a process called photo-excitation. The emission of light or luminescence is one of many ways in which the excess energy can be dissipated by the excited electrons, when they de-excite to their ground state. The luminescence derived from exciting a sample with photons is called photoluminescence. The energy of the emitted light relates to the difference in energy levels between the two electrons states involved in the transition between the excited state and equilibrium state [41] as shown in Fig 2.9 (a).

The Fluorolog 3 spectrofluorometer instrument was used to characterize Fe_2O_3, and it is capable of acquiring both phosphorescence and fluorescence spectral data. The excitation source is

equipped with a 450 W continuous xenon lamp as an excitation source for steady state measurements, and a flashing Xenon Lamp for decay curve measurements. The monochromator, sample compartment, detector and accessories are the four basic components of Fluorolog 3, as shown in Fig 2.9 (b). The double grating monochromator in the excitation and emission path are responsible for the system's considerable increase in sensitivity, resolution, and stray-light rejection. The sample compartment is a T-box with two options of emission signal collecting, namely, the front-face emission collection for solids samples and the right-angle emission for solution samples [42].

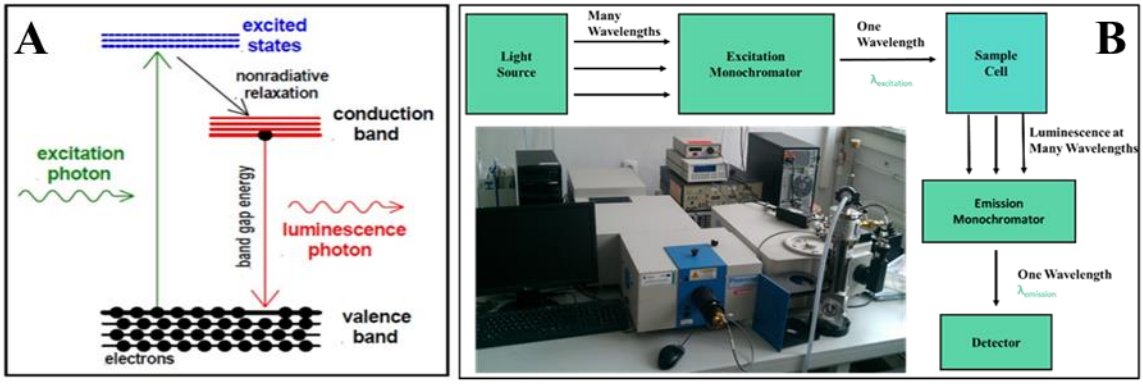

Figure 2. 9 (a) Principle of photoluminescence spectroscopy (PL), (b) Essential of a luminescence experiment. The sample is irradiated at one wavelength and emission is observed over a range of wavelengths. The excitation monochromator selects the excitation wavelength and the emission monochromator selects the one wavelength at a time to observe [43].

Fluorolg 3 is not limited to only steady state measurements, it also measures lifetime, both short time and long lifetime measurements. Time-correlated single-photon counting (TCSPC), is used for time-domain lifetime measurements. In TCSPC, the excitation light is pulsed, ideally with a pulse-width shorter than the luminescent lifetime. The emission from the sample is collected from a series of repeated pulses, with the time of arrival of these photons binned into channels. The fluorescence from the series of excitation pulses builds up a decay curve, from which the lifetimes of all sample components are calculated [44].

2.10. 980 Laser diode system

High-Power 980-nm lasers are the key components in erbium– doped amplifiers, which are critical to high –capacity communication system. The main forces driving towards high power pump laser are the increase number of channels, higher grain for loner reach, and small form factors for the amplifiers. There has been much effort toward improving chip and module power in recent years. The challenge would be to push the laser diode to even high power while also maintaining the lasing with single-mode operation since operation approaches the physical limits. The reliability, in addition to performance has always been a critical requirement for high-power 980-nm pumps since the laser facet is very susceptible to failure caused by higher power satisfying the Telcordia qualification standards [45**]**. In this work, the FLS980 spectrometer was used to investigate luminescence properties. The FLS980 is a computer controlled modular spectrofluorimeter for measuring steady state luminescence spectra in the ultraviolet to near infrared range with single photon counting sensitivity. It combines ultimate sensitivity with high spectral resolution and excellent stray rejection. The performance of the FLS980 makes it ideally suited for demanding applications in the broad areas of photophysics, photochemistry, biophysics and materials research [46].

In fluorescence measurements, the sample (liquid or solid) is excited with a light of one wavelength and then measuring difference light (luminescence) which is emitted. The equipment consist of a xenon lamp with double monochromator to provide continuous excitation and laser with optical parametric oscillator (OPO) to provide pulsed excitation, both of which can be tuned to different wavelength starting at about 200 nm in the far violet region. The system also has a powerful fixed wavelength infrared laser for up-conversion studies and several very fast pulsed fixed wavelength erasable programmable logic device (EPLD) light sources in the UV for lifetime measurements. Luminescence is detected using two possible PMTs (photomultiplier tubes), one sensitive in the visible part of the spectrum and another in the infrared region, or with a CCD (charge coupled device) camera which is less sensitive but faster. Both excitation and emission spectra will be corrected for the spectral response of the system e.g. the efficiency of light sources, mirrors, diffraction gratings, optical filters and detectors. An integrating sphere is provided to capture light emitted from the samples in different directions for quantum yield measurements and a cryostat is provided so that samples can be cooled from room temperature to about 10 K on the absolute

temperature scale. By monitoring the emission of samples after pulsed excitation using the PMTs and fast photon-counting electronics, the system can be used to measure the lifetime of phosphorescent materials. The system includes variable slits and filters and is controlled through a single software package, while an advanced software package for the analysis of time-resolved data is also included. The schematic diagram of the system is shown in Fig 2.10 [47].

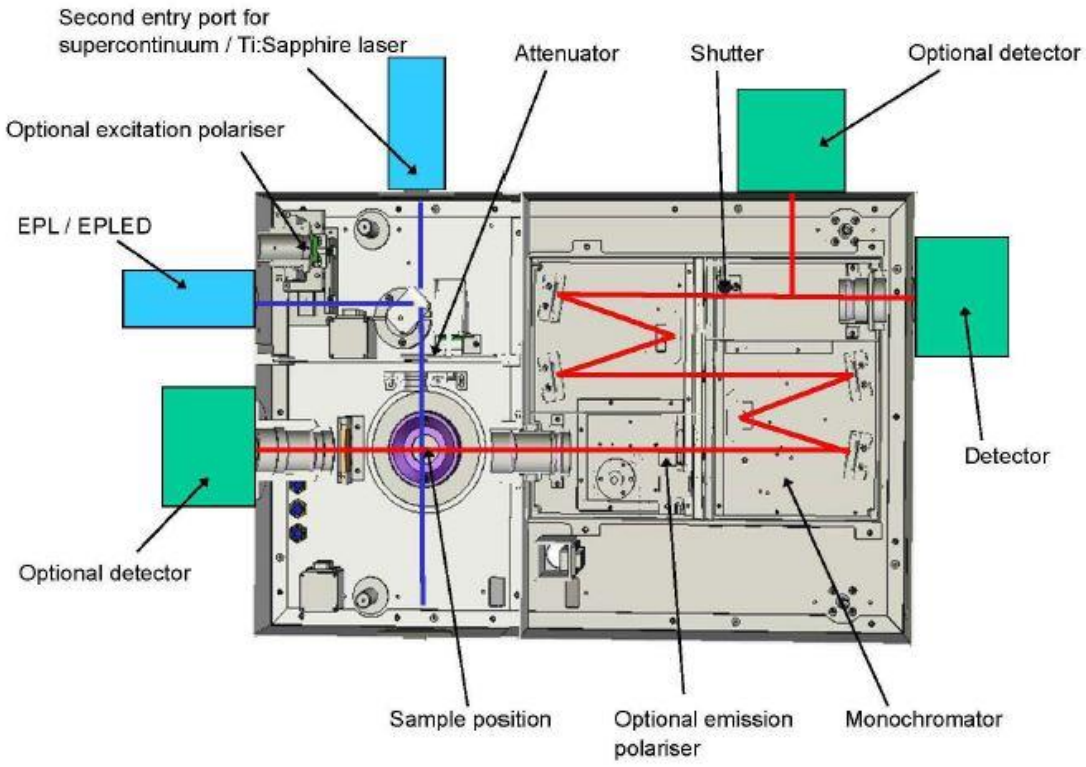

Figure 2. 10 Schematic diagram of FLS980 spectrophotometer [47].

2.11. Vibrational sample magnetometer

The Vibrational sample magnetometry (VSM) is a measurement technique which allows to determine the magnetic moment of a sample with very high precision. The VSM is based on Faraday's law, which states that an electromagnetic force is generated in a coil when there is a change in flux through the coil. In the measurements setup, a magnetic sample is moving in the proximity of two pickup coils as shown in Fig 2.11.

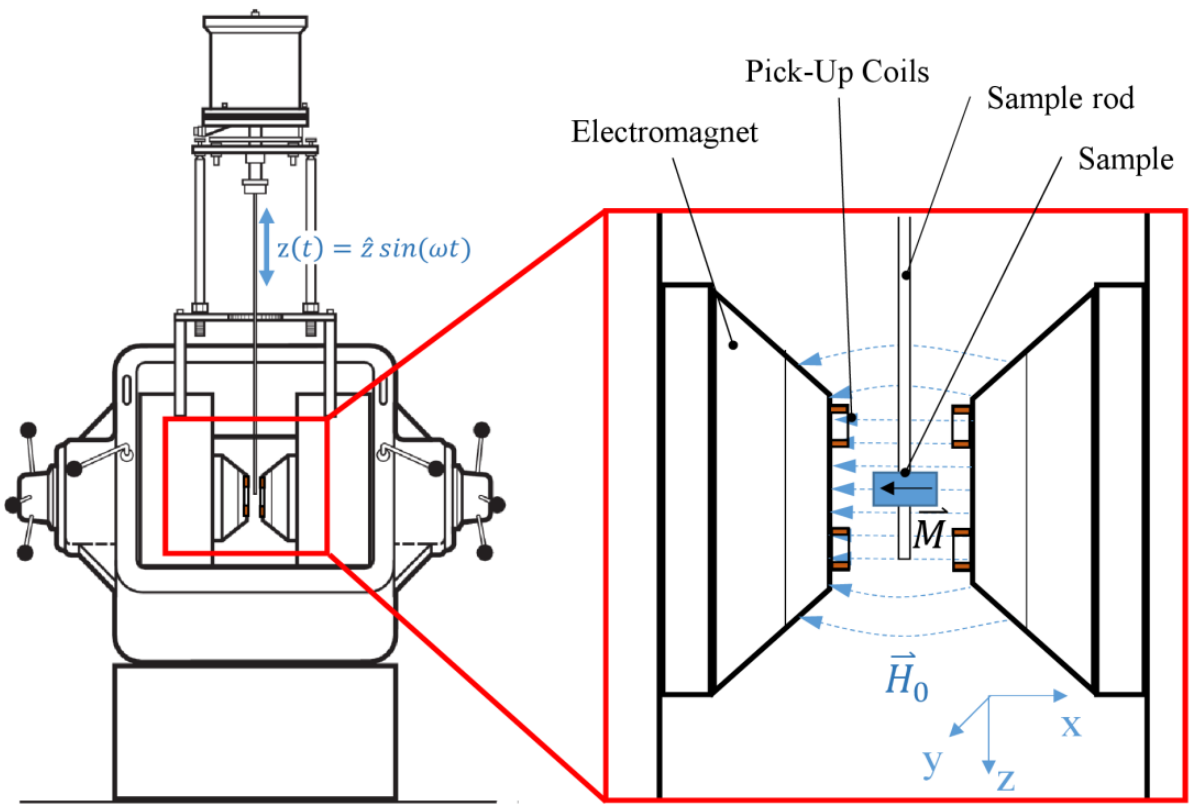

Figure 2. 11 Schematic representation of a VSM [49].

The VSM systems are used to measure the magnetic properties of materials as a function of magnetic field, temperature and time. They are ideally suited for research, production testing, quality and process control. Powders, liquids, solids, single crystals and thin films are all readily accommodated in a VSM [48]. A sinusoidal signal is provided by the oscillator and translated by the transducer assembly into a vertical vibration. The sample is fixed to the sample rod and vibrates with a given frequency and amplitude. It is centered between the two pole pieces of an electromagnet that generated a magnetic field $\bar{H}_0$ of high homogeneity. Stationary pickup coils are mounted on the poles of the electromagnet. Their symmetry center coincides with the magnetic center of the static sample. Hence, the change in magnetic flux originating from the vertical movement of the magnetized sample induces a voltage U_{ind} in the coils. When homogeneous field $\bar{H}_0$along the *x* axis is brought to the sample, it will be magnetized along the direction of the field, resulting in a magnetic moment $\bar{m}$ of the sample. Then, the sample will be moved periodically

relative to the pickup coils. The measurement setup is sensitive even to very low magnetic moments. Today's vibrating sample magnetometers are able to detect magnetic moments of down to the μemu range, which corresponds to approx. 10^{-9} g of iron [49].

References

[1] M. Mohapatra and S. Anand, "Synthesis and applications of nano-structured iron oxides / hydroxides – a review," *Multicr. Int. J. Eng. Sci. Technol.*, vol. 2, no. 8, pp. 127–146, 2010.

[2] S. Laurent, D. Forge, M. Port, A. Roch, C. Robic, L. Vander Elst, and R. N. Muller, "Magnetic iron oxide nanoparticles: Synthesis, stabilization, vectorization, physicochemical characterizations and biological applications," *Chem. Rev.*, vol. 108, no. 6, pp. 2064–2110, 2008.

[3] M. Geppert, "Synthesis and Characterization of Iron Oxide Nanoparticles and Investigation of their Biocompatibility on Astrocyte Cultures," thesis, 2012.

[4] M. A. G.-L. and D. L. P. Arturo I. Martinez1, "study of the p roperties of iron oxide nanostructures," in *Research in Nanotechnology Developments*, 2009, pp. 183–194.

[5] B. Hayes, "Recent advances in microwave-assisted synthesis," *Aldrichimica Acta*, vol. 37, no. 2, pp. 66–76, 2004.

[6] V. Okpala, D., Uche, "Sol-gel technique: A veritable tool for crystal growth," *J. Appl. Sci. Res.*, vol. 4, no. 1, p. 506–510., 2013.

[7] C. . Brinker, A. . Hurd, P. . Schunk, C. . Ashely, R. . Cairncross, J. Samuel, K. . Chen, C. Scotto, and R. . Schwartz, "'Sol-Gel Derived Ceramic Films--Fundamentals and Applications'," *Metall. Ceram. Prot. Coatings*, no. I, pp. 112–151, 1996.

[8] C. a Milea and C. Bogatu, "The Influence of Parameters in Silica Sol-Gel Process," *Bull. Transilv. Univ. Brasov Eng. Sci.*, vol. 4, no. 1, pp. 59–66, 2011.

[9] D. Co-supervisor, "luminescence investigation of zinc oxide nanoparticles guy leba kabongo for the degree of november 2013," no. November, 2013.

[10] L. L. Hench and J. K. West, "The sol-gel process," *Chem. Rev.*, vol. 90, no. 1, pp. 33–72, 1990.

[11] A. S. Teja and P. Y. Koh, "Synthesis, properties, and applications of magnetic iron oxide nanoparticles," *Prog. Cryst. Growth Charact. Mater.*, vol. 55, no. 1–2, pp. 22–45, 2009.

[12] S. Suresh, "Semiconductor Nanomaterials, Methods and Applications: A Review," *Nanosci. Nanotechnol.*, vol. 3, no. 3, pp. 62–74, 2013.

[13] M. Niederberger, "Aqueous and Nonaqueous Sol-Gel," in *Metal Oxide Nanoparticles in*

Organic Solvents, 2009, pp. 7–19.

[14] S. Technique, “Sol-Gel Deposition,” *Ceramics*, pp. 2–5, 2006.

[15] S. Ravichandran and E. Karthikeyan, “Microwave synthesis - A potential tool for green chemistry,” *Int. J. ChemTech Res.*, vol. 3, no. 1, pp. 466–470, 2011.

[16] M. Schiavoni, “Synthesis of Magnetic Iron Oxide Nanoparticles Magnetic.” microwave-enhanced science, pp. 1-2,

[17] E. A. Osborne, T. M. Atkins, D. A. Gilbert, S. M. Kauzlarich, K. Liu, and A. Y. Louie, “Rapid Microwave-Assisted Synthesis of Dextran-Coated Iron Oxide Nanoparticles for Magnetic Resonance Imaging,” *Nanotechnology*, vol. 23, no. 21, p. 215602, 2012.

[18] Veera Gnaneswar Gude, Prafulla Patil , Edith Martinez-Guerra , Shuguang Deng and Nagamany Nirmalakhandan, "Microwave energy potential for biodiesel production", *Sustainable Chemical Processes*, vol. 1, no. 5, 2013

[19] Y.-J. Zhu and F. Chen, “Microwave-Assisted Preparation of Inorganic Nanostructures in Liquid Phase,” *chemical reviews*, dx.doi.org/10.1021/cr400366s, 2013.

[20] N. H. Patel, “Basic Principle, Working and Instrumentation of Experimental Techniques,” PhD thesis, 2015.

[21] T. ART, “Basics of X-ray Diffraction,” in *Introduction to powder/polyscrystalline diffraction*, pp. 1–22, 1999.

[22] B. Fultz and J. M. Howe, *Transmission Electron Microscopy and Diffractometry of Materials (Third Edition)*. 2007.

[23] R. Jenkins, “X-ray Techniques : Overview,” *Encycl. Anal. Chem.*, pp. 13269–13288, 2000.

[24] M. S. Dhlamini, “Luminescent Properties of Synthesized PbS Nanoparticle Phosphors,” MSc thesis, 2008.

[25] A. R. Barron, “Transmission Electron Microscopy : An Overview,” *Phys. methods Chem. nano Sci.*, vol. 1, no. 1, pp. 3–10, 2014.

[27] J. Mabon, W. Swiech, H. Zhou, M. Bresim, and C. Chiritescu, “Scanning Electron Microscopy (SEM) and Focused Ion Beams (FIB) in Materials Research,” *6th Advanced Materials Characterization Workshop*, 2014. .

[28] B. Hafner, “Scanning Electron Microscopy Primer,” *Characterization Facility, University of Minnesota, pp.1-29*, 2007. .

[29] M.T Postek, K. S Howard, A. H Johnson and K. L McMichael, 'brief introduction to

scanning elctron microscopy (SEM)', pp. 1-8

[30] Jeol, “Scanning Electron Microscope a to z,” *Serv. Adv. Technol.*, pp. 32, 2006.

[31] W. C. Nixon, “The General Principles of Scanning Electron Microscopy,” *Philos. Trans. R. Soc. London*, vol. 261, no. 837, pp. 45–50, 1971.

[32] T. Yamashita and P. Hayes, “Analysis of XPS spectra of Fe^{2+} and Fe^{3+} ions in oxide materials,” *Appl. Surf. Sci.*, vol. 254, no. 8, pp. 2441–2449, 2008.

[33] C. S. Fadley, “X-Ray photoelectron spectroscopy,”*Electron Spectroscopy: Theory, Techniques, and Applications*, vol. 2, 1987, pp. 1–155.

[34] K. P. Electronics, “X-Ray Photoelectron Spectroscopy (XPS / ESCA),” *Philips*, 2008.

[35] J. Fraunhofer and G. Kirchhoff, “Fundamentals of UV-visible spectroscopy,” *Microwaves*, pp. 79–88, 2002.

[36] Ashathy j, "UV & Visible spectroscopy: introduction, theory, law, limitation", *department of pharmaceutical chemistry Ezhuthachan college of pharmaceutical science,*

[37] S. Kumar, “Spectroscopy of Organic Compounds,” *Dept. Chem.*, vol. 66, pp. 1–36, 2006.

[38] F. M. Sanda, M. E. Victor, T. A. Monica, and C. Alina, “Spectrophotometric Measurements Techniques Fermentation Process (Part One): Base Theory for Uv-Vis Spectrophotometric Measurements,” *Hungary-Romania Cross-Border Co-operation Program.*, pp. 1-16, 2012.

[39] https://en.wikipedia.org/wiki/File:Schematic_of_UV-_visible_spectrophotometer.png, 27/02/2018

[40] P. Spectroscopy, “Review of experimental methods,” pp. 16–23.

[41] a. R. Baron, “Photoluminiscence spectroscopy and its applications,” *Phys. Methods Chem. Nano Sci.*, pp. 295–305, 2012.

[42] M. M. Colen, “Synthesis and Characterization of Long Persistent Phosphors Using Combustion Method,” *MSc thesis*, 2015.

[43] Ruquan Ye and Andrew R. Barron, "*photoluminescence spectroscopy and its applications*", OpenStax-CNX module: m38357 Vol. 1.2, 2011

[44] Horiba, “Fluorolog®-3 with FluorEssence™,” no. May. 2014.

[45] Guowen Yang, Gary M. Smith, Monica K. Davis, David A. S. Loeber, Martin Hu, Chung-en Zah, and Rajaram Bhat," Highly Reliable High-Power 980-nm Pump Laser", *photonics technology letters*, vol. 16, no. 11, pp. 2403-2405 2004

[46] FLS980 photoluminescence spectrometer, *Edinburgh instuments*,2015

[47] http://eqdb.nrf.ac.za/equipment/spectrometers/tuneable-laser-based-time-resolved-fluorescence-spectrophotometer-fls980.

[48] Lake Shore Cryotronics, *Magnetic Media Measurements with a VSM*, www.lakeshore.com]

[49] Christian-Albrechts-Universitat zu Kiel, Vibrating Sample Magnetometry, Basic laboratory materials science and engineering, 18.10.2016

Chapter3: Structural and Optical properties of sol-gel derived α-Fe_2O_3 Nanoparticles

3.1. Introduction

Recent developments in the field of nanomaterials is a good platform to tune their properties. This enables the properties to be reversible in a controlled manner [1]. Iron oxide has attracted a lot of attention in the field of nanotechnology due to its optical, electrical, magnetic, catalytic and chemical properties. It has potential applications in gas sensors, magnetic resonance imaging, photo-electrochemical cells, contrast agents and drug delivery. Since α-Fe_2O_3 is applied in various fields, its optical properties have been well studied, with the red emission being of greater interest [2]. Optical absorption of α-Fe_2O_3 is strong over the entire visible optical range and very weak in the infrared optical range. The color of α-Fe_2O_3 results from different types of intra electron transitions [3, 4]. Mahadeo Mahadik et al [5] synthesized α-Fe_2O_3 by varying the substrate temperature and the absorption band edge was up to 600 nm. The absorption transitions were assigned to (i) ligand to metal charge-transfer transition, (ii) Fe^{3+} ligand field transition and (iii) pair excitations resulting from the simultaneous excitations of two neighboring Fe^{3+} cations that are magnetically coupled. α-Fe_2O_3 and γ-Fe_2O_3 polymorphs are commonly utilized among various iron oxide nanoparticles, due to their unique size, architecture, chemical, electrical, magnetic, anticorrosive and optical properties. However, α-Fe_2O_3 is the most attractive and has received a lot of attention due to its high chemical stability under ambient conditions, low cost and non-toxicity [6-8].

α-Fe_2O_3 displays n-type semiconducting properties with a band gap that is approximately 2.2 eV, and this makes it to absorb and emit in the visible region of the electromagnetic spectrum. Shinder et.al [9] synthesized Al doped α-Fe_2O_3 by spray pyrolysis. The α-Fe_2O_3 showed a single hematite phase with a crystalline size 20-40 nm. The band gap increased from 2.2 to 2.25 with doping concentration which attributed to blue shift. Its conduction band (CB) is composed of empty d-orbitals of Fe^{3+} and the valence band (VB) consists of occupied 3d orbitals of Fe^{3+} with some admixture from the O 2p non-bonding orbitals. The compound exhibits rhombohedral centered hexagonal structure of the corundum type, with a closely packed oxygen lattice in which two-thirds of the octahedral sites are occupied by Fe^{3+} ions. It exhibits weak-ferromagnetic property at

room temperature, antiferromagnetic below the Morin transition temperature of 250 K and paramagnetic above the Nèel temperature of 948 K [10-12].

It is well-known that the magnetization of ferromagnetic materials has a great influence on the morphology and structure of nanoparticles [7, 13]. The ferromagnetic α-Fe_2O_3 is a good candidate for biomedical applications. Various synthesis methods enable tunable particle sizes, such that the particles can be scaled down to dimensions that are smaller than or comparable to those of the genes (2 – 10 nm), proteins (5 – 50 nm), cells (10- 100 nm) and viruses (20 – 450 nm). This demonstrates that they can target a biological entry of interest [14].

On account of the attractive scientific and industrial application of α-Fe_2O_3 nanoparticles, novel methods for their synthesis and new approaches in their characterization have been reported in recent years. It has been reported that various preparation techniques could lead to different phases or mixture of phases and different degrees of size control [15]. To exploit the interesting and useful properties of nanostructures and to apply them in technology, their controlled and well dispersed particles during synthesis is quite essential. The synthesis of α-Fe_2O_3 nanoparticles with various structural morphology have attracted much interest due to their importance to have a thorough understanding of fundamental phenomena such as light scattering, particle interaction and electrophoresis. Up to now several synthesis methods have been developed for the preparation of α-Fe_2O_3 nanoparticles which include sol-gel, hydrolysis of iron salt, hydrothermal synthesis, microwave synthesis, chemical bath deposition, combustion and chemical spray pyrolysis technique [16-18]. It has been reported that nanometer-sized particles can be grown into zero, one, two and three dimension through these synthesis methods. By far a large variety of α-Fe_2O_3 nanostructures have been synthesized, including the most common 0D spherical nanoparticles [16], 1D nanocrystals such as rod [19] wire [20] and tube [21], 2D layered structured such as nano flakes [22], and complex 3D architectures such as dendrites and snowflakes [23], as well as hollow micro-spheres [24].

3.2. Materials and methods

Several synthetic routes have been developed to acquire nanomaterials with controllable size, morphology, crystallinity and so forth. In the past decade, synthesis of iron oxide in the nano range has been the main challenge. These synthesis processes include careful control of pH, concentration of the reactants, temperature, method of mixing, and rate of oxidation. Processes such as nucleation, growth, aggregation and adsorption of impurities influence the morphology of the iron oxide particles. However, it is not possible to precipitate specific iron oxide particles in many cases directly in the desired size and shape [25].

$FeN_3O_9 \cdot 9H_2O$, polyvinyl alcohol (PVA) and absolute ethanol were used as precusors grade and were used as received without further purification. In this chapter, sol-gel method was used to synthesize the α-Fe_2O_3. $FeN_3O_9 \cdot 9H_2O$ was used as the solid starting material and was dissolved in absolute ethanol. The solution was stirred for 1 hour at room temperature. A solution of polyvinyl acetate (PVA) was prepared by dissolving in absolute ethanol at 60 °C and transferred to the solution with continuous stirring for 1 hour. The solution was then dried at 100 °C for 1 hours. The obtained powder was ground into fine powder, divided into various portions and annealed at different temperatures (300 °C and 600 °C) to obtain the crystalline phase.

The obtained powders were characterized with an X-Ray diffractometer (Rigaku Smartlab) to confirm the phase formation and the crystallinity of the samples. Diffuse reflectance measurements were carried out to extract the absorption characteristics using the Lambda 1050 UV/Vis/NIR spectrophotometer. The X-ray photoelectron spectroscopy (XPS) was used to investigate the chemical state of the materials, and the transmission electron microscopy (TEM) was used to study the surface morphology and particle size. The Fourier transmission infrared spectroscopy (FTIR) was used to investigate chemical bonding of the materials. The thermoluminescence measurements were carried out using the Riso TL/OSL reader (model TL/OSL-DA-20) equipped with a ^{90}Sr beta radiation source with a dose rate of 0.1028 Gy/s and a photomultiplier tube. A combination of BG 3 + BG 39 Schott filters were used in the system, with transmission range of 320 nm – 450 nm.

3.3. Results and discussions

3.3.1. X-Ray diffraction

The structure and phase purity of the samples were confirmed by performing powder X-ray diffraction with Cu K_α radiation of $\lambda = 1.5405$ Å at room temperature from 20 - 70°. The Rigaku SmartLab diffractometer was operated at 40 kV and 200 mA. Fig 3.1 shows the XRD pattern of α-Fe_2O_3 nanoparticles (a) as prepared, (b) annealed at 300°C and (c) annealed at 600 °C. The patterns of the as prepared sample indicate that the structure is amorphous.

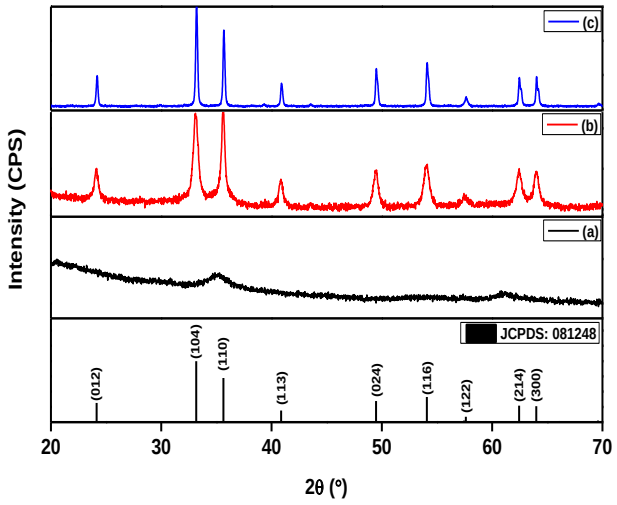

Figure 3. 1 XRD pattern of α-Fe_2O_3 nanoparticles (a) as-prepared and annealed at different temperatures (b) 300°C and (c) 600°C.

Annealing of the samples introduces peaks, and it is observed that an increase in annealing temperature significantly intensifies the peaks. This clearly indicates that the samples become crystalline when they are annealed. The patterns of the 300 ^oC annealed α-Fe_2O_3 sample indicates that the structure has initiated crystallinity, and resembles α-Fe_2O_3 polymorph. The more crystalline is observed on a sample that was annealed at 600 ^oC. According to the standard pattern of iron oxide, the sample annealed at 300 ^oC does seem to have fully crystallized into the desired polymorph (α-Fe_2O_3), as observed from the peak ratio of peak 2 [104] with respect to other peaks. This indicates that annealing above 300 ^oC to obtain a single phase α-Fe_2O_3 nanoparticles is

adequate. The XRD pattern of the samples match those of the hexagonal structure (space group: R3c) of α-Fe_2O_3 with an ICSD card number of 081248 [1, 7, 13].

The broadness of diffraction peaks is influenced by the crystallite size and the internal strain. The Scherer's equation was used to estimate the crystallite size by averaging the sizes of peak [012], [104], [110] and [113]. The peak [104] was used to calculate the crystallite size.

$$D_{hkl} = \frac{K\lambda}{\beta cos\theta} \qquad 3.1$$

where D_{hkl} is the crystallite size, k is the Scherer coefficient (0.89), λ is the wavelength of the X-rays, and β is the full width at half maximum (FWHM) and θ is the diffraction angle. The crystallite sizes were 3.9 nm and 9.5 nm for the samples annealed at 300°C and 600°C respectively. Other researchers have, also reported the increase in crystallite size with increase in annealing temperature as observed in his work. Similarly, an increment of crystallite size for α-Fe_2O_3 nanoparticles from 18 to 54 nm was reported when annealing temperature increased from 300 °C and also providesto 500 °C [26]. An increment of the crystallite size for α-Fe_2O_3 from 34 to 44 nm was also reported when annealing temperature was increased from 500 °C to 700 °C [10]. When the particles are forming, they either collide or coalesce with one another to form a large particle observed from the enhanced diffraction peak. The process that occur depends upon the temperature and available energy; hence, the particle size increases with increasing temperature [27].

3.3.2. Transmission Electron Microscopy

The particle size and morphology were analyzed using TEM. Fig 3.2 shows the TEM images of α-Fe_2O_3 nanoparticles. Sample (a) shows amorphous structure as confirmed by XRD, sample (b) and (c) confirms the nanoscale dimension of the particles and shows the average diameter of 3 nm and 20 nm respectively. The images reveal that the particles have spherical morphologies. The particles size increases due to the increasing annealing temperature. The disparity between TEM and XRD is that XRD provides reliable statistical information and provides estimation of the particle size from the broadening of the RXD reflection by means of the Scherer formula. The TEM on the other hand, size distribution curve is limited to several hundreds of particles. The particle boundaries cannot always be seen precisely, due to lack of overlap of the particles [28].

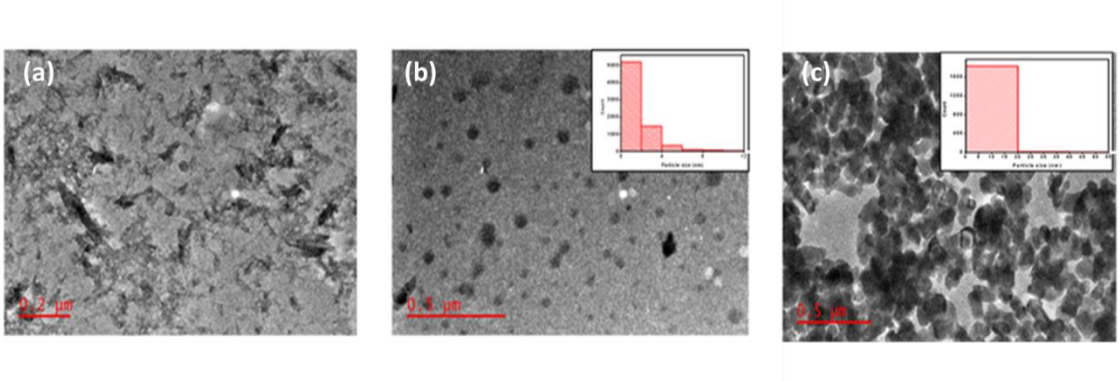

Figure 3. 2 TEM image of α-Fe_2O_3 nanoparticles (a) as-prepared and annealed at different temperatures (b) 300°C and (c) 600°C.

3.3.4. X-ray photoelectron spectroscopy (XPS)

In XPS, standard α-Fe_2O_3 has two Fe 2p peaks ($2p_{1/2}$ and $2p_{3/2}$), Fe $2P_{3/2}$ peak is narrower, stronger and has more area than Fe $2p_{1/2}$ because Fe $2p_{3/2}$ has a degeneracy of four states while Fe$2p_{1/2}$ has only two in spin-orbit (j-j) coupling [29]. Since the Fe 2P peaks have asymmetric shape for metals, multiple spitting was observed which are due to atoms containing unpaired electrons. In this instance there can be coupling between the unpaired electron in the core with unpaired outer shell electron when a core electron vacancy is formed. This phenomenon can create a number of final states, which will manifest in the photo electron spectrum [30].

Fig 3.3 and 3.4 show fitted XPS data of Fe 2p and O 1s orbitals. The Fe $2p_{3/2}$ and Fe $2p_{1/2}$ are fitted with two multiple peaks. The Fe 2p spectrum shows the presence of a satellite peak that confirms the presence of α-Fe_2O_3 [31]. The obtained binding energies of Fe $2P_{3/2}$ and Fe $2p_{1/2}$ for sample (a) are 724.2 eV and 711.1 eV respectively. The clearly distinguishable satellite peak is obtained at 718.9 eV (~ 8eV) and does not overlap with the Fe 2p3/2 or Fe 2p1/2. The high binding energy surface peak indicate that the relative intensity of the surface structure was large. The rest of the binding energies are listed in table 3.1. Similar binding energies have been reported in the literature [32, 33]. To determine the presence of oxide/hydroxyl species in the samples, an O 1s spectrum was measured. Due to primity of the binding energies (BE) of many surface and bulk species that have different chemical state, in the O 1s region, the BE peak at 530.1 eV can be assigned to oxygen atom in the iron oxide lattice, O1s (Fe-O), associated with a high electron density on ferric cation. The as grown samples are a hydroxide Fe-OH and is reduced to Fe-O by reduction in coordination of the molecules located at the surface after annealing at high temperatures. The rest

of the assigned peaks are shown in table 3.1. The XPS peak fit was used to fit the spectrum. We could not put the accuracy of the fit because of the satellite peaks, which came into play. The outline of the fitting procedure is as follows: (1) select the binding energy for background subtraction, (2) Select linear method for background subtraction, (3) Select Gaussian-Lorentzia ratio to determine peak shape, (4) Select asymmetry factory (FWHM) for the specific peaks and (5) Select best fitted curve for experimentally obtained Fe 2p and O ls.

Table 3.1 Peak position values of Fe 2p peaks and O 1s.

Peak positions (eV)	
Fe $2p_{1/2}$	Fe $2p_{3/2}$
724.2	711.1
724.2	710.8
723.8	710.7
O1s peak positions (eV)	
530.1	Fe - O
531.1	Fe - OH lattice
532.0	Fe - OH adsorbed
528.8	C – O
529.2	O - H

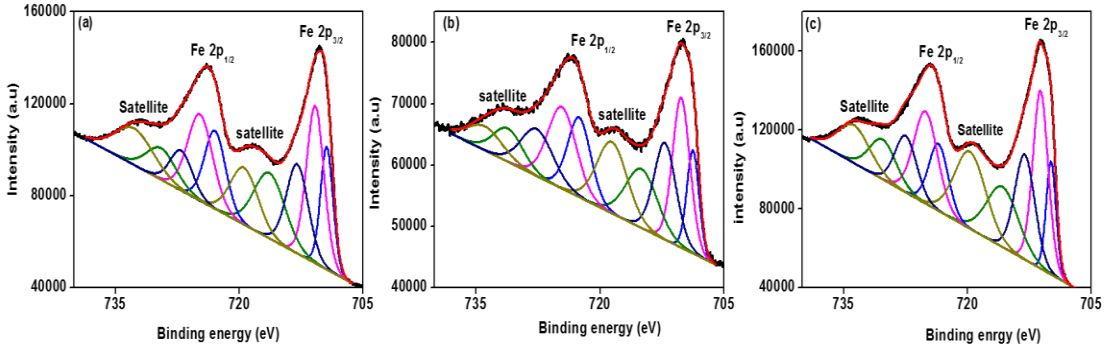

Figure 3. 3 XPS spectra of the Fe 2p of the powders (a) as prepared (b) annealed at 300° C and (c) annealed at 600°C.

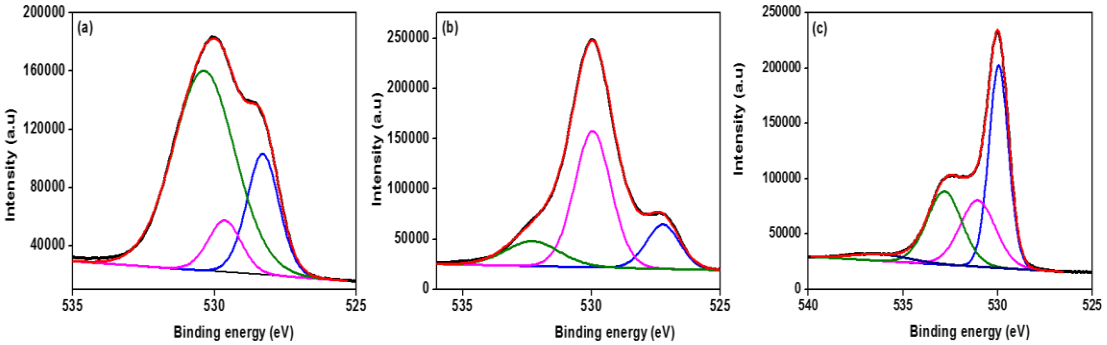

Figure 3. 4 XPS spectra of the O 1s of the powders (a) as prepared, (b) annealed at 300° C and (c) annealed at 600°C.

The formation of α-Fe_2O_3 nanoparticles was further confirmed by FTIR spectroscopy. Fig 3.5 shows FT-IR spectra of α-Fe_2O_3 samples annealed at different temperatures in the range of 350 – 4000 cm^{-1}, which identifies the chemical bonds as well as functional groups. It can be seen that, there was a significant broad band centered at 3394 cm^{-1} which was assigned to the O-H stretching inside hematite network structure. A hematite has ideally no bulk O-H group, these vibrations arise from non-stoichiometric hydroxyls and water entrapped in the hematite bulk during synthesis. The bands centered at 1531cm^{-1} and 1302 cm^{-1} may possibly be assigned to O-H bending modes. The band centered at 400 cm^{-1} is assigned to the A_{2u} mode, bands at 679 cm^{-1} and 486 cm^{-1} are both assigned to the Fe-OH mode [34, 35]. All the bonding peaks became sharper and stronger from as prepared to the powder annealed at 600 °C, which shows better crystallinity of the nanostructures

at high temperature. This phenomena of crystallinity is well confirmed in XRD spectra.

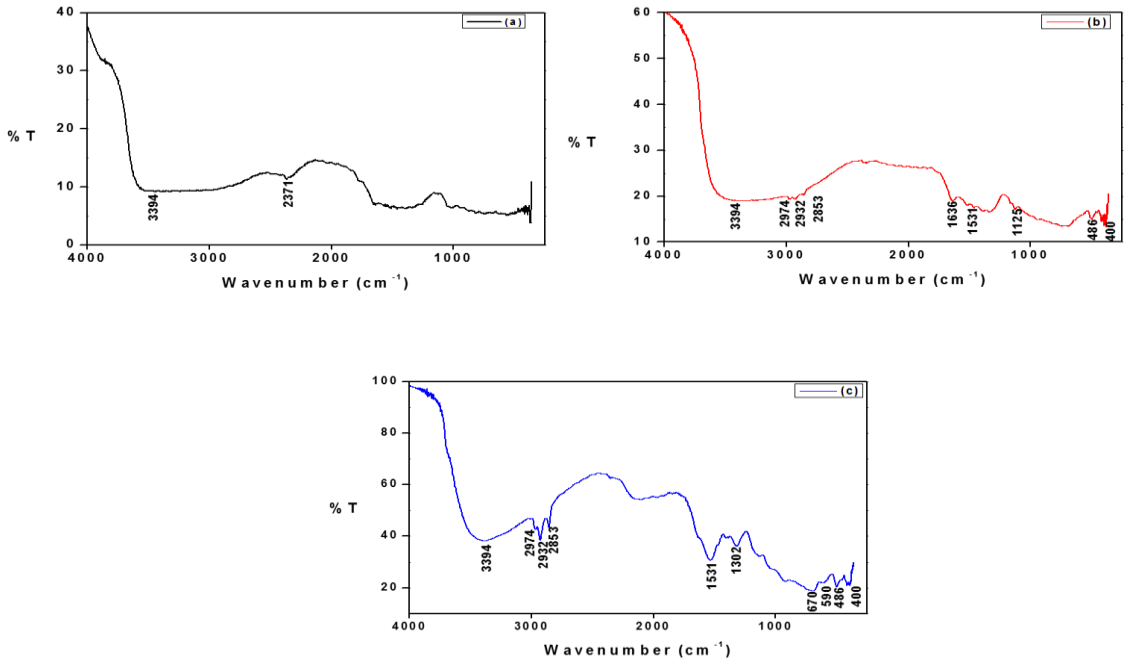

Figure 3. 5 FTIR spectrum of α-Fe_2O_3 samples at different temperatures (a) as prepared, (b) 300°C and (c) 600°C.

3.3.5. Diffuse reflectance

Fe oxides exhibit variety of colors, which result from different types of electronic transitions. As a rule, there is a strong absorption in the ultraviolet (UV) by colored Fe oxides and blue spectral region except in the red and infrared (IR) region, they strongly reflect. When the surface of the powdered materials is bombarded with a beam of light, only a small fraction is specularly reflected, the remainder penetrate into the mass and undergoes scattering. Some parts of the radiation ultimately leave the mass in all directions and constitute diffused reflectance. The diffuse reflectance has been proven to be useful to identify and characterize different Fe oxides [36].

The diffuse reflectance spectra of the three samples are shown in Fig 3.6, below. The reflectance was measured using the 1050 LAMBDA UV/Vis/NIR spectrophotometer equipped with integrating sphere, measuring from 200 nm to 800 nm. It is observed that from 300 nm to 510 nm the nanomaterials show a very low reflectance, which corresponds to high absorption. There is a rapid increase of reflectance at about 510 nm. In the UV region, two weak bands are observed at 240 nm and 286 nm which are attributed to ligand-to-metal charge transfer between the O 2p

orbital to the F^{3+} $2t_{2g}$ and $3e_g$ orbitals [37]. In the visible region between 400 nm and 700 nm, there exist three poorly defined bands at 420 nm, 530 nm and 620 nm. According to literature [38-40], the 620 nm band arises from the ligand field transition, 530 nm from electric pair transition and the 420 nm was assigned to the $^6A \rightarrow {}^4E$ transition. The region between 700 and 800 nm, with low absorption, shows very high reflectance. These bands shift to longer wavelength (red shift) as the temperature increases with increasing particle size. As the temperature increases from 300 °C to 600 °C the spectrum shows two band edges, this is due to the Laporte-forbidden transition and also the increases in the size of the particles.

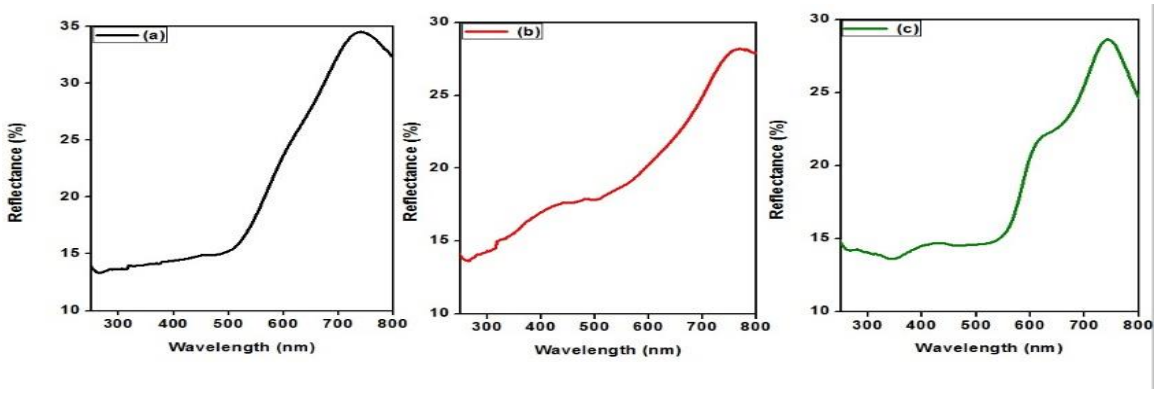

Figure 3. 6 Diffused reflectance spectra of α-Fe_2O_3 nanoparticles for (a) as prepared, (b) annealed at 300°C and (c) annealed at 600°C.

To estimate the band gap of the nanomaterials, the Kubelka-munk relation was used

$$F(R) = \frac{(1-R)2}{2R} = \frac{K}{S} \qquad 3.2$$

where R is the absolute reflectance of the sample, K is the molar absorption coefficient and S is the scattering coefficient. From the relation we can generate a plot of $(F(R)\ hv)^2$ vs hv which is shown in Fig 3.7 for the 3 samples. From the plot the band gap is estimated from the linear part of the plot. The observed band gap for (a), (b) and (c) are 2.06 eV, 1.69 eV and 1.98 eV respectively. The fluctuation of the band gap can be attributed to the innumerable surface states present in the system. The different possibilities for the fluctuation are defect states, cation/anion vacancies, and interstitials with energy located within the band gap. Also, it could be due to the surface related to

the adsorbed species where energy levels are within the band gap, which could be labile with size factor conditions [41].

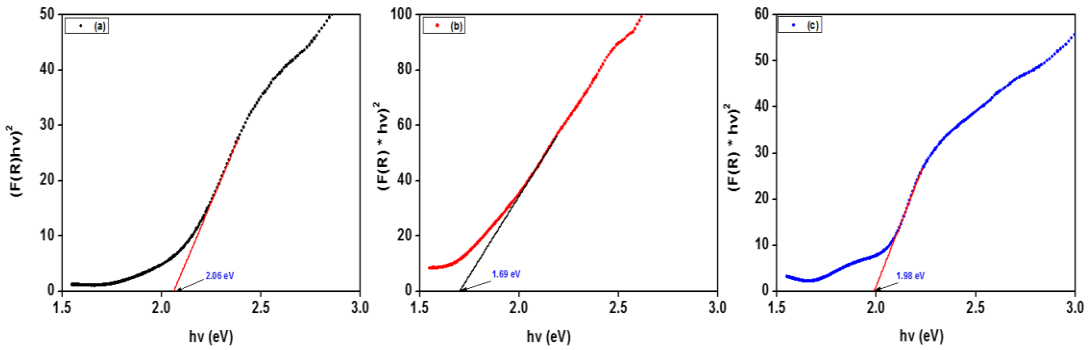

Figure 3. 7 Energy band gap extrapolation from the kubelka-Munk relation for (a) as prep (b) annealed at 300°C and (c) annealed at 600°C.

3.3.6. Photoluminescence properties

Due to the local forbidden d-d transition, resonant energy transfer between cations and efficient lattice and magnetic relaxation, bulk α-Fe_2O_3 does not show photoluminescence. However, due to quantum effect, α-Fe_2O_3 nanostructures exhibit photoluminescence resulting in delocalization and quantization of electronic state [7]. The photoluminescence property of α-Fe_2O_3 was measured after exciting the samples with different wavelengths using the xenon lamp. The excitation wavelength was from 200 nm to 360 nm in steps of 2 nm. The 3D acquisition (excitation vs Emission vs Intensity) was acquired. It is observed that the emission intensity increases with increasing excitation wavelength and then decreases after a certain wavelength.

Fig 3.8 (a -c) shows the 3D spectra and contour maps for the α-Fe_2O_3 samples prepared at different temperatures. The contour map of the 3D acquisition spectra is shown as well. Along with the contour maps are the scale bars, which indicate the luminescence intensity. According to the contour map, the maximum emission peak is observed at 388 nm for sample a, the maximum emission for sample b is centered about 425 nm. Fig 3.8c shows spectra with two emission peaks at 388 nm and 427 nm, with 427 nm peak being the most intense peak of the two. This is evident on the contour map.

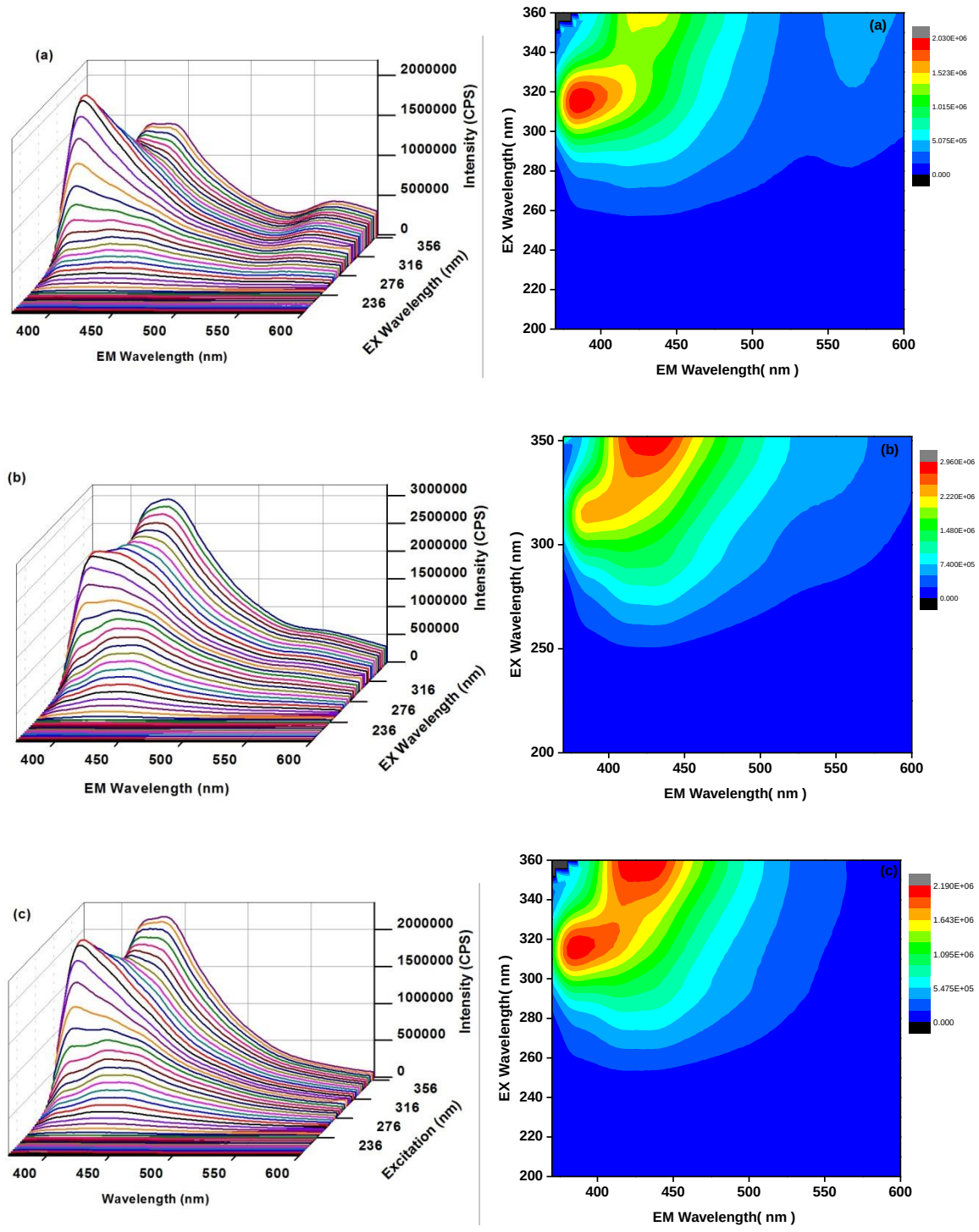

Figure 3. 8 Photoluminescence spectra showing the 3D and Contour images of (a) as prepared, (b) annealed at 300°C and (c) annealed at 600°C.

From the 3D spectra (Fig 3.8) an excitation wavelength of 336 nm was chosen for a line plot because that is where the nanoparticles show strong photoluminescence, as shown in Fig 3.9. At an excitation wavelength of 336 nm, the α-Fe_2O_3 nanoparticles show an intense emission band around 422 nm. Cherepy et al [42] observed an emission band at ~400 nm (excited at 300 nm) from a spindle shaped hematite nanostructures. Such emission above the band gap was intriguing because it was rarely detected. Because there was no measurable emission induced by the Fe^{3+} ligand field and exciton pair transition in the visible region, they attributed the band at ~400 nm to ligand-to-metal charge-transfer transition.

The decrease in particle size can be attributed to the origin of the luminescence of α-Fe_2O_3, which leads to the reduction in interaction. The emission intensity of the sample annealed at 300^{o}C (b) increases compared to the as prepared sample (a) and a decrease in intensity was measured as the annealing temperature was further increased to 600^{o}C (c). The enhancement of the intensity can be related to the size of the nanoparticles, as the size increase the photoluminescence increases. The broad emission peak was de-convoluted using a Gaussian fitting to understand their peak position and nature, shown in Fig 3.10. The emission peak at 350 nm is assigned to localized states in the band gap. The intense peaks at 404 nm and 435 nm are related to shallow defects emissions and mainly result from defects such as interstitials and oxygen vacancies. The broad peak at 475 nm is attributed to the recombination of electron-hole pair from the free or shallowly trapped exciton [43]. The broader peak at 576 nm is attributed to the radiative recombination of electron trapped at oxygen vacancy-related state near the conduction band edge with holes in deep Fe-related surface state [44].

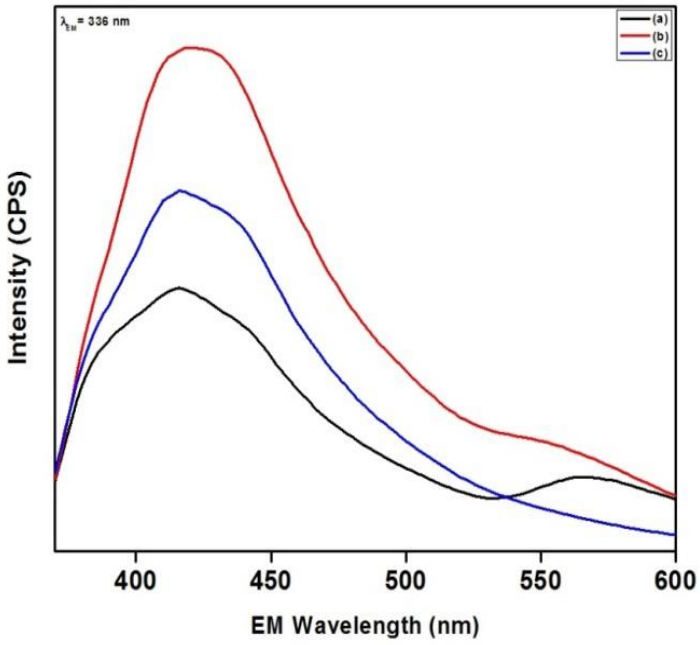

Figure 3. 9 ***Photoluminescence spectra of α-Fe_2O_3 nanoparticles of (a) as prepared, (b) annealed at 300°C and (c) annealed at 600°C excited at λ = 336 nm.***

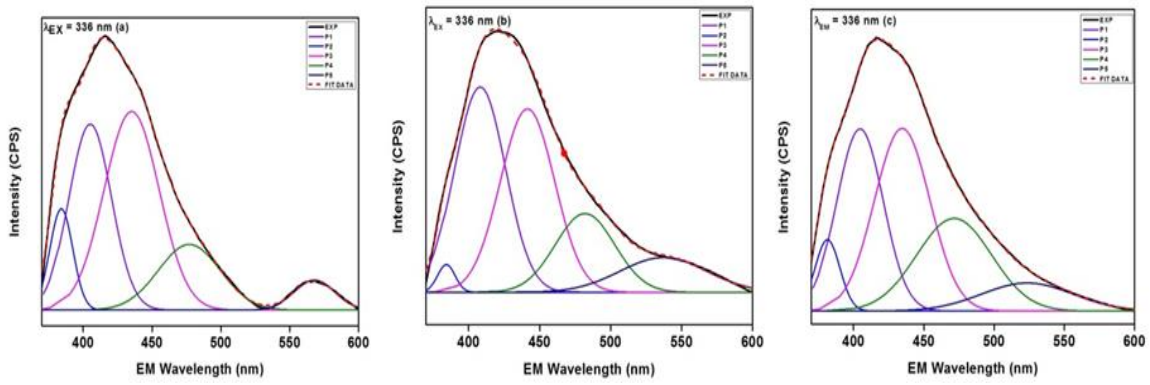

Figure 3. 10 Deconvolution photoluminescence emission spectra of α-Fe_2O_3 (a) as prepared, (b) annealed at 300°C and (c) annealed at 600°C, excited at 336 nm.

3.3.7. Thermoluminescence

Thermoluminescence (TL) was measured to approximate the activation energy necessary to detrap the electrons from the electron trapping centers of α-Fe_2O_3, and to evaluate the kinetics involved. The TL glow curves of α-Fe_2O_3 shown in Fig 3.11 were obtained by irradiating the sample with beta particles. To improve the glow curve signal, the sample was dosed up to 1315 Gy. With an increment of dose, a peak positioned at 69 °C prevailed, and second peak at 163°C appeared. The second peak may indicate that we have 2 prominent electron traps in our system. We observe a glow shift to higher temperatures, which indicates that the kinetics followed by the traps are neither of first nor second order. It has been reported that the system follows first order kinetics when there is no shift in temperature position upon exposure. For second order kinetics the shift is towards the lower temperature [45]. Three methods were used to approximate the activation energy.

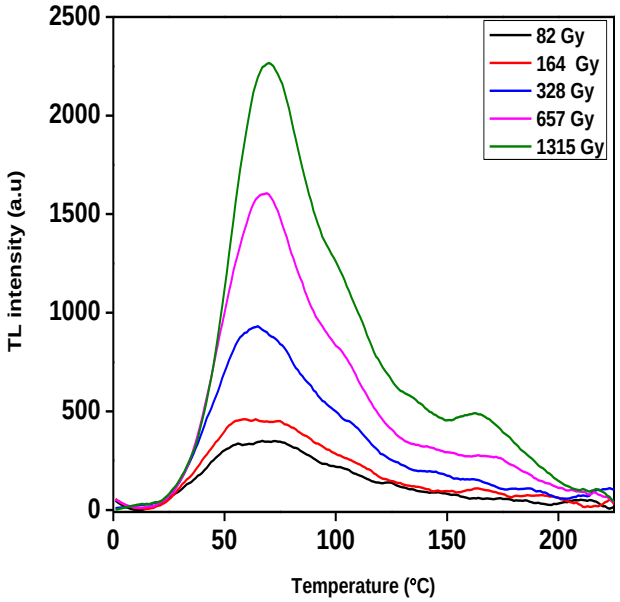

Figure 3. 11 Different glow curves acquired by exposing α-Fe_2O_3 to different doses of Beta particles.

The geometrical shape of a TL glow peak plays an important role in calculating trapping parameters. The first method used to approximate the activation energy of the first trapping centre

was initial rise (IR) method [46]. In IR method, the initial portion of the peak is taken under consideration as shown in Fig12 (a). In this method, the dependence of temperature is being neglected because of the amount of trapped electrons in the low initial tail of peak can be assumed to be constant. We obtained the activation energy E by plotting Ln(I) vs 1/*k*T (Fig 3.12(b)) for the initial part of the data. The energy was estimated to be 0.85 eV from the glow curve obtained by exposing the sample to 1315 Gy.

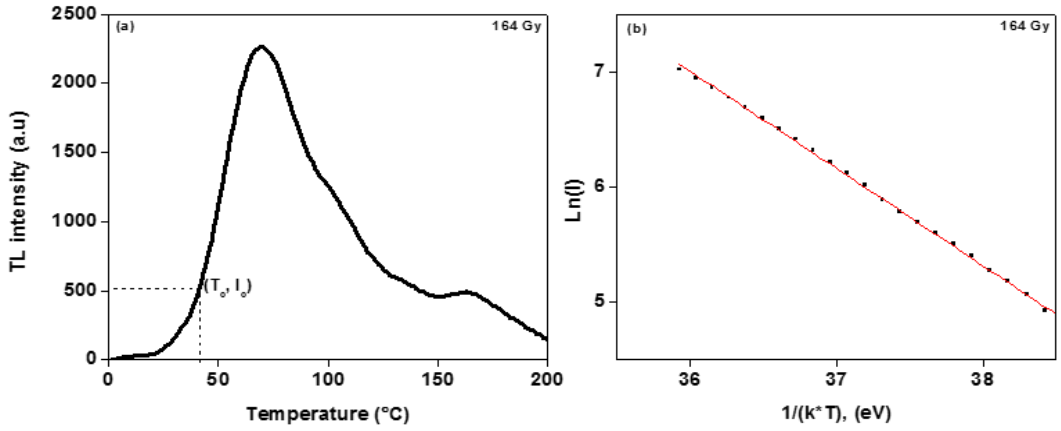

Figure 3. 12 (a) Glow curve showing cut off temperature region of the glow curve acquired from 164 Gy exposure, (b) the linear fit on the curve of Ln(I) vs 1/KT.

Chen's method was also used to estimate the activation energy. From the glow curve (Fig 3.13) three temperatures required for Chen's peak shape equation were estimated to:

T_1 = 49.7°C = 322 K, T_2 = 104.7°C = 377.7 K and T_M = 69.9°C = 342.9 K

The τ, δ, and ω ratios were estimated to 20.2, 34.8 and 55 respectively. The value of the geometric factor μ = $\frac{\delta}{\omega}$ was approximated to 0.63. The geometric factors full width at half maximum (FWHM) (ω), low temperature parameter (τ) or the upper temperature parameter (δ) are used to approximate the activation energy using Eq. 3.3. $\boldsymbol{A_\alpha}$ and $\boldsymbol{b_\alpha}$ are constants where α can either be ω, τ or δ. The activation energy was estimated to be 0.82 eV.

$$\mathbf{E}_\alpha = \boldsymbol{A}_\alpha \left(\frac{kT_m^2}{\alpha}\right) - 2\, \boldsymbol{b}_\alpha\, \mathbf{k}\mathbf{T}_m \qquad 3.3$$

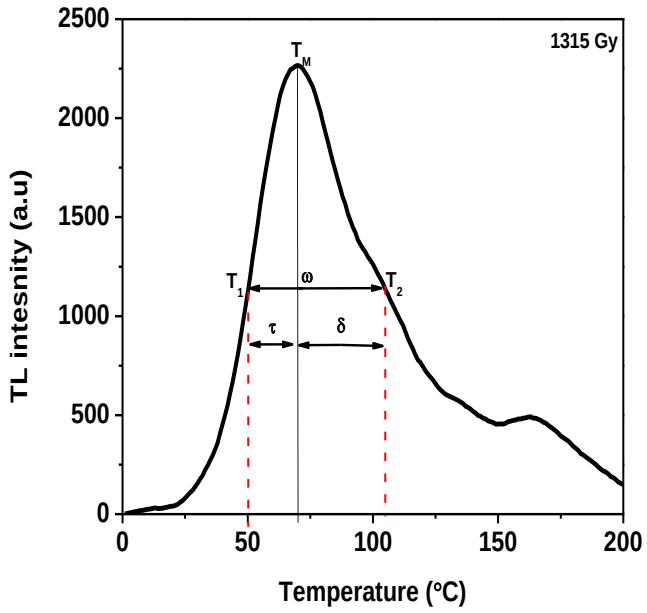

Figure 3. 13 ***Chen's peak shape ratios in the glow curve obtained with 1315 Gy exposure.***

The variable heating rate method used also to estimate the activation energy. In this method the glow curves were measured by varying the heating rate from 0.5, 1, 2, 3, 4, 5 °C.s^{-1} for the α-Fe_2O_3 sample exposed to 1315 Gy. In Fig 3.14a, as the heating rate increases, the glow peaks shift to higher temperatures and the height of the TL peak changes. The activation energy (E) was extrapolated from the linear fit of ln (T_M^2/β) vs $1/kT_M$ graph, as shown in figure14b, and found to be 0.74 eV. The averaged activation energy from the three methods is estimated to be 0.80 eV.

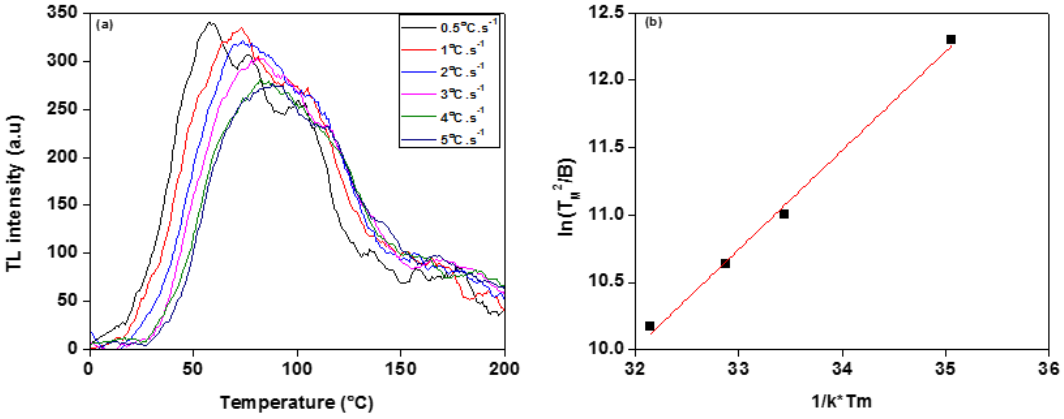

Figure 3. 14 (a) Glow curve for variable heating rates, (b) the slope for activation energy approximation.

3.4. Conclusion

α-Fe_2O_3 nanocrystals were successfully prepared by a simple sol-gel method. XRD confirmed no other phases other than α-Fe_2O_3. The crystallinity increased with increasing annealing temperature. The crystallite sizes were found to be smaller than those reported in literature. The FTIR confirmed the purity of α-Fe_2O_3 as no peaks belonging to other compounds were present. The band gap was found to be around 2eV with no particular trend from sample (a) to (c). The XPS shows that the samples are hydroxide Fe-OH which is then reduced to Fe-O when annealed. A 3D photoluminescence spectrum was acquired to obtain the maximum emission of the samples. The emission spectrum was then de-convoluted to understand their positions centered at 350 nm, 404 nm,435 nm, 475 nm and 576 nm. The 404 nm and 435 nm are found to be related to the shallow defect emission, 350 nm arises from the localized states in the band gap, the 475 nm arise from the recombination of electron-hole pair from free or shallowly trapped exciton and the 576 nm is attributed to radiative recombination of electron trapped at oxygen vacancy-related state near the conduction band edge with holes in deep Fe-related surface state. The averaged activation energy was approximated to be 0.8 eV.

References

[1] H. Gleiter, H. Hahn, and T. Schimmel, "Advances in nanomaterials," Beilstein J. Nanotechnol., vol. 4, no. 1, p. 805–806, 2013.

[2] M.A. Mahadik et al., 'Photocatalytic oxidation of Rhodamine B with ferric oxide thin films under solar illumination,' Materials Research Bulletin, Vol. 48, p. 4058–4065, 2013

[3] Jun Wang, W William B. White, and James H. Adair, ''Optical Properties of Hydrothermally Synthesized Hematite Particulate Pigments'', J. Am. Ceram. Soc., vol. 88, no. 12, p. 3449–3454, 2005

[4] Jose Torrent and Vidal Barron, 'Diffuse reflectance spectroscopy of iron oxides', Encyclopedia of Surface and Colloid Science, p. 1433-1446, 2002

[5] Mahadeo Mahadik, Sambhaji Shinde, Vijay Mohite, Sarita Kumbhar, Kesu Rajpure, Annasaheb Moholkar, Jin Kim, and Chandrakant Bhosale, 'Photoelectrocatalytic oxidation of Rhodamine B with sprayed α-Fe_2O_3 photocatalyst,' Mater. Express, Vol. 3, No. 3, p. 247-255, 2013

[6] S. C. K. G. S. B. A. H. Bagheri, "Generation of Hematite Nanoparticles via Sol-Gel Method," Res. J. Chem. Sci., vol. 3, no. 7, pp. 62–68, 2013.

[7] P. Shikha, B. S. Randhawa, and T. S. Kang, "Greener synthetic route for superparamagnetic and luminescent α-Fe_2O_3 nanoparticles in binary mixtures of ionic liquid and ethylene glycol," RSC Adv., vol. 5, no. 63, p. 51158–51168, 2015.

[8] I. M. Mirza, A. K. Sarfraz, and S. K. Hasanain, "Effect of Surfactant on Magnetic and Optical Properties of α-Fe_2O_3 Nanoparticles," Acta Phys. Pol. A., vol. 126, no. 6, p. 1280–1287, 2014.

[9] S. S. Shinde, R. A. Bansode, C. H. Bhosale, and K. Y. Rajpure, 'Physical properties of hematite α-Fe_2O_3 thin films: application to photoelectrochemical solar cells,' Journal of Semiconductors, Vol. 32, No. 1, p. 013001, 2011

[10] P. Mallick and B. N. Dash, "X-ray Diffraction and UV-Visible Characterizations of α-Fe_2O_3 Nanoparticles Annealed at Different Temperature," Nanosci. Nanotechnol., vol. 3, no. 5, p. 130–134, 2013.

[11] W. Wu, Z. Wu, T. Yu, C. Jiang, and W.-S. Kim, "Recent progress on magnetic iron oxide nanoparticles: synthesis, surface functional strategies and biomedical applications," Sci. Technol. Adv. Mater., vol. 16, no. 2, p. 23501, 2015.

[12] M. Mohammadikish, "Hydrothermal synthesis, characterization and optical properties of ellipsoid shape α-Fe_2O_3 nanocrystals," Ceram. Int., vol. 40, no. 1 part B, pp. 1351–1358, 2014.

[13] X. M. Liu, S. Y. Fu, H. M. Xiao, and C. J. Huang, "Preparation and characterization of shuttle-like α-Fe $_2O_3$ nanoparticles by supermolecular template," J. Solid State Chem., vol. 178, no. 9, p. 2798–2803, 2005.

[14] Farnaz Assa, Hoda Jafarizadeh-Malmiri, Hossein Ajamein, Navideh Anarjan, Hamideh Vaghari, Zahra Sayyar, and Aydin Berenjian, 'A biotechnological perspective on the application of iron oxide nanoparticles', Nano Research., Vol 9, no. 8, P. 2203–2225, 2016

[15] S. Akbar, S. K. Hasanain, N. Azmat, and M. Nadeem, "Synthesis of Fe_2O_3 nanoparticles by new Sol-Gel method and their structural and magnetic characterizations," Cond. Matter., p. 1–19, 2004.

[16] M. Srivastava, A. K. Ojha, S. Chaubey, J. Singh, P. K. Sharma, and A. C. Pandey, "Investigation on magnetic properties of α-Fe_2O_3 nanoparticles synthesized under surfactant-free condition by hydrothermal process," J. Alloys Compd., vol. 500, no. 2, p. 206–210, 2010.

[17] S.S. Shinde, C.H. Bhosale, K.Y. Rajpure, 'Studies on morphological and electrical properties of Al incorporated combusted iron oxide,' Journal of Alloys and Compounds, Vol. 509, p. 3943–3951, 2011

[18] S. S. Shinde, Sher Singh Meena, S. M. Yusuf, and K. Y. Rajpure, 'Mossbauer, Raman, and Magnetoresistance Study of Aluminum-Based Iron Oxide Thin Films,' J. Phys. Chem. C Vol. 115, p. 3731–3736, 2011.

[19] A. Mao, G. Y. Han, and J. H. Park, "Synthesis and photoelectrochemical cell properties of vertically grown α-Fe2O3 nanorod arrays on a gold nanorod substrate," J. Mater. Chem., vol. 20, no. 11, p. 2247, 2010.

[20] C. H. Kim, H. J. Chun, D. S. Kim, S. Y. Kim, J. Park, J. Y. Moon, and G. L. et Al, "Magnetic anisotropy of vertically aligned α-Fe2O3 nanowire array," Appl. Phys. Lett., vol. 89, no. 22, p. 22310301−22310303, 2006.

[21] Z. Zhang, M. F. Hossain, and T. Takahashi, "Self-assembled hematite (α-Fe_2O_3) nanotube arrays for photoelectrocatalytic degradation of azo dye under simulated solar light irradiation," Appl. Catal. B Environ., vol. 95, no. 3–4, pp. 423–429, 2010.

[22] M. V. Reddy, T. Yu, C. H. Sow, Z. X. Shen, C. T. Lim, G. V. Subba Rao, and B. V. R. Chowdari, "α-Fe_2O_3 Nanoflakes as an Anode Material for Li-Ion Batteries," Adv. Funct. Mater., vol. 17, no. 15, pp. 2792–2799, 2007.

[23] S. Bharathi, D. Nataraj, M. Seetha, D. Mangalaraj, N. Ponpandian, Y. Masuda, K. Senthil, and K. Yong, "Controlled growth of single-crystalline, nanostructured dendrites and snowflakes of α-Fe_2O_3: influence of the surfactant on the morphology and investigation of morphology dependent magnetic properties," CrystEngComm, vol. 12, no. 2, p. 373, 2010.

[24] S. Ni, S. Lin, Q. Pan, F. Yang, K. Huang, X. Wang, and D. He, "Synthesis of core-shell α-Fe_2O_3 hollow micro-spheres by a simple two-step process," J. Alloys Compd., vol. 478, no. 1–2, p. 876–879, 2009.

[25] M. Mohapatra and S. Anand, "Synthesis and applications of nano-structured iron oxides / hydroxides – a review," vol. 2, no. 8, p. 127–146, 2010.

[26] K. Raja, M. Mary Jaculine, M. Jose, S. Verma, A. A. M. Prince, K. Ilangovan, K. Sethusankar, and S. Jerome Das, "Sol–gel synthesis and characterization of α-Fe_2O_3 nanoparticles," *Superlattices Microstruct.*, vol. 86, p. 306–312, 2015.

[27] M.Z Igbal, S. Al and M.A Mirza, 'effect of particle size on the structural and transport properties of La0.67Ca0.33MnO3 nanoparticles', *CODEN JNSMAC*, vol. 48, no. 1&2, pp. 51-63, 2009

[28] Holger Borchert, Elena V. Shevchenko, Aymeric Robert, Ivo Mekis, Andreas Kornowski, Gerhard Grubel, and Horst Weller, 'Determination of Nanocrystal Sizes: A Comparison of TEM, SAXS, and XRD Studies of Highly Monodisperse CoPt3 Particles', *Langmuir*, Vol. 21, pp. 1931-1936, 2005.

[29] T. Yamashita and P. Hayes, "Analysis of XPS spectra of Fe^{2+} and Fe^{3+} ions in oxide materials," *Appl. Surf. Sci*., vol. 254, no. 8, p. 2441–2449, 2008.

[30] M. C. Biesinger, B. P. Payne, A. P. Grosvenor, L. W. M. Lau, A. R. Gerson, and R. S. C. Smart, "Resolving surface chemical states in XPS analysis of first row transition metals, oxides and hydroxides: Cr, Mn, Fe, Co and Ni," Appl. Surf. Sci., vol. 257, no. 7, p. 2717–2730, 2011.

[31] A. A. Tahir, K. G. Upul Wijayantha, S. Saremi-Yarahmadi, M. Maznar, and V. McKee, "Nanostructured α-Fe_2O_3 thin films for photoelectrochemical hydrogen generation," Chem. Mater., vol. 21, no. 16, p. 3763–3772, 2009.

[32] R. K. Sahu, D. Mukherjee, J. P. Tiwari, T. Mishra, S. K. Roy, and L. C. Pathak, "Influence of foreign Fe ions on wet chemical synthesis of Pt nanoparticle thin films at ambient temperature: in situversus direct addition," J. Mater. Chem., vol. 19, no. 37, p. 6810, 2009.

[33] L. Liu, X. Yang, C. Lv, A. Zhu, X. Zhu, S. Guo, C. Chen, and D. Yang, "Seaweed-Derived Route to Fe_2O_3 Hollow Nanoparticles/N-Doped Graphene Aerogels with High Lithium Ion Storage Performance," ACS Appl. Mater. Interfaces, vol. 8, no. 11, p. 7047–7053, 2016.

[34] J. L. Rendon, "IR Spectra of Powder Hematite: Effects of Particle Size and Shape," Clay Miner., vol. 16, no. 4, p. 375–382, 1981.

[35] H. S. Mansur, C. M. Sadahira, A. N. Souza, and A. A. P. Mansur, "FTIR spectroscopy characterization of poly (vinyl alcohol) hydrogel with different hydrolysis degree and chemically crosslinked with glutaraldehyde," Mater. Sci. Eng. C, vol. 28, no. 4, p. 539–548, 2008.

[36] J. Torrent and V. Barron, "Diffuse reflectance spectroscopy of iron oxides," Encycl. Surf. Colloid Sci., p. 1438–1446, 2002.

[37] J. Wang, W. B. White, and J. H. Adair, "Optical properties of hydrothermally synthesized hematite particulate pigments," J. Am. Ceram. Soc., vol. 88, no. 12, p. 3449–3454, 2005.

[38] G. Zhang, Y. Xu, D. Gao, and Y. Sun, "α -Fe_2O_3 nanoplates : PEG-600 assisted hydrothermal synthesis and formation mechanism," J. Alloys Compd., vol. 509, no. 3, p. 885–890, 2011.

[39] L. Lu, L. Li, X. Wang, and G. Li, "Understanding of the Finite Size Effects on Lattice Vibrations and Electronic Transitions of," p. 17151–17156, 2005.

[40] Y. Yamanoi, S. Nakashima, and M. Katsura, "Temperature dependence of refectance spectra and color values of hematite by in situ, high-temperature visible micro-spectroscopy," Am. Mineral., vol. 94, no. 1, p. 90–97, 2009.

[41] J. Dhanaraj, R. Jagannathan, T. R. N. Kutty, and Chung-Hsin Lu, 'Photoluminescence Characteristics of Y2O3:Eu3+ Nanophosphors Prepared Using Sol-Gel Thermolysis', J. Phys. Chem. B, 105, 11098-11105,2001

[42] D. a. Wheeler, G. Wang, Y. Ling, Y. Li, and J. Z. Zhang, "Nanostructured hematite: synthesis, characterization, charge carrier dynamics, and photoelectrochemical properties," Energy Environ. Sci., vol. 5, no. 5, p. 6682, 2012.

[43] M.A. Mahadik, S.S. Shinde, K.Y. Rajpure, C.H. Bhosale, 'Photocatalytic oxidation of Rhodamine B with ferric oxide thin films under solar illumination', *Materials Research Bulletin* vol. 48, pp 4058–4065, 2013

[44] A.V. Dijken, E.A. Meulenkamp, D. Vanmaekelbergh, A. Meijerink, 'Identification of the transition responsible for the visible emission in ZnO using quantum size effects', Juornal of louminescence, vol. 90,pp. 123–128, 2000M

[45] G Debelo, F B Dejene and Kittessa Roro, 'Thermoluminescence and photoluminescence study of KY_3F_{10}:Ho^{3+} commercial phosphor powder', Physica Scripta, vol. 91, p. 065701, (2016)

[46] Mahua Karmakar, On the Initial Rise Method for Kinetic Analysis in Thermally Stimulated Luminescence, Indian Journal of Science and Technology, vol 5, no. 11, 2012

Chapter4: Effect of Ho^{3+} doping on Structural and optical properties of α-Fe_2O_3 nanoparticles

4.1. Introduction

Intense scientific research for many years has been performed on iron oxide nanoparticles. Eight iron oxides are known and among them hematite (α-Fe_2O_3), magnetite (Fe_3O_4) and maghemite (γ-Fe_2O_3) are very promising and popular candidates due to their polymorphism involving temperature-induced phase transition [1]. α-Fe_2O_3 is the most stable iron oxide and n type semiconductor in ambient conditions [2]. α-Fe_2O_3 is an n-type semiconductor with a band gap of 2.3 eV, where the conduction band is composed of empty d- orbitals of Fe^{3+} and the valence band consist of occupied 3d crystal field orbitals of Fe^{3+} with some admixture from the O 2p non-bonding orbitals [3].

α-Fe_2O_3 particles are non-toxic, cost effective and are therefore used in many applications, such as drug delivery, bio-sensing, magnetic separation, magnetic resonance imaging and as contrast reagent. The iron oxide nanoparticles are usually doped with rare earth (RE) ions to enhance their properties for these applications. Rare-earth (Ln^{3+}) ions are known to have exceptionally large magnetic moment as well as luminescence properties [4]. Ln^{3+} is endowed with unique optical properties, which are attributed to abundant energy levels of 4f configuration. It can give out desired emissions through various energy transfer pathways because it possesses intermediate energy levels [5].

The structural incorporation of foreign cations, particularly facile for trivalent cations having similar ionic radius is another way of modifying substantially hematite properties. Particle shape may be altered by guest cations, as occurs with Al cations that cause a peanut-like shape, or induce change in optical properties, as observed for La-substituted micro-hematite [6]. Bhuiyan et.al have managed to incorporate lanthanum into hematite nanoparticles. The incorporation was evident by studying XRD, which showed the existence of $Fe_{2-x}La_xO_3$ by a shift in diffraction peak to lower angle [7].

Among trivalent RE ions, Ho^{3+} has been chosen as optically active center because it exhibits fluorescence in the visible and near infrared region [8]. Doping of hematite with rare-earth elements is however challenging, due to the different size of Fe^{3+} and rare-earth trivalent ions [6].

In this chapter, we investigate the alteration of both the structure and optical properties through doping of α-Fe_2O_3 with a range of holmium ion concentration by a simple sol-gel method.

4.2. Experimental

Un-doped and Ho^{3+} doped nanoparticles of α-Fe_2O_3 were prepared and different concentrations of Ho^{3+} were incorporated. Sol-gel method reported elsewhere [9] was used to prepare the material with some modifications. All the reagents were of analytical grade, and were used as received without further purification. Fe $(NO_3)_3 \cdot 9H_2O$ was used as the starting material. Different concentrations of Ho^{3+} 0 mol%, 0.1 mol%, 0.3 mol%, 0.6 mol% and 0.9 mol% were added in different beakers, and the mixtures were separately dissolved in absolute ethanol. The resulting liquid solution was continuously stirred at room temperature for 1 hour. The polyvinyl alcohol solution, 0.5 M was added into the stirred solution drop wise. The solution was then dried in an oven at absolute ethanol boiling point of 100°C for 1 hour. The obtained amorphous powder was then annealed in a furnace at 600°C to obtain α-Fe_2O_3:xHo^{3+} phosphor where x corresponds to 0 mol%, 0.1 mol%, 0.3 mol%, 0.6 mol% and 0.9 mol%. The powders were characterized by X-ray Diffraction (XRD), Transmission Electron Microscopy (TEM), Ultraviolet-visible Spectroscopy (UV-Vis, Photoluminescence Spectroscopy (PL) and Energy Dispersion Spectroscopy (EDS).

4.3. Characterization

4.3.1. XRD

The phase formation of un-doped and Ho^{3+} doped α-Fe_2O_3 nanoparticles at different concentration is shown in Fig. 4.1. The formation was confirmed using a Powder X-ray diffraction from Rigaku SmartLab, equipped with Cu Kα radiation of λ = 1.5405 Å. The XRD was operated at 40 kV and 200 mA. The observed diffraction patterns from both un-doped and doped α-Fe_2O_3:Ho^{3+} show only diffraction peaks corresponding to hexagonal structure of α-Fe_2O_3 (JCPDS card # 86-0550).

No diffraction peaks related to Ho_2O_3 were observed, indicating that Ho^{3+} ions have been incorporated into the Fe_2O_3 crystal lattice. The peak (116) at 54.10° was used to calculate the crystallite size using Scherer formula. The crystallite sizes were found to be 0.97, 0.73, 0.65, 0.44 and 0.42 nm for (a), (b), (c), (d) and (e) respectively. The size was observed to be decreasing with increasing Ho^{3+} concentration, due to an increase in the amount of grain boundaries.

As the Ho^{3+} ions were introduced into α-Fe_2O_3, the (116) peak was found to be shifted to lower 2θ angle and broadens due to large ionic radius of Ho^{3+} (1.76Å) than that of Fe^{3+} (0.69 Å). The shift of the peak is shown as the insert in Fig4.1. The lattice mismatch, distortion and crystallite strain has been reported to be the cause of the peak shifts and broadening [10]. The FWHM was found to be increasing with increasing concentration as the size of the crystal decreases. This observation also indicates that the nanoparticles lose crystallinity as the concentration of the dopant increases.

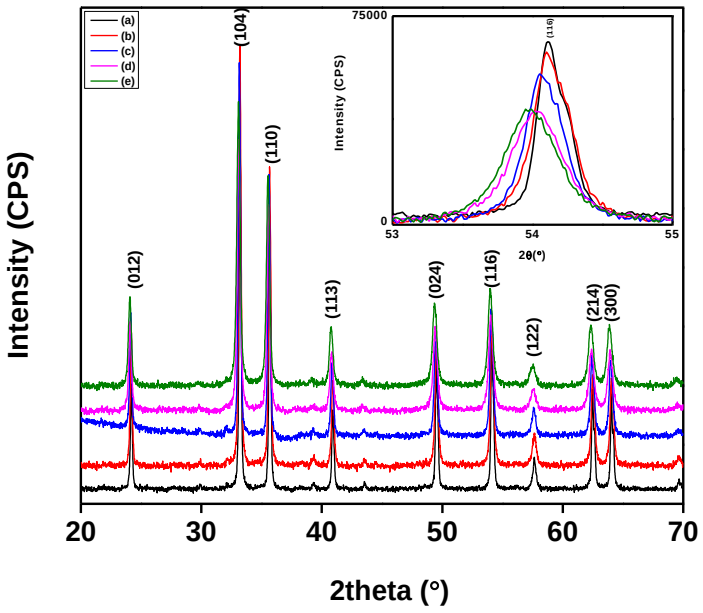

Figure 4. 1 XRD pattern of α-Fe_2O_3 and α-Fe_2O_3:Ho^{3+} nanoparticles at different doping concentration (a) 0 mol%, (b) 0.1 mol%, (c) 0.3 mol%, (d) 0.6 mol% and (e) 0.9 mol% annealed at 600°C. The insert is the magnified region of (116) peak.

4.3.2. TEM and Energy dispersive spectroscopy

The TEM image (Fig 4.2(a)) shows that the particles are spherical in shape and the size was approximated to 20 nm. There was no difference in terms of the morphology of all the samples, hence only the as prepared sample TEM image was shown. The EDS patterns are shown in Fig 4.2 (b-f). The EDS is a technique that is important in identifying the elemental signature of materials [11]. Fig 2 (b), (c), and (d) show the existence of Fe and O only, whereas, Fig 4.2 (e) and (f) shows the existence of Fe, O and Ho. The EDS suggest that the holmium content increases with an increase in the dopant concentration. The accompanying elemental quantification reveals that the intensity of Ho^{3+} peak increases from 1.4 to 2.7 wt % for the samples in figure 4.2 (e) and (f), respectively. This phenomenon has been observed when ZnO was doped with Ho^{3+} [12].

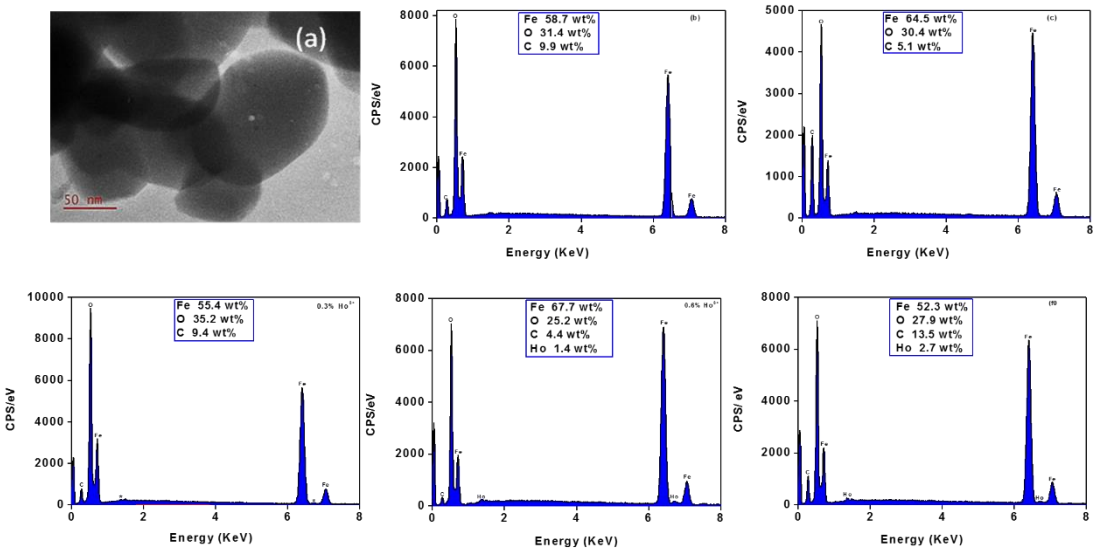

Figure 4. 2 TEM image (a) for 0 mol% and the survey scan for elemental analysis EDS for (b) 0 mol%, (c) 0.1 mol%, (d) 0.3 mol%, (e) 0.6 mol% and (f) 0.9 mol%.

4.3.3. UV-Vis

Fe oxides exhibit a variety of colors, which results from different types of electronic transitions. Colored Fe oxides are mostly reported to strongly absorb in the ultraviolet (UV) region and in the blue spectral region, and strongly reflecting in the red and infrared (IR) regions [13]. The reflectance spectra of α-Fe_2O_3:Ho^{3+} was measured at room temperature by a 1050 UV/Vs/NIR spectrophotometer, as shown in Fig 4.3.The spectrum is characterized by a nearly constant

reflectivity from 350 nm to 550 nm, a shoulder near 620 nm and a reflectivity maximum near 750 nm. The nanoparticles show a very low reflectance from 350 nm to 550nm. A rapid increase of reflectance occurs at about 560 nm. The slope of the curve depends on the particle size and shape involved and it shift to a lower wavelengths indicating a possible increase in the band gap. A wide absorption band around 660 nm in the red range is believed to arise from spin-forbidden ligand field transition, most likely $^6A_1 \rightarrow {}^4T_2$ [14].

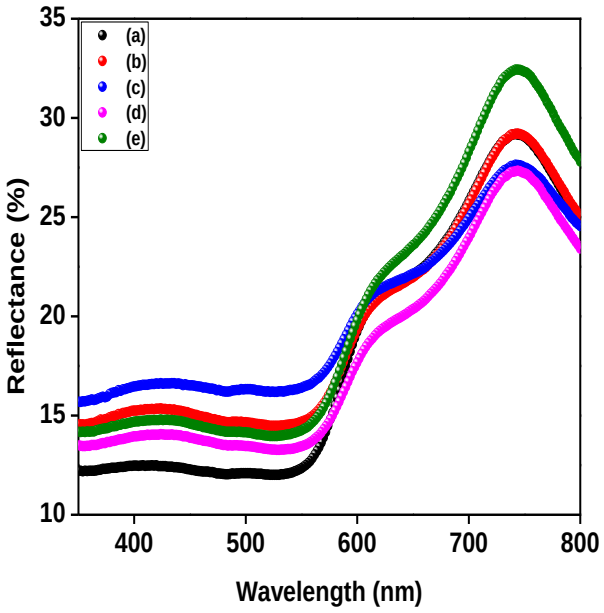

Figure 4. 3 Diffused reflectance spectrum of α-Fe_2O_3 and α-Fe_2O_3:Ho^{3+} nanoparticles at different Ho^{3+} doping concentration (a) 0 mol%, (b) 0.1 mol%, (c) 0.3 mol%, (d) 0.6 mol% and (e) 0.9 mol% annealed at 600°C.

For the band gap estimation a plot of hv v/s [$F(R_\infty)$ hv] is plotted from eq.3.2. The straight-line portion of the curve, when extrapolated to zero, gives the optical band gap E_g, as shown in Fig 4.4 a –e. The results show band gap decreases from 2.04 eV, 1.98 eV and 1.94 eV with an increase in Ho content from (a) to (c), and then increases to 1.97 eV and 2.0 eV as the Ho content increases further to (d) and (e), respectively. Since every particle is made up of only a very small number of atoms, the number of overlapping of orbitals or energy level decreases and the width of the band get narrower, thereby increasing the band gap. The reported band gap of α-Fe_2O_3 is about 2.2 eV [15]. The change in band gap with respect to size of the particle could be due to bulk defect, which

induces delocalization of molecular orbitals in the conduction band edge. It then creates shallow deep traps in electronic energy, in turn causing the red shift of the reflectance spectra. The traps shift to the higher energy when the crystallite size decreases below its size at the band gap minimum, which then results in blue shifting of the spectrum thereby increasing the band gap [16]. The band tailing becomes broader due to the slight doping and finally reaches and merges with the bottom of the conduction band causing sudden decreases of the optical band gap [17].

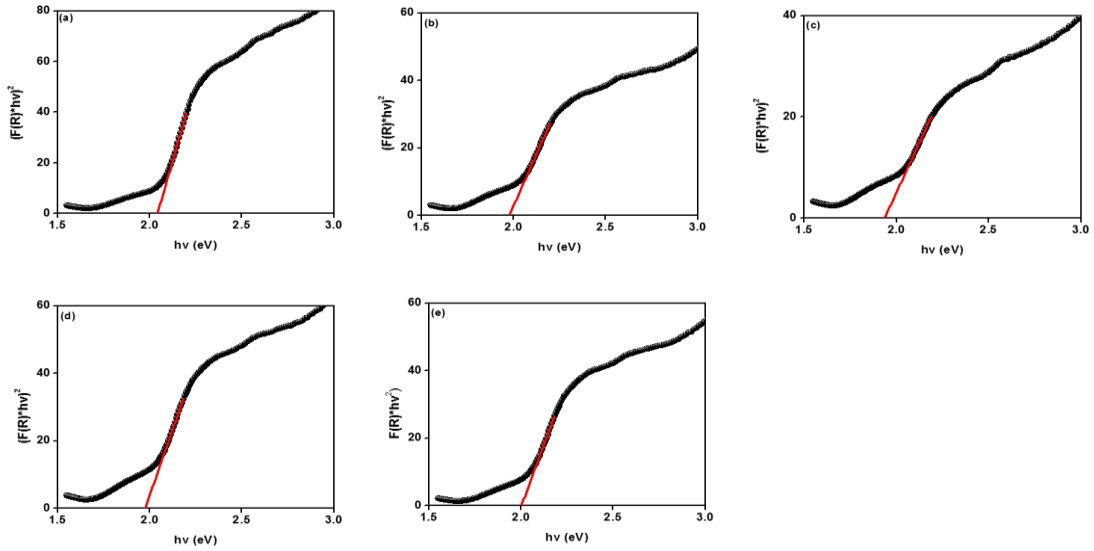

Figure 4. 4 KM band gap determination of α-Fe_2O_3 and α-Fe_2O_3:Ho^{3+} nanoparticles at different doping concentration (a) 0 mol%, (b) 0.1 mol%, (c) 0.3 mol%, (d) 0.6 mol% and (e) 0.9 mol% annealed at 600°C.

4.3.4. Photoluminescence

The room temperature down-conversion PL emission and excitation spectra of un-doped and doped α-Fe_2O_3 nanophosphors with different Ho^{3+} concentrations are shown in Fig 4.5. The spectra were measured with excitation radiation from a xenon lamp at the wavelength of 350 nm at room temperature, which corresponds to the best excitation wavelength. A blue emission in the visible region was observed for α-Fe_2O_3:Ho^{3+}, which is centered at 410 nm and 430 nm. It has been reported that the visible luminescence, related to deep level emissions, mainly results from the α-Fe_2O_3 defects such as interstitials and oxygen vacancies [18]. The emission intensity increases with an increase in Ho^{3+} doping concentration from (a) to (b); thereafter from (c) to (e) it shows quenching phenomena in PL intensity in no particular order. From the PLE spectrum, a strong

absorption was observed in the range 200 nm – 250 nm with (e) being the one with strongest absorption caused by electronic transition in the host matrix. The spectra are characterized by one sharp and one broad absorption band presented from UV to the visible spectrum region (200 nm – 450 nm). The band at 229 is attributed to the host-lattice absorption and the broad band at 377 nm correspond to 4f – 5d absorption oh Ho^{3+} ions [19].

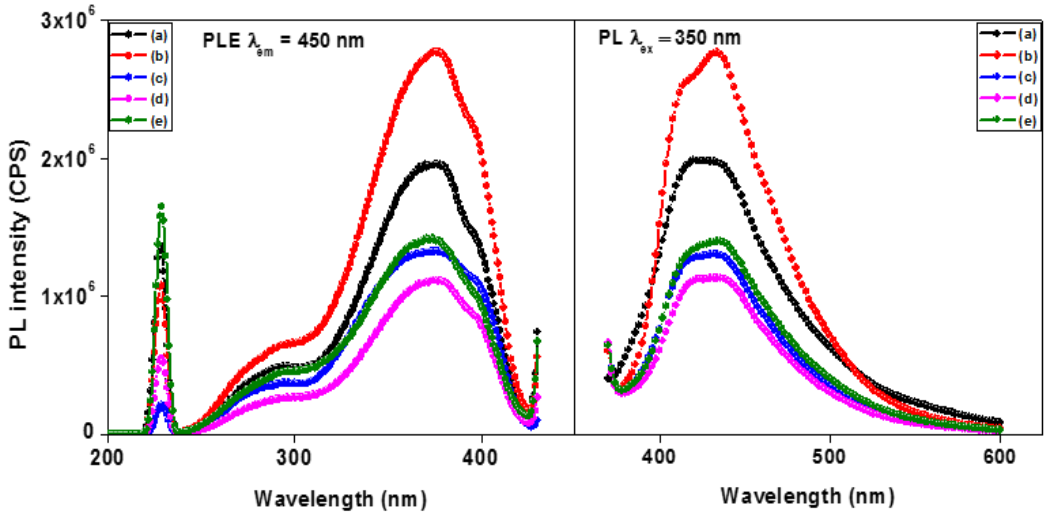

Figure 4. 5 ***Room temperature PL excitation and emission spectra of α-Fe_2O_3:Ho^{3+} at concentration (a) 0 mol%, (b) 0.1 mol%, (c) 0.3 mol%, (d) 0.6 mol% and (e) 0.9 mol%.***

4.4. Conclusion

Ho^{3+} ions were successfully incorporated into the α-Fe_2O_3 host material by a sol-gel method and accompanying effects were investigated. The XRD spectra show a decrease in average crystallite size from 0.97 nm to 0.42 nm with an increase in Ho^{3+} doping, due to increased grain boundaries. The amount of Ho^{3+} was quantified using EDS, which shows an increase in holmium quantity as the Ho^{3+} concentration increases. The diffuse reflectance spectra displayed a peak around 750 nm, which decreased from (a) to (d) and rapidly increase at (e). Due to the nature and strength of the crystalline potential by addition of the Ho^{3+} ions, the band gap decreased from 2.04 eV, 1.98 eV, and 1.94 eV for (a), (b) to (c) and increased from 1.97 eV to 2.00 for (d) to (e), respectively. The results from Photoluminescence shows that there is an enhancement in luminescence properties from (a) to (b), and thereafter quenching from (c) to (e).

References

[1] W. Wu, Z. Wu, T. Yu, C. Jiang, and W.-S. Kim, "Recent progress on magnetic iron oxide nanoparticles: synthesis, surface functional strategies and biomedical applications," *Sci. Technol. Adv. Mater.*, vol. 16, no. 2, pp. 23501, 2015.

[2] W. Wu, X. Xiao, S. Zhang, J. Zhou, L. Fan, F. Ren, and C. Jiang, "Large-scale and controlled synthesis of iron oxide magnetic short nanotubes: Shape evolution, growth mechanism, and magnetic properties," *J. Phys. Chem. C*, vol. 114, no. 39, pp. 16092–16103, 2010.

[3] Z. Zhang, C. Boxall, G. H. Kelsall, T. D. Waite, S. S. Dukhin, and M. Breuer, "Photoelectrophoresis of colloidal iron oxides. I: Hematite (α-Fe2O3). Discussion," *Colloids Surf. A. Physicochem. Eng. Asp.*, vol. 73, pp. 145–163, 1993.

[4] M. Bloemen, S. Vandendriessche, V. Goovaerts, W. Brullot, M. Vanbel, S. Carron, N. Geukens, T. Parac-Vogt, and T. Verbiest, "Synthesis and characterization of holmium-doped iron oxide nanoparticles," *Materials (Basel).*, vol. 7, no. 2, pp. 1155–1164, 2014.

[5] H. Dong, L. D. Sun, and C. H. Yan, "Energy transfer in lanthanide upconversion studies for extended optical applications," *Chem Soc Rev*, vol. 44, no. 6, pp. 1608–1634, 2015.

[6] Francesca Stefania Freyria, Gabriele Barrera, Paola Tiberto, Elena Belluso, Davide Levy, Guido Saracco, Paolo Allia, Edoardo Garrone, Barbara Bonelli, 'Eu-doped α-Fe2O3 nanoparticles with modified magnetic properties Francesca', *Journal of Solid State Chemistry, vol.* 201, pp. 302–311, 2013.

[7] T.I. Bhuiyan, M. Nakanishi, Y. Kusano, T. Fujii, J. Takada, Y. Ikeda, 'Synthesis, morphology and color tone properties of the lanthanum substituted hematite', *Mater. Lett,* vol. 61, pp. 3774–3777, 2007.

[8] S. Babu and Y. C. Ratnakaram, "Emission characteristics of holmium ions in fluoro-phosphate glasses for photonic applications," *DAE Solid State Physics Symposium*, vol. 1731, p. 70001, 2016.

[9] M. Farahmandjou and F. Soflaee, "Low Temperature Synthesis of α-Fe2O3 Nano-rods Using Simple Chemical Route," *Journal of NanoStructures*, vol. 4, no. 4. pp. 413–418, 2014.

[10] E. J. Mittemeijer and U. Welzel, "The 'state of the art' of the diffraction analysis of crystallite size and lattice strain," *Zeitschrift fur Krist.*, vol. 223, no. 9, pp. 552–560, 2008.

[11] B. Heffner, 'Energy dispersive spectroscopy on the SEM: a primer', Characterization facility, University of Minnesota – Twin Cities.

[12] G. M. Rai, M. A. Iqbal, Y. Xu, I. G. Will, and W. Zhang, "Doping on Structural, Microstructure and Magnetic Properties of ZnO Bulk and Thin Film Systems," *Chinese J. Chem. Phys.*, vol. 24, no. 3, pp. 353–357, 2011.

[13] J. Torrent and V. Barron, "Diffuse reflectance spectroscopy of iron oxides," *Encycl. Surf. Colloid Sci.*, pp. 1438–1446, 2002.

[14] L. Chen, X. Yang, J. Chen, J. Liu, H. Wu, H. Zhan, C. Liang, and M. Wu, "Continuous shape- and spectroscopy-tuning of hematite nanocrystals," *Inorg. Chem.*, vol. 49, no. 18, pp. 8411–8420, 2010.

[15] M. Mohammadikish, "Hydrothermal synthesis, characterization and optical properties of ellipsoid shape α-Fe_2O_3 nanocrystals," *Ceram. Int.*, vol. 40, no. 1 PART B, pp. 1351–1358, 2014.

[16] H. Lin, C.P. Huang, W.Li ,C.Ni, S. Ismat Shah , Yao-Hsuan Tseng , 'Size dependency of nanocrystalline TiO2 on its optical property and photocatalytic reactivity exemplified by 2-chlorophenol,' Applied Catalysis B: Environmental, Vol. 68, pp. 1–11, 2006.

[17] "Band gap narrowing of cadmium oxide powder by rare earth praseodymium doping," vol. 3, no. 1, pp. 47–50, 2017.

[18] M. A. Marzouk, S. M. Abo-naf, H. A. Zayed, and N. S. Hassan, "photoluminescence and semiconducting behavior of Fe, Co , Ni and Cu implanted in heavy metal oxide glasses," *J. Mater. Res. Technol.*, vol. 5, no. 3, pp. 1–8, 2015.

[19] Q. Wu, X. Wang, Z. Zhao, C. Wang, Y. Li, A. Mao, and Y. Wang, “Synthesis and luminescence characteristics of devices and fi eld emission displays,” *J. Mater. Chem. C Mater. Opt. Electron. devices*, vol. 2, pp. 7731–7738, 2014.

Chapter5: Structural and magnetic properties of Ho^{3+} and Yb^{3+} co-doped α-Fe_2O_3

5.1. Introduction

Due to strong influence on physical and chemical properties, magnetic nanomaterials have been in the trajectory for scientists [1]. Among these materials, rare-earth (RE) doped nanomaterials are widely investigated due to excellent luminescence characteristics arising from 4f – 4f transitions, giving rise to long luminescence lifetime and low absorption, which have clear advantages in applications of data storage devices, electrodes, magnetic fluids and bio-medicines [2]. RE ions have been extensively employed as activators for various phosphors. Phosphors are efficient luminescence material [3]. Fe_2O_3 is one of the simplest oxides on first impression, which usually exists in nature in two polymorphs: cubic γ-Fe_2O_3 and rhombohedral α-Fe_2O_3 (hematite) [4]. Hematite is the most stable iron oxide with a high resistance to corrosion, low cost, and it is also biocompatible, environmentally friendly and non-toxic. Hematite is an n-type semiconductor with a band gap of about 2.1 eV. It crystallize in the rhombohedral system space group R-3c [5]. Since hematite is stable at high temperature, it is a suitable host for the rare-earth ions [6].

Hematite is paramagnetic above Curie temperature (T_C) of 956 K. At room temperature is weakly ferromagnetic and undergoes a phase change at 260 K (Morin temperature, T_M) to antiferromagnetic state. Hematite magnetic behavior depends of the crystallinity and particle size. The T_M decreases as the particles size decreases and tend to vanish for particles smaller than 8-20 nm [7]. Ferromagnetism in hematite arise when an atom has a net magnetic moment due to unpaired electrons. When placed in a magnetic field, the magnetic moments of the domain align along the direction of the applied magnetic field forming a large net magnetic moment [8]. As traditional pigment being used in many applications, the optical properties of hematite have been studied extensively. One of the striking optical properties of hematite is its color, which was known for years but not studied in detail until the work by Kerker et al [9]. There is still a continuous research interest in mixed lanthanide oxide nanoparticle due to the magnetic and fluorescence properties, which are useful for many applications [10].

5.2. Methods

All the chemical reagents that we used were of analytical grade and were used as received without further purification. In this chapter sol-gel, method was followed to synthesize the Ho^{3+}:Yb^{3+} co-doped α-Fe_2O_3. $FeN_3O_9 \cdot 9H_2O$, Ho $(NO_3)_3 \cdot 5H_2O$, and Yb $(NO_3)_3 \cdot 5H_2O$ were used as the solid starting materials and were dissolved in absolute ethanol. The solution was stirred for 1 hour at room temperature. The Ho $(NO_3)_3 \cdot 5H_2O$, and Yb $(NO_3)_3 \cdot 5H_2O$ were added at different molar concentration, 0.1 mol% Ho with 0.75 mol% Yb, 0.9 mol% Yb and 1.05 mol% Yb. A solution of PVA was prepared and transferred to the solution with continuous stirring. The solution was then dried at 100°C. The obtained powder was ground into fine powders that were annealed at 600°C. The obtained powders were characterized with an X-Ray diffractometer (Rigaku SmartLab) to confirm the phase formation and the crystallinity of the samples. The diffused reflectance measurements were done to extract the absorption characteristics using the Lambda 1050 UV/Vis/NIR spectrophotometer. The X-ray photoelectron spectroscopy (XPS) was used to investigate the chemical state of the materials, and the Vibrating sample magnetometer was used to evaluate the magnetic properties of the nanoparticles.

5.3. Results and Discussion

5.3.1. XRD

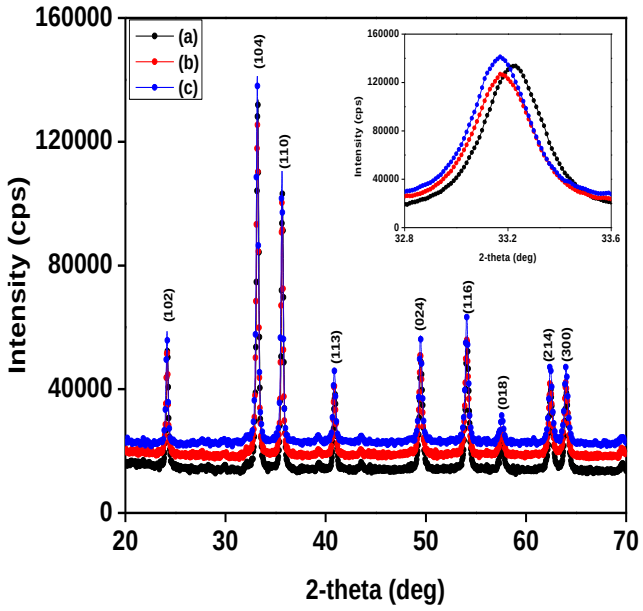

Figure 5. 1 XRD pattern of Ho and Yb co-doped α-Fe_2O_3 (a) 0.1mol%Ho:0.75mol%Yb, (b) 0.1Mol%Ho:0.9mol%Yb and (c) 0.1mol%Ho:1.05mol%Yb.

The phase transformation and crystallinity of the α-Fe_2O_3:Ho^{3+}: Yb^{3+} nanoparticles were identified using RIGAKU SmartLab diffractometer with Cu kα radiation of wavelength 1.5405 Å through the angular range 20° - 70°. Fig 5.1 shows the powder x-ray diffraction pattern of α-Fe_2O_3:Ho^{3+}: Yb^{3+} nanoparticles recorded at room temperature. All the observed diffraction peaks are assigned to the α-Fe_2O_3 (JCPDS no:081248). No peaks belonging to Ho^{3+} and Yb^{3+} dopants are present in the diffraction pattern. This is an indication that our dopants have replaced the Fe^{3+} ion in the crystal structure.

The (104)-plane intensity is stronger than that of the (110), indicating that the (104) plane is the preferred growth plane and was used to calculate the crystallite sizes. From (a) to (c), the peaks are observed to be shifting to the lower 2θ and broader, indicating the dopants are causing strain into the crystal lattice. The crystalline size was calculated using the Debye Scherer formula equation (eq) 3.1

The strain was calculated using the following formula:

$$\varepsilon = \frac{\beta \, Cos \, \theta}{4} \qquad 5.1$$

Table 5.1 the calculated values of crystallite size and strain.

Sample	Crystalline size (nm)	Strain
(a)	6.3	0.058
(b)	6.5	0.056
(c)	6.8	0.053

The crystallite size was increasing with increasing Yb^{3+} doping concentration. The strain was observed to be decreasing with increasing doping concentration. This is due to the increase in crystallite size of the dopants introduced into the structure, which causes more and more distortion in the crystal structure. This resulted in the change in the lattice parameters, which is due to the difference in ionic radii between the host and the Ho^{3+} and Yb^{3+} ions, as well as the change in doping concentrations. See table 5.2.

Table 5.2 Lattice parameters of sample (a), (b) and (c).

Lattice parameters	(a)	(b)	(c)
a = b	5.0380 Å	5.0380 Å	5.0355 Å
c	13.7720 Å	13.7720 Å	13.7474 Å

5.3.2. XPS

For additional characterization to prove ionization states of the rare earth ions, XPS analysis was performed. The XPS analysis shows the 2p Fe, 1s O, 4d Ho and Yb core levels spectra, which are fitted to account for the oxidation states. The Ho 4d spectra did not show any peaks, this may be due to the amount of Ho ions doped with which is 0.1mol %. The $2p_{3/2}$ and $2p_{1/2}$ main peaks are accompanied by satellite structures on their higher binding energy side, at about 8eV. The typical

binding energy value for ferric oxides reported in literature is 711 eV for the $2p_{3/2}$ main peak [11]. From Fig 5.2, the $2p_{3/2}$ peak appears to be narrower and stronger than that of the $2p_{1/2}$ and the area is larger due to the spin orbit (j-j) coupling, where Fe $2p_{1/2}$ has only two but $2p_{3/2}$ has four degeneracy sites [12].

The Fe 2p doublet peaks were each deconvoluted on a Shirley-type background. The wide peak located at 709 eV ($2p_{3/2}$) and 722 eV ($2p_{1/2}$) are attributed to Fe-O bonds. The 711 eV ($2p_{3/2}$) and 724 eV ($2p_{1/2}$) are attributed to Fe-O bonds for Fe^{3+} [13]. The Peak around low binding energy at 707.6 eV is attributed to Fe $2p_{3/2}$ in pure Fe, which indicates that the particles sized of our nanoparticles are very small [14]. O 1s peak has been deconvoluted to four peaks located at 526.7 eV, 527 eV, 528.7 eV and 529.9 eV. The 526.7 eV and 527 eV are very close to each other. The binding energy at 529.9 eV arises from the oxygen in long O-Fe bonds.

Yb compound show many interesting physical phenomena, e.g. mixed valence and existence of heavy fermions. The environment of Yb changes depending on the host matrix and the lattice constant changes considerably. The valence of the ions is usually influence by the lattice constant with the tendency to induce a mixed valence [15]. The XPS spectra of Yb 4d core-level is shown in Fig 5.2. Three pronounce peaks are observed centered at 182.8 eV, a weak peak at 189 eV and an additional peak at 196 eV. The peak at 182.8 eV and 189 eV are assigned to the spin orbit split 4d level, $4d_{5/3}$ and $4d_{3/2}$, respectively. To monitor the oxidation state and the valence state, the energy of $4d_{5/3}$ peak is used. The value of 182.8 eV coincide well with that of Yb_2O_3. The peak at 196 eV is an indicative of the advance oxidation state of Yb, with dominants +3 valence state, which is a characteristic of Yb_2O_3. The peak is usually assigned to the $4f^{13}$ configuration of Yb ion [16].

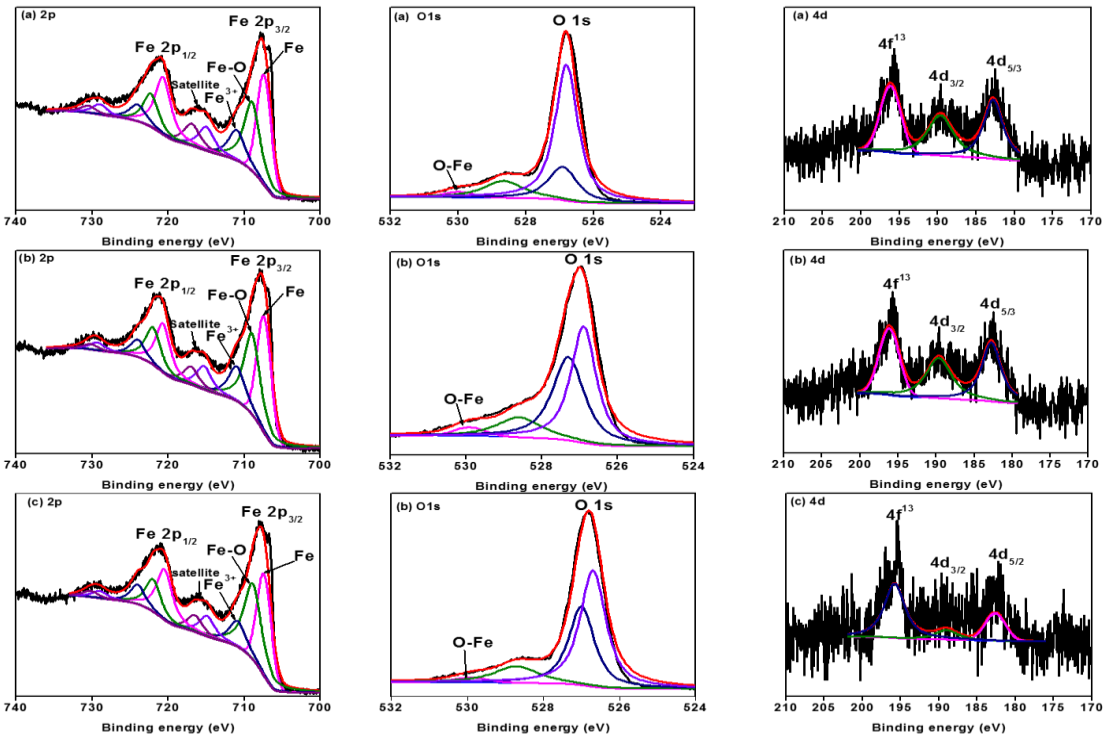

Figure 5. 2 XPS spectra of Ho and Yb co-doped α-Fe_2O_3 (a) 0.1mol%Ho:0.75mol%Yb, (b) 0.1Mol%Ho:0.9mol%Yb and (c) 0.1mol%Ho:1.05mol%Yb.

5.3.3. Reflectance

The reflectance spectra were measured by a Lambda 1050 spectrophotometer with an integrating sphere in the range of 300 nm to 2000 nm. The spectra exhibit that of the bulk hematite with some band arising from the dopants. The spectrum shown in Fig 5.3 is characterized by a very low to nearly constant reflectivity from 300 nm to 550 nm. An increase in reflectivity is observed from 550 nm to 740 nm. From 740 nm – 900 nm there is a slight decrease in reflectivity. Thereafter from 900 nm – 1500 nm there is a rapid increase in reflectivity reaching nearly 100 %. From 1500 nm to 2000 nm it shows a nearly constant reflectivity with some bands from the dopants, Ho ions.

The spectra show prominent band centered at 870 nm, 675 nm and 550 nm which are from the α-Fe_2O_3. The band centered at 870 nm, 675 nm and 550 nm are assigned to $^6A_1 \rightarrow {}^4T_1$ (^4G) and $^6A_1 \rightarrow {}^4T_2$ (^4G) ligand field transition of Fe^{3+}, as well as the $^6A_1 + {}^6A_1 \rightarrow {}^4T_1$ (^4G) + $^4T_1$ (^4G) 'double exciton process' of the simultaneous excitation of the two adjacent Fe^{3+} centers, respectively [17]. The band at ultraviolet region centered at 326 nm is attributed to the ligand-to-metal charge transfer

between the O_{2p} orbital to the Fe^{3+} $2t_{2g}$ and 3_{eg} orbital [9], and also partly from the contributions of the Fe^{3+} ligand field transition at $^6A_1 \rightarrow {}^4T_2$ (^4D) [18]. The two bands from 1200 nm → 2000 nm centered at 1945 nm and 1390 nm are attributed to $^5I_8 \rightarrow {}^5F_7$: Ho^{3+} transition and $^2F_{5/2} \rightarrow {}^2F_{7/2}$: Yb^{3+} transition, respectively. These bands show the presence of dopants in the prepared nanoparticles [19].

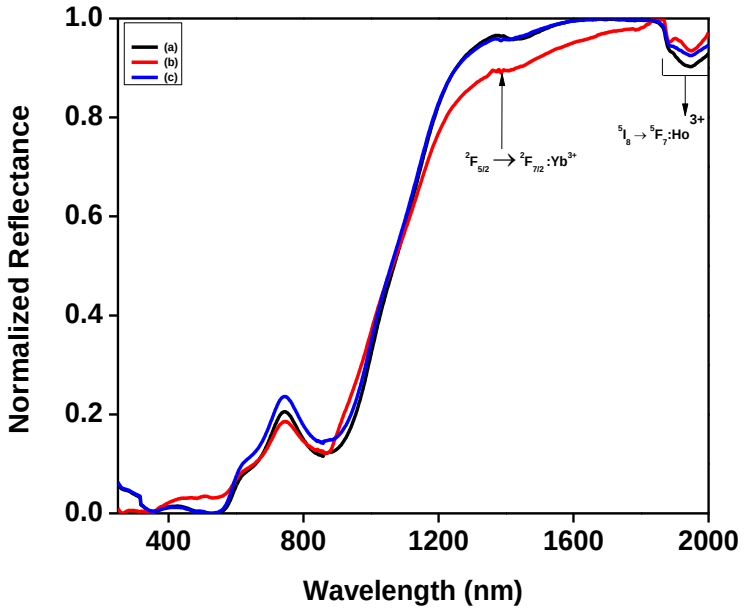

Figure 5. 3 Diffused Reflectance spectra of Ho and Yb co-doped α-Fe_2O_3 (a) 0.1mol%Ho:0.75mol%Yb, (b) 0.1Mol%Ho:0.9mol%Yb and (c) 0.1mol%Ho:1.05mol%Yb.

The energy band gap (E_g) is a characteristic feature of all materials which determine their application potential. It depends not only on the material but on its characteristics like crystallinity and stoichiometry. Diffused reflectance is a simple but powerful spectroscopic tool to estimate the band gap of powder samples unambiguously. The band gap has been estimated using a Kubelka-Munk equation (eq) 3.2.

A plot of $(F(R)*hv)^2$ v/s hv is plotted and an extrapolation of a straight line at K= 0 is made to estimate the band gap as shown in Fig 5.4. The band gap was observed to be decreasing with an increase in the concentration of Yb [from (a) to (b)] and increasing with a further increase in the concentration of Yb [from (b) to (c)]. The main contribution to the shift of the band gap is the self-

energies of the electrons and holes interacting with the phonons. Since the phonon number is fluctuating, the band energy is also fluctuating resulting in an exponential absorption tail below the average band-gap energy [20].

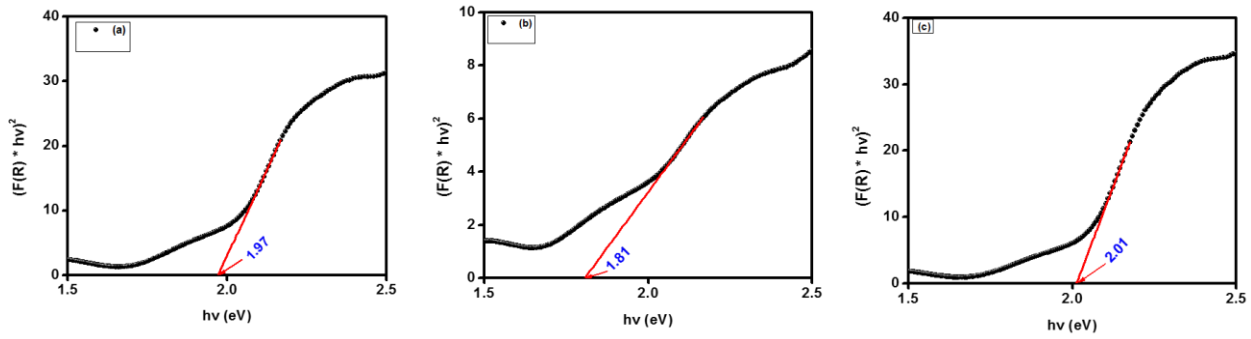

Figure 5. 4 Band gap determination of Ho and Yb co-doped α-Fe_2O_3 (a) 0.1mol%Ho:0.75mol%Yb, (b) 0.1Mol%Ho:0.9mol%Yb and (c) 0.1mol%Ho:1.05mol%Yb.

5.3.4. VSM

The magnetization measurements were preformed using a vibrating sample magnetometer at room temperature with the applied field varied from ±10000 Oe. The hysteresis loop was obtained by measuring the irreversible change in the magnetization of the samples when applying cycling positive and negative values of magnetic fields. Among the different parameters that can be extracted from the hysteresis loop, three can provide us with the basic information needed to describe the magnetic behavior of the material under study. The saturation magnetisation (M_S) is essentially the limit value to which the curve tends within the high-field region, and is reached when all the magnetic moments in the material are aligned with the external field. Upon field decreasing, the sample does not recover its unmagnetised state, retaining a certain amount of magnetisation at zero field: the remanence or remanent magnetisation (M_r). The third parameter is also a consequence of the irreversible character of magnetic hysteresis; the coercivity or coercive field (H_c) represents the field we need to apply to completely demagnetise the sample [21].

Fig 5.5 shows the variation of magnetization *M* as a function of magnetic field *H*. the curves shows a well-defined hysteresis loop with remnant magnetization of 0.09 emu/g, 0.14 emu/g, 0.16 emu/g and 0.13 emu/g for sample (a), (b), (c) and (d), respectively. This magnetization is due to the magnetic exchange interaction between neighboring atoms which are so powerful that they are able to align the ferromagnetic atomic moments despite the continual disturbance of thermal

agitation. The loop shows a ferromagnetic behavior. The coercivity was observed to be 92 Oe, 2427 Oe, 2781 Oe and 2803 Oe for sample (a), (b), (c) and (d), respectively, the coercively increased with increasing Yb concentration. This is an Indication that the impurities play an important role in the magnetization. The magnetization saturation was not reached at the field of 10000 Oe.

The remanent was observed to be increasing with an increase in the concentration of Yb [from (a) to (c)] and decreases with a further increase in the concentration of Yb [from (c) to (d)]. Since the magnetization of ferromagnetic materials are very sensitive to the morphology and structure of the host, the higher coercivity may be attributed to the shape of the anisotropy of the dopants, which prevent them from magnetization in direction, except their easy magnetic axes, hence a large coercivity [22]. In Fig 5.6 we have employ low temperature measurements. The M_r and H_c were observed to be decreasing as the temperature decreases from room temperature to 5K, to observe the change in magnetism and its effects. As the magnetic behavior depends on the crystallinity, particle size and extent of cation substitution, crystallinity of our material tend to lower the M_r and H_c at all temperatures. The properties of the material then change to anti-ferromagnetic behavior upon further decrease of the temperature from 50 K to 5 K. This is due to the interaction between particles classified as the dipole-dipole interaction and exchange interaction. Both the interactions change the magnetic properties of magnetic materials [23].

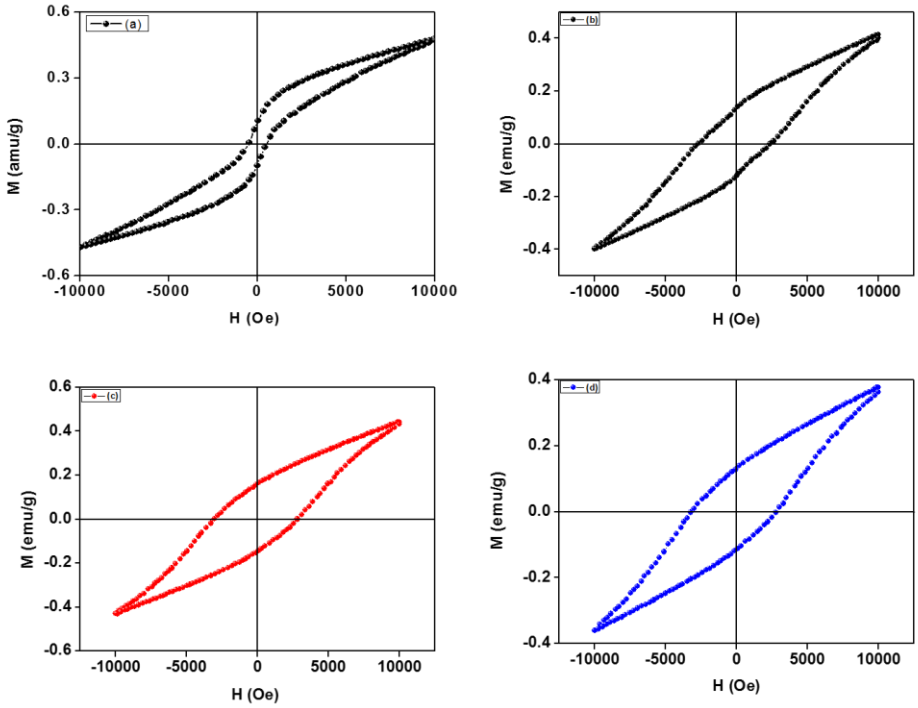

Figure 5. 5 Hysteresis loop for un-doped (a) and Ho and Yb co-doped α-Fe_2O_3 (b) 0.1Ho:0.75Yb:αFe_2O_3, (c) 0.1Ho:0.9Yb:α-Fe_2O_3 and (d) 0.1Ho:1.05Yb:α-Fe_2O_3.

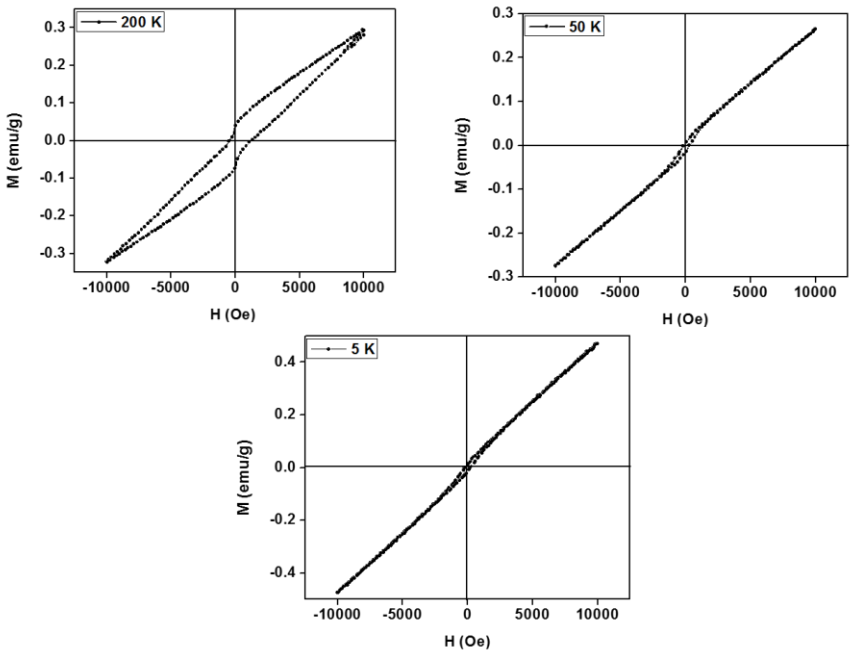

Figure 5. 6 Hysteresis loop for 0.1Ho:1.05Yb:α-Fe_2O_3 at temperature 200K, 50K and 2K.

5.4. Conclusion

α-Fe_2O_3 was successfully co-doped with Ho^{3+} and Yb^{3+} ions using the sol-gel method. The crystallite size was observed to be increasing with increasing Yb concentration. This is due to the strain induced while co-doping. However, the band gap was observed to be increasing with increasing Yb dopant, this would indicate that our material emits more in higher concentration. The hysteresis loop was observed from the VSM where the nanomaterial shows the ferromagnetic properties. This property could assist the nanomaterial to be applied in Bio-imaging.

References

[1] K. Raja, M. Mary Jaculine, M. Jose, S. Verma, A. A. M. Prince, K. Ilangovan, K. Sethusankar, and S. Jerome Das, "Sol–gel synthesis and characterization of α-Fe2O3 nanoparticles," *Superlattices Microstruct.*, vol. 86, pp. 306–312, 2015.

[2] M. Pedroni, F. Piccinelli, S. Polizzi, A. Speghini, M. Bettinelli, and P. Haro-gonzález, "Upconverting Ho – Yb doped titanate nanotubes," *Mater. Lett.*, vol. 80, pp. 81–83, 2012.

[3] M. S. Dhlamini, G. H. Mhlongo, H. C. Swart, and K. T. Hillie, "Energy transfer between doubly doped Er^{3+}, $Tm^{3+}$and Ho^{3+} rare earth ions in SiO_2 nanoparticles," *J. Lumin.*, vol. 131, no. 4, pp. 790–794, 2011.

[4] L. Chen, X. Yang, J. Chen, J. Liu, H. Wu, H. Zhan, C. Liang, and M. Wu, "Continuous shape- and spectroscopy-tuning of hematite nanocrystals," *Inorg. Chem.*, vol. 49, no. 18, pp. 8411–8420, 2010.

[5] M. Tadic, M. Panjan, V. Damnjanovic, and I. Milosevic, "Magnetic properties of hematite (α -Fe2O3) nanoparticles prepared by hydrothermal synthesis method," *Appl. Surf. Sci.*, vol. 320, no. September 2014, pp. 183–187, 2016.

[6] Y. Yamanoi, S. Nakashima, and M. Katsura, "Temperature dependence of refectance spectra and color values of hematite by in situ, high-temperature visible micro-spectroscopy," *Am. Mineral.*, vol. 94, no. 1, pp. 90–97, 2009.

[7] A. S. Teja and P. Y. Koh, "Synthesis, properties, and applications of magnetic iron oxide nanoparticles," *Prog. Cryst. Growth Charact. Mater.*, vol. 55, no. 1–2, pp. 22–45, 2009.

[8] B. Issa, I. M. Obaidat, B. A. Albiss, and Y. Haik, "Magnetic nanoparticles: Surface effects and properties related to biomedicine applications," *Int. J. Mol. Sci.*, vol. 14, no. 11, pp. 21266–21305, 2013.

[9] J. Wang, W. B. White, and J. H. Adair, "Optical properties of hydrothermally synthesized hematite particulate pigments," *J. Am. Ceram. Soc.*, vol. 88, no. 12, pp. 3449–3454, 2005.

[10] W. Xu, B. A. Bony, C. R. Kim, J. S. Baeck, Y. Chang, J. E. Bae, K. S. Chae, T. J. Kim, and

G. H. Lee, “Mixed lanthanide oxide nanoparticles as dual imaging agent in biomedicine,” *Sci. Rep.*, vol. 3, pp. 1–10, 2013.

[11] T. Fujii, F. M. F. De Groot, G. A. Sawatzky, F. C. Voogt, T. Hibma, and K. Okada, “In situ XPS analysis of various iron oxide films grown by NO_2-assisted molecular-beam epitaxy,” *Phys. Rev. B*, vol. 59, no. 4, p. 3195, 1999.

[12] T. Yamashita and P. Hayes, “Analysis of XPS spectra of Fe2+ and Fe3+ ions in oxide materials,” *Appl. Surf. Sci.*, vol. 254, no. 8, pp. 2441–2449, 2008.

[13] M. hafiqur Rahman, S. Ghose, J. R. Gatabi, J. s Rojas-Ramirez, R. K. P. And, and R. Droopad, “Heteroepitaxial growth and characterization of $BiFeO_3$ thin film on GaAs,” *Mater. Res. express*, vol. 3, no. 10, 2016.

[14] Y. Huo, W. Li, D. Min, D. Wang, H. Liu, and Q. Kong, “Zero-valent iron nanoparticles with sustained high reductive activity for carbon tetrachloride,” *RSC Adv.*, vol. 5, pp. 54497–54504, 2015.

[15] Z. GoŁacki and M. Heinonen, “Valency of Yb in PbS and PbTe determined by XPS,” *Acta Phys. Pol. A*, vol. 91, no. 4, pp. 775–778, 1997.

[16] R. J. Iwanowski, J. W. Sobczak, and Z. Kaliński, “X-ray photoelectron study of Yb-doped InP,” *Acta Phys. Pol. A*, vol. 91, no. 4, pp. 809–813, 1997.

[17] L. Lu, L. Li, X. Wang, and G. Li, “Understanding of the Finite Size Effects on Lattice Vibrations and Electronic Transitions of,” pp. 17151–17156, 2005.

[18] Y. P. He, Y. M. Miao, C. R. Li, S. Q. Wang, L. Cao, S. S. Xie, G. Z. Yang, B. S. Zou, and C. Burda, “Size and structure effect on optical transitions of iron oxide nanocrystals,” *Phys. Rev. B - Condens. Matter Mater. Phys.*, vol. 71, no. 12, pp. 1–9, 2005.

[19] V. H. M. A., M. M. G. Alejandrina, J. L. Lucio Mart??nez, and A. V. Kir’yanov, “Enhanced near-infrared emission from holmium-ytterbium co-doped phosphate glasses containing silver nanoparticles,” *Appl. Spectrosc.*, vol. 68, no. 11, pp. 1247–1253, 2014.

[20] T. Skettrup, “Urbach’s rule derived from thermal fluctuations in the band-gap energy,” *Phys. Rev. B*, vol. 18, no. 6, pp. 2622–2631, 1978.

[21] D. Ortega, “Structure and magnetism in magnetic nanoparticles,” *Magn. nanoparticles from Fabr. to Biomed. Clin. Appl.*, pp. 3–44, 2011.

[22] D. VARSHNEY and A. YOGI, “Structural, vibrational and magnetic properties of Ti substituted bulk hematite: α-Fe2-xTixO3,” *J. Adv. Ceram.*, vol. 3, no. 4, pp. 269–277, 2014.

[23] Marin Tadic a,⇑, Nada Citakovic b, Matjaz Panjan c, Boban Stanojevic d, Dragana Markovic a,Đord-e Jovanovic e, Vojislav Spasojevic, 'Synthesis, morphology and microstructure of pomegranate-like hematite(a-Fe2O3) superstructure with high coercivity', Journal of Alloys and Compounds 543, 118–124, 2012.

Chapter6: Luminescence and magnetic properties of Tm^{3+} doped α-Fe_2O_3 nanomaterials

6.1. Introduction

In the last few years many scientific groups have been devoted to developing and improving the properties of magnetic nanomaterials. Synthesis conditions must be well controlled to obtain fine powders with a narrow particle size distribution as well as desired crystallinity of the particles, in order to achieve applicable properties. There has been great interest in iron oxide nanoparticles which currently focuses on controlling their magnetic, electric, optical and catalytic properties [1]. Due to these properties, the iron oxide nanoparticles have emerged as a versatile material for different applications [2]. Many forms of existence of iron oxide is found in nature, magnetite (Fe_3O_4), maghemite (γ-Fe_2O_3) and hematite (α-Fe_2O_3) are the most common. Magnetite has been considered an ideal candidate for biological applications, both as tag for sensing and imaging, and as an activity agent for antitumor therapy. Both magnetite and maghemite have attracted attention in biomedical application because of their biocompatibility and low toxicity in human body. Hematite, on the other hand, has great scientific and technological importance since this material can be used in information storage, color imaging, magnetic refrigeration, gas sensing and so on [3].

Due to its instinctive environmentally friendly, nontoxic, corrosion-resistance and thermal stability, α-Fe_2O_3 is well known magnetic semiconductor with a band gap of around 2.1 eV [4], where the conduction band is composed of empty d-orbitals of Fe^{3+} and the valence band consists of occupied 3d crystal field orbitals of the Fe^{3+} with some admixture from the O 2p non-bonding orbitals. The Fe^{3+} occupy two-thirds of the octahedral sites that are confined by the nearly ideal hexagonal closed-packed O lattice [5]. At low temperature, pure stoichiometric bulk α-Fe_2O_3 is a collinear antiferromagnetic (AF) material, with spin aligned along the magnetically easy c-axis of its rhombohedral crystal structure. As the temperature increases, a magnetic transition is observed at $T_M \approx 265$ K. At this point the spin flop into the basal plane as a result of the antisymmetric Dzialoshinskii-Moriya exchange interaction, and take on a weakly ferromagnetic (WF) ordering

with spin canting of a fraction of a degree [6]. Many methods have been employed to synthesize the α-Fe_2O_3, Microwave [7], sol-gel [8], hydrothermal [9], combustion [10] etc.

The nanocomposites containing luminescent and magnetic characteristics are trending in a wide range of applications, such as bio-imaging, diagnostic, and therapeutics. Magnetic iron oxide nanoparticles have in the meanwhile been proven to be promising, hence allowed in the wide range of biomedical applications[11]. Rare earth ions can be incorporated in the host lattice and thereby altering their properties. It takes an addition of very small amount of rare earth ions to ferrite samples to alter their electrical, magnetic and structural properties depending upon the type and amount of rare earth used. Rare earth can be divided into two categories, one with radius close to Fe ions and other with the radius greater than Fe ions [12]. In this work, we report on the doping of Tm ions into α-Fe_2O_3 nanoparticles to study the magnetic and luminescence properties for imaging application.

6.2. Synthesis method

Microwave synthesis was used to synthesize α-Fe_2O_3 and α-Fe_2O_3:Tm. Microwave irradiation has become widely used as a rapid heating method for the synthesis of iron oxide nanoparticles. It also reduces the reaction time and increases product yield when compared to conventional heating methods [13]. Ferric chloride, Urea as fuel, Polyethylenglycol and thulium nitrate were used as precursors. Thulium was added in the molar concentration of 0.2, 0.4 and 0.6 mol%. The mixture was dissolved in distilled water and irradiated in the microwave with power of 750 W for 15 minutes. The final product was collected and centrifuged, washed with deionized water and air-dried at 100℃ for 1 hour. The dried powder was then annealed in the microwave oven at 600 ℃ for 4 hours to obtain a crystalline powder. The powder was ground and characterized using XRD, SEM, PL and VSM.

6.3. Characterization Techniques

6.3.1. Structural properties

The room temperature X-ray diffraction (XRD) pattern of Tm doped α-Fe_2O_3 in Fig 6.1 shows a rhombohedral phase of α-Fe_2O_3, with space group $R\bar{3}C$. The phase was confirmed by using a Rigaku SmartLab diffractometer, equipped with Cu Kα radiation of λ = 1.5405 Å. The XRD was operated at the voltage of 40 kV and current of 200 mA. All diffraction peaks were observed to be of pure α-Fe_2O_3 with no impurities peaks. The (104) plane was found to be the preferred orientation of the material. Fig 6.1(B), shows the zoomed spectra of the 104 plane. We observed a shift in peak position to lower angle (from sample (a) to (c)) with the shift difference of two theta 0.1° which is due to an increase in d-spacing, as the Tm doping concentration increases and a shift to the higher angle from (c) to (d). The shift in peak position strongly depends on the interplanar spacing (dhkl) and average crystallite size (d). Since the interplanar spacing is inversely proportional to the peak position, it is the one mostly responsible for the shifting of the peak. From (a) to (b) the interpanar spacing is increasing as the size decreases. The higher angle shift from (d) to (e) shows that the interplanar spacing becomes longer thereby creating stress on the host material. Similar finding have been reported on Tm^{3+} doped ZnO [14]. The intensity decreases almost half as the Tm doping increases. Therefore, the shift in diffraction peaks of the samples is due to the difference in ionic radii of Fe^{3+} (1.25Å) and Tm^{3+} (1.75 Å). However, the addition of Tm^{3+} into α-Fe_2O_3 led to the replacement of the Fe^{3+} by Tm^{3+} ions. This then causes the lattice strain in the materials. The lattice parameters decreased with increased Tm doping concentration. The crystal parameters are listed in table 6.1.

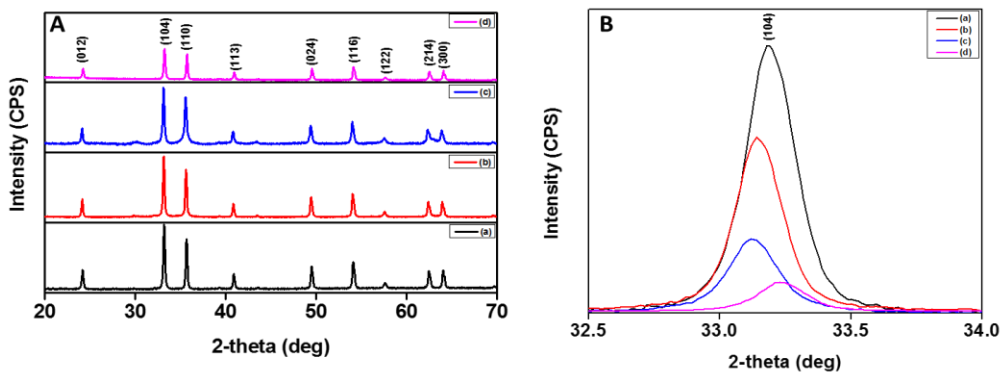

Figure 6. 1 (A) XRD pattern of Tm:α-Fe_2O_3 nanoparticles with different concentration of (a) 0.0mol %, (b) 0.2 mol %, (c) 0.4 mol % and (d) 0.6 mo l%. Fig 6 (B), shows the preferred orientation of peak (104) showing the effect of Tm.

Table 6. 1 Crystal size and lattice parameters.

Tm^{3+} Concentration (Mol%)	**2- theta (deg.)**	**d-spacing (Å)**	**Crystallite size (nm)**	**Lattice constants (Å)**		
				a	**b**	**c**
0.0	33.16	2.6996	0.992	5.033	5.033	13.754
0.2	33.13	2.7015	0.989	5.040	5.040	13.759
0.4	3.3.12	2.7022	0.906	5.042	5.042	13.757
0.6	33.23	2.7029	0.796	5.046	5.046	13.758

6.3.2. Luminescence

It was repoted that the bulk α-Fe_2O_3 does not produce luminescence. However, the luminescence from the α-Fe_2O_3 nanomaterials is due to local forbiden d-d transition, resonant energy transfer between cations, and efficient lattice and magnetic relaxations. The self trap states have been observed in hematite nanostructures due to their size- associated optical properties, and quantum confinement effect [13]. The optical properties of the Tm doped α-Fe_2O_3 are determined by the chemical nature of their constituents (doping ion and matrix). Their luminescence is in most cases due to forbidden transitions among different f-electron configurations of the Tm^{3+} ions [15]. Fig 6.2(A), shows the luminescence emission of Tm doped α-Fe_2O_3 excited by a 320 nm zenon lamp at room temperature. The luminescence shows an increase in emission intensity from sample (a)

to (b) and a decrease from (b) to (c). The decrease in intensity is referred to as luminescence quenching, which could be due to increase in Tm doping concentration. The emission peaks were observed from the deconvoluted spectra in Fig. 6.2 (B) and centered at 412 nm, 433 nm, 466 nm and 453 nm. Emission peak at 412 correspond to the violet luminescence and is due to the radiative defects related to interface trap existing at the grain boundaries. Emission at 433 nm and 466 nm are related to the deep level emisions and mainly results from defects such as interstitials and oxygen vacancies. The peak at 453 nm is due to luminescence centers in the material [16]. These emission peaks are from the host material α-Fe_2O_3. The peaks appered to be centered at the same position for all three samples as the Tm concentration increases.

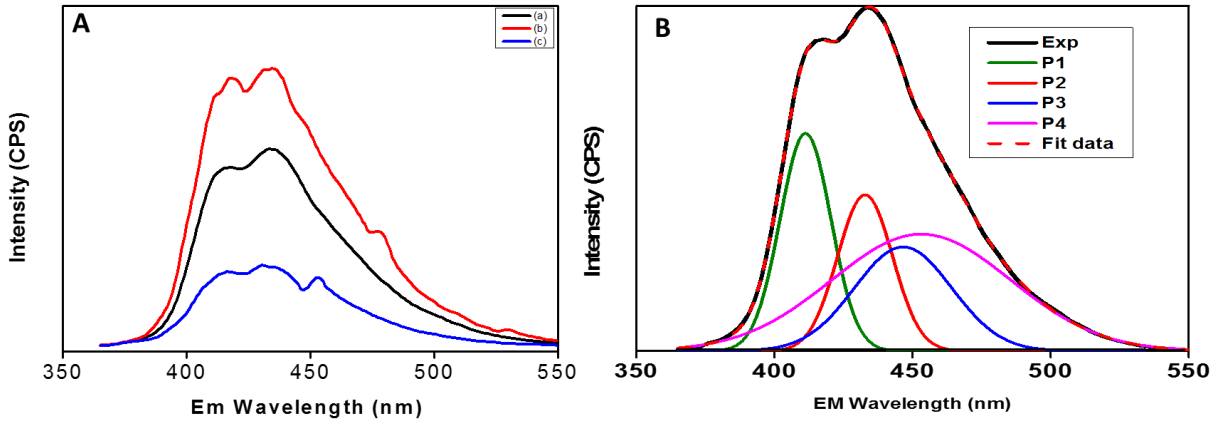

Figure 6. 2 (A), Photoluminescence spectra of Tm:α-Fe_2O_3 with different concentrations (a) 0.2 mol%, (b) 0.4 mol% and (c) 0.6 mol% : (B), Deconvoluted photoluminescence emission spectra of 0.mol% Tm:α-Fe_2O_3.

6.3.3. Diffused reflectance

The UV-Vis diffuse reflectance of Tm^{3+} doped α-Fe_2O_3 nanomaterials was measured using the 1050 UV-Vis-NIR spectrophotometer. The spectra are shown in Fig 6.3. Below 500 nm the spectra show low reflectance nature of the materials and thereafter increases the rapidly around 560 nm. The increase around 560 nm indicates that the band gap is about 2.1 eV. The transition below 500 nm are due to ligand-to-metal charge transfer [17]. The absorption at 550 nm is assigned to the $2^6A_1 \rightarrow 2^4T_1$ excitation of the an Fe-Fe pair [18], possibly overlapped the contributions of $^6A_1 \rightarrow ^4E$, $^4A_1(4G)$ ligand field transition and the charge-transfer band tail [19]. The absorption around 660

nm is assigned to $^6A_1 \rightarrow {}^4T_1$, which arise from the spin-forbidden ligand field transition and in the red range of the spectrum, indicating the color of our material[4]. The absorption in the NIR is assigned to the ground state transition of Tm^{3+} from $^3H_6$ to $^3H_5$ [20].

The band gap extrapolation is shown in Fig 6.3(B). The band gap was observed to be decreasing with decreasing crystallite size of the material from 2.12, 2.11 eV to 2.08 and 2.05 or sample (a), (b), (c) and (d), respectively. The 2.12 eV and 2.11 eV band gap exhibit an absorption threshold in our material, which is attributed to band gap exciton. The un-doped sample show a weak confinement, which caused an enhancement in band gap. After Tm^{3+} doping, the surface pressure increases and causes an increase in lattice strain, which decreases the band gap from 2.012 eV to 2.05 eV. The decrease in bandgap to higher wavelength is caused by the larger strain, where the band gap is said to be red shifted. Therefore, the surface and interface effects cause the red shift, which is responsible for the reduction of the band gap [21]. The 2.08 eV and 2.05 eV band gaps are attributed to the charge transfer excitation at couples Fe^{2+}- Tm^{3+} impurities that marks the extrinsic band gap [22].

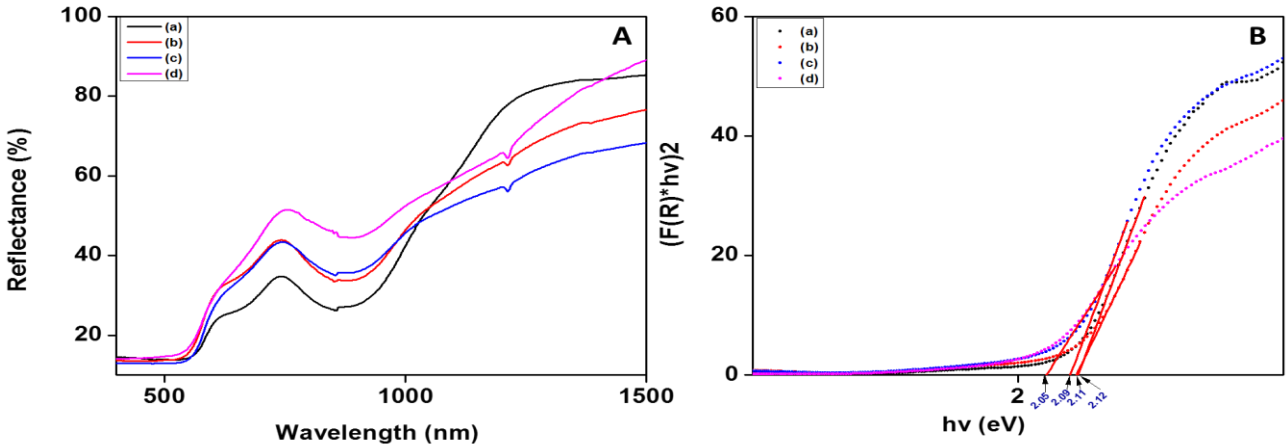

Figure 6. 3 (A) Reflectance spectra of Tm doped α-Fe_2O_3 with different Tm concentrations (a) 0.0 mol%, (b) 0.2 mol%, (c) 0.4 mol% and (d) 0.6 mol%, Figure 3(B) corresponding band gaps.

6.3.4. Magnetic Properties

It has been reported that the highest efficiency in clinical research has been demonstrated by supperparamagnetic nanoparticles with average sizes less than 20 nm and with narrow size distribution. Therefore, identification of atomic, electronic and magnetic structure of the iron oxide nanoparticles is an important task needed for the optimization of the methods for nanoparticles synthesis for the certain bio-medical requirements [23]. The rare earth ions are found to be promising additive to improve the magnetic properties of iron oxide. The magnetization hysteresis curve of the Tm doped α-Fe_2O_3 nanopartricles at room amd low tempetarures were measured using a vibrational-smaple magnetometer (VSM). The curves shows the hysteresis loop of the applied field (H) v/s the induced magnetization. Figure 6.4(A) shows the hysteresis loop of sample 1 and figure 6.4(B) is for sample 2. A sharp increase of magnetization was observed when applied field was increased form 0 to 10 000 Oe. Both samples exhibit paramagnetic behavior at room temperature. The materials were found to have a spherical shape (Fig 6.5) and the diameter in the nano range. The Morin transition has been shown to be strongly affected by strain and lattice defects as indicated in the XRD results [24]. The strain is caused by the incoporation of the Tm rare earth ion. At room temperature (300K), the material exhibit paramagnetic behavior. The contribution of the paramagnetic behavior of our material may be arising from the Tm^{3+} ions. The 2 unpaired electrons in the inner 4f subshells of the Tm^{3+} ions are tightly bound to the nucleus and shielded by the outer closed shell $5d^16s^2$ electrons from the crystal field and are responsible for the magnetic characteristics of the Tm^{3+} ions. Tm^{3+} paramagnetism, arises from the magnetic moment related to the Tm^{3+}ions and are localized and non-interacting. The same behavior was obsererved by N. Shrivastava, when doping the nanomaterial with Gd^{3+} [11].

When the temperature was decrease to 100K, 20K and 5K, the nanomaterials showed ferromagnetic behavior. The ferromangnetic behavior is due to the fact that at T_M, a spin flip transition takes place and the spin aligns parallel to the c-axis, retaining the ferromagnetic coupling within a given plane [24]. This leads to increase in saturation magnetization, retenstivity (Mr) and coercivity (Hc), with decreasing temperature. It can be seen that the coercivity is higher at 5K than at room temperature and the other temperatures. The shape of the hysteresis is due to the surface anisotropy of the particles and magnetic core shell structure resulting in the ununiform reversal of the nanoparticles magnetization. Finite α-Fe_2O_3 is known to be antiferromagnetic under Morin

temperature , Tm = 250K. However, doping with Tm makes it to stay at the ferromangetic regime. The observed values are listed on table 5.

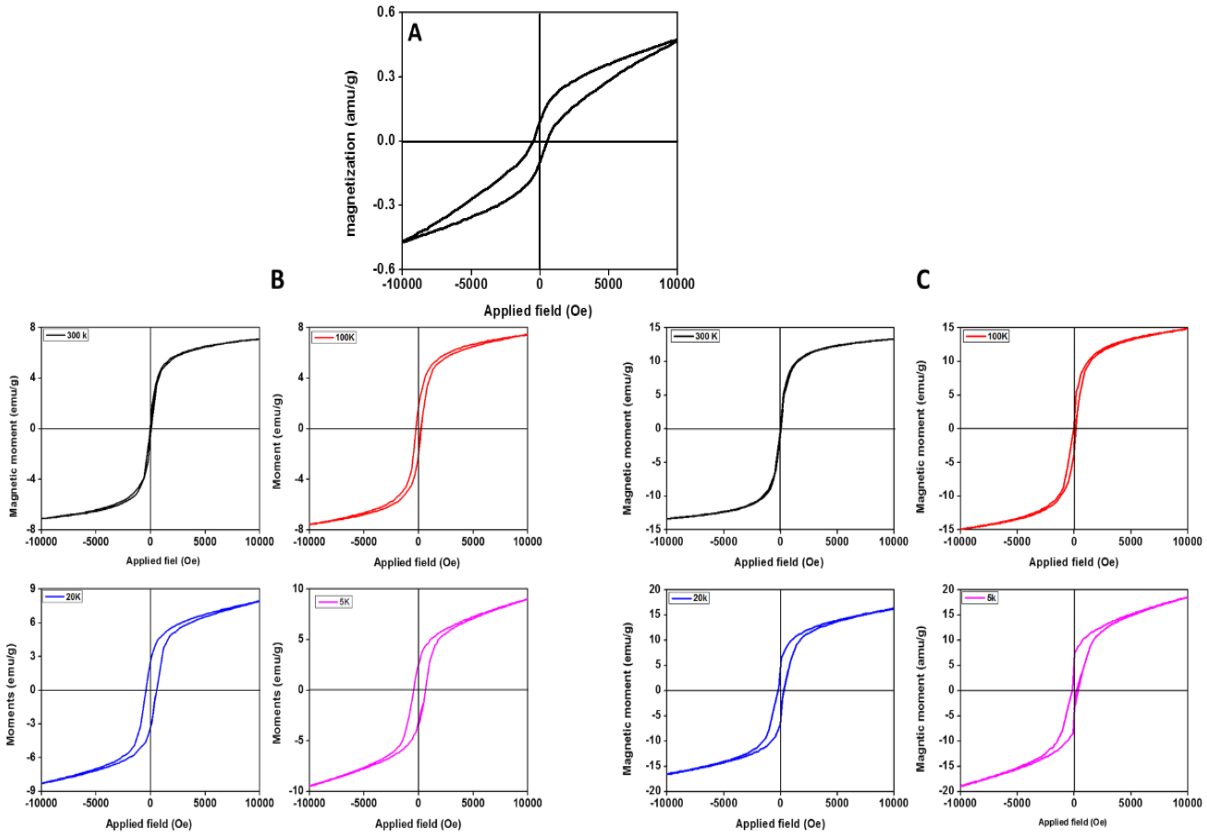

Figure 6. 4 (A), Hysteresis loop for 0.0 mol% Tm:α-Fe_2O_3 , (B)Hysteresis loop for 0.2 mol% Tm:α-Fe_2O_3, (C) Hysteresis loop for 0.6 mol% Tm:α-Fe_2O_3 nanoparticles.

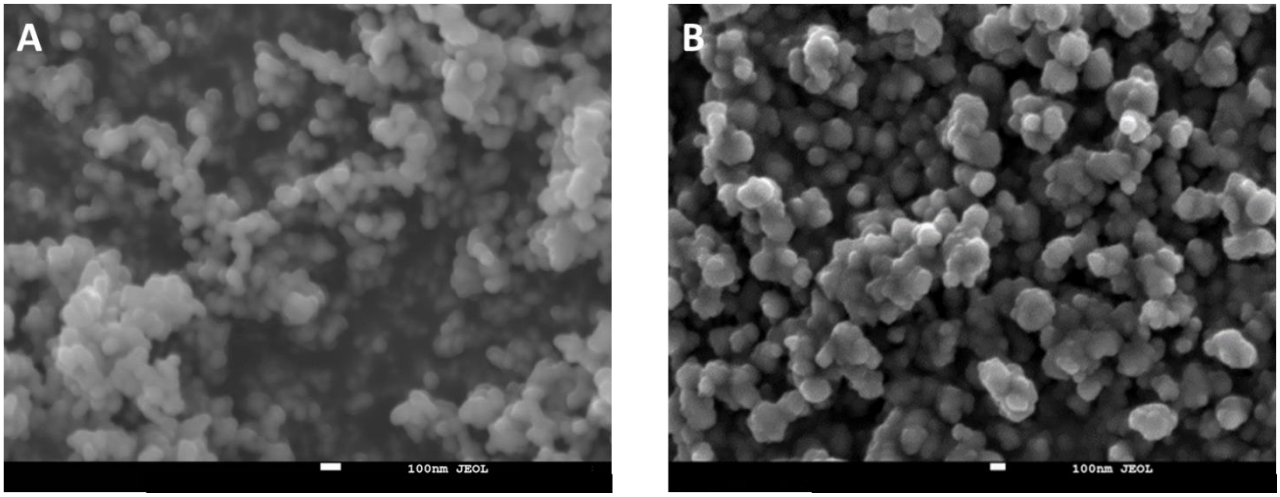

Figure 6. 5 SEM image of (A) α-Fe_2O_3 nanoparticles and (B) Tm: α-Fe_2O_3 nanoparticles.

Table 6. 2 Magnetization data of (A) 0.0 mol% Tm:α-Fe_2O_3 , (B) 0.2 mol% Tm:α-Fe_2O_3, (C) 0.6 mol% Tm:α-Fe_2O_3 nanoparticles

	Sample (A)	Sample (B)				Sample (C)			
	300 k	***300 K***	***100 K***	***20 K***	***5 K***	***300 K***	***100 K***	***20 K***	***5K***
Saturation Magnetization (emu/g)	***0.48***	***6.32***	***7.15***	***7.55***	***7.75***	***11.18***	***13.59***	***14.50***	***16.04***
Rentensivity (emu/g)	***0.10***	***0.53***	***1.386***	***2.78***	***2.59***	***0.01***	***1.78***	***4.39***	***7.52***
Coercivity (Oe)	***41.89***	***20.00***	***23.00***	***96.00***	***175.00***	***39.40***	***100.90***	***110.00***	***192.00***

6.4. Conclusion

We have reported on microwave synthesis of Tm doped α-Fe_2O_3 nanomaterials. The synthesis suggest the successful doping of Tm ions into α-Fe_2O_3 matrix, which was evidence from the XRD. The luminescence observed was found to be dominated by intrinsic defects from the host matrix rather than for the extrinsic defects of the Tm^{3+} ions. The increase in the intensity of the defects emission peak with the introduction of the Tm^{3+} ions was observed. The magnetic hysteresis showed a paramagnetic behavior at room temperature and ferromagnetic behavior below room temperature. The findings suggest that Tm^{3+} ions doped α-Fe_2O_3 nanomaterials with both luminescence and magnetic properties can be used for the development of luminescence-magnetic compound for biomedical opportunities in the field.

References

[1] M. Tadic, M. Panjan, V. Damnjanovic, and I. Milosevic, "Magnetic properties of hematite (α -Fe2O3) nanoparticles prepared by hydrothermal synthesis method," *Appl. Surf. Sci.*, vol. 320, no. September 2014, pp. 183–187, 2016.

[2] D. K. Bora, A. Braun, S. Erat, O. Safonova, T. Graule, and E. C. Constable, "Evolution of structural properties of iron oxide nano particles during temperature treatment from 250 degrees C-900 degrees C: X-ray diffraction and Fe K-shell pre-edge X-ray absorption study," *Curr. Appl. Phys.*, vol. 12, no. 3, pp. 817–825, 2012.

[3] S. Saha and A. K. Bhunia, "Synthesis of Fe 2 O 3 Nanoparticles and Study of its Structural , Optical Properties," vol. 17, no. December, pp. 191–195, 2013.

[4] L. Chen, X. Yang, J. Chen, J. Liu, H. Wu, H. Zhan, C. Liang, and M. Wu, "Continuous shape- and spectroscopy-tuning of hematite nanocrystals," *Inorg. Chem.*, vol. 49, no. 18, pp. 8411–8420, 2010.

[5] W. Wei, W. Zhaohui, Y. Taekyung, J. Changzhong, and K. Woo-Sik, "Recent progress on magnetic iron oxide nanoparticles: synthesis, surface functional strategies and biomedical applications," *Sci. Technol. Adv. Mater.*, vol. 16, no. 2, p. 23501, 2015.

[6] P. G. Bercoff and H. R. Bertorello, "Magnetic properties of hematite with large coercivity", *Applied physics A*, vol. 100, no.4, pp. 1019–1027, 2010.

[7] J.-Y. Hwang, S. Shi, Z. Xu, and K. W. Peterson, "Synthesis of Monodispersed Iron Oxide Particles By a Large-Scale Microwave Reactor," *Chem. Eng. Commun.*, vol. 193, no. 12, pp. 1586–1591, 2006.

[8] L. E. Mathevulaa, L. L. Notoa, B. M. Mothudia, M. Chithambob, and M.S. Dhlaminia, "Structural and optical properties of sol-gel derived α-Fe2O3 nanoparticles," *J. Lumin.*, vol. 192, pp. 879–887, 2017.

[9] M. Mohammadikish, "Hydrothermal synthesis, characterization and optical properties of ellipsoid shape ??-Fe2O3 nanocrystals," *Ceram. Int.*, vol. 40, no.1, pp. 1351–1358, 2014.

[10] P. Dhiman, "Solution combustion preparation of Fe2O3- nano-flakes: Synthesis and characterization," *Adv. Mater. Lett.*, vol. 3, no. 4, pp. 330–333, 2012.

[11] N. Shrivastava, U. Rocha, D. Muraca, C. Jacinto, S. Moreno, J. M. Vargas, and S. K. Sharma, "Magnetic upconverting fluorescent NaGdF 4 :Ln 3+ and iron-oxide@NaGdF 4 :Ln 3+ nanoparticles," *AIP Adv.*, vol. 8, no. 5, p. 56710, 2018.

[12] S. Akbar Hosseini, "Low-cost and eco-friendly viable approach for synthesis of gadolinium doped nickel ferrite nanoparticles using starch," *J. Mater. Sci. Mater. Electron.*, vol. 27, no. 12, p. 7433, 2016.

[13] D. a. Wheeler, G. Wang, Y. Ling, Y. Li, and J. Z. Zhang, "Nanostructured hematite: synthesis, characterization, charge carrier dynamics, and photoelectrochemical properties," *Energy Environ. Sci.*, vol. 5, no. 5, p. 6682, 2012.

[14] G.L Kabongo, Hybrid heterostructure based on poly(3-hexylthiophene-2,5-Dily) (P3HT)-ZnO:RE3+ (RE=Ho, Tm for photovoltaic, University of South Africa, PhD, 2016

[15] C. Bouzigues, T. Gacoin, and and A. Alexandrou, "Biological Applications of Rare-Earth Based Nanoparticles," *ACS Nano*, vol. 5, no. 11, p. 8488, 2011.

[16] M.A. Mahadik, S.S. Shinde, V.S. Mohite, S.S. Kumbhar, K.Y. Rajpure, A.V. Moholkar, C.H. Bhosalen, Photoelectrocatalytic activity of ferric oxide nanocatalyst: A synergestic effect of thickness, Ceramics International 40 (2014) 9463–9471

[17] J. Torrent and V. Barron, "Diffuse reflectance spectroscopy of iron oxides," *Encycl. Surf. Colloid Sci.*, pp. 1438–1446, 2002.

[18] D. M. Sherman and T. D. Waite, "Electronic spectra of Fe3+ oxides and oxide hydroxides in the near IR to near UV.," *Am. Mineral.*, vol. 70, no. 11–12, pp. 1262–1269, 1985.

[19] G. Zhang, Y. Xu, D. Gao, and Y. Sun, "␣ -Fe 2 O 3 nanoplates : PEG-600 assisted hydrothermal synthesis and formation mechanism," *J. Alloys Compd.*, vol. 509, no. 3, pp. 885–890, 2011.

[20] Y. Liu, W. Luo, R. Li, H. Zhu, and X. Chen, "Near-infrared luminescence of Nd3+ and Tm3+ ions doped ZnO nanocrystals," *Opt. EXPRESS 9748*, vol. 17, no. 12, pp. 9748–9753,

2009.

[21] Anjali Jain Deotale and R. V. Nandedkar, Correlation between Particle Size, Strain and Band Gap of Iron Oxide Nanoparticles, Materials Today: Proceedings 3, pp. 2069–2076, 2016.

[22] B. Gilbert, C. Frandsen, E. R. Maxey, and D. M. Sherman, "Band-gap measurements of bulk and nanoscale hematite by soft x-ray spectroscopy," *Phys. Rev. B - Condens. Matter Mater. Phys.*, vol. 79, no. 3, 2009.

[23] T. A. Lastovina, A. L. Bugaev, S. P. Kubrin, E. A. Kudryavtsev, and A. V. Soldatov, "Structural studies of magnetic nanoparticles doped with rare-earth elements," *J. Struct. Chem.*, vol. 57, no. 7, pp. 1523–1528, 2016.

[24] M. Reufer, H. Dietsch, U. Gasser, B. Grobety, A. M. Hirt, V. K. Malik, and P. Schurtenberger, "Magnetic properties of silica coated spindle-type hematite particles," *J. Phys. Condens. Matter*, vol. 23, no. 6, 2011.

Chapter7: Up-conversion luminescence properties of Tm^{3+} and Yb^{3+} co-doped α-Fe_2O_3 nanoparticles

7.1. Introduction

There have been an increase of interest in various transition metal oxides. Binary iron oxides such as α-Fe_2O_3, Fe_3O_4 and γ-Fe_2O_3, are attractive materials, by virtue of their environmental affinity, abundance and low cost [1]. α-Fe_2O_3 is the most chemically stable in ambient conditions of the three polymorphs, because it is non-toxic and bio-compatible. It shows n-type semiconducting properties with a band gap mostly approximated to 2.2 eV, which lies in the visible region [2]. Foreign materials can be introduced into the α-Fe_2O_3 structure to substantially modify its properties, particularly facile for trivalent lanthanide (Ln^{3+}) cations having similar ionic radius [3]. The guest cations may alter the particle size [4] or induce change in optical properties, as observed for La-substituted α-Fe_2O_3 [5]. In our study we doped α-Fe_2O_3 with up-converting rare-earth ions to study the up-conversion luminescent properties of the nanomaterials. Ln^{3+} ions are an attractive class of dopant ions, particularly the trivalent cations due to their peculiar magnetic and optical properties related to their f-electron configuration. Doping α-Fe_2O_3 with Ln^{3+} ions is however challenging, due to the different size of the Fe^{3+} ironic radius compared to that of the lanthanide ions [3].

There have been a wide use of luminescent materials in different technologies nowadays. Other luminescent materials were also investigated, but it has been reported that relatively few of these materials found their way into applications [6]. Ln^{3+} ions, owing to their abundant energy levels of 4f configurations are endowed with unique and fascinating optical properties. Ln^{3+} ions possess real intermediate energy level, which gives out desired emission via various energy transfer pathways. Certain Ln^{3+} ions possess both down-conversion and up-conversion luminescent properties. These lanthanides have received consistent attention due to their excellent photostability and long luminescence lifetime, as well as their large stokes/anti-stokes shift and sharp-band emission [7]. Up-converting (UP) Ln^{3+} ions can be doped into solid-state nanomaterials, which are then called up-conversion nanoparticles (UCNPs). UCNPs are dilute guest host system where Ln^{3+} ions are dispersed as a guest of less than 100 nm in size. The Ln^{3+}

dopants are referred to as optically active centers, which produce emission when excited. Depending on the dopant, UCNPs can display wavelength selective up-conversion, such as NIR to shorter NIR, visible, or UV [8]. Among the research materials, Ln^{3+} ions, such as Er^{3+}, Tm^{3+}, Ho^{3+} and Pr^{3+} are doped as activator ions, because they possess favorable metastable energy levels with long lifetimes. Yb^{3+} has a large absorption cross section at around 980 nm therefore, is doped as a sensitizer and can efficiently transfer the excitation energy to the activator ions [9].

There has been a renewed interest in the spectroscopic properties of the thulium (Tm^{3+}) ions over the past years, particularly in application areas such as optical communication, Bio-imaging and sensing [10]. Non-invasive imaging and minimally invasive in-vivo bio- imaging techniques are valuable tools in the arsenal of clinical diagnostics. Many types of bio-imaging are available, spanning from techniques that enable whole-organism anatomical imaging to others that provide specific molecular imaging at subcellular resolution. Such tools are expected to be pivotal for advancing early-stage cancer diagnosis, guided stem cell therapies, drug delivery, pathogen detection, gene therapy, image-guided surgery, and cancer staging [11]. For bio-imaging uses, the application of particles that presents superparamagnetic behaviour at room temperature is preferred [12]. Intensive research has been recently dedicated to obtain laser radiation in the visible spectrum. Ln^{3+} ions doped solid-state materials can provide an efficient mechanism to obtain blue and green laser radiation. The electronic transitions $^1D_2 \rightarrow {}^3F_4$ and $^1G_4 \rightarrow {}^3H_6$ around 450 and 480 nm, respectively, of Tm^{3+} doped materials can generate blue up-conversion emission [13]. Yb^{3+} being the most active sensitizer, can transfer the electrons to the Tm^{3+}, thereby enabling the Tm^{3+} to emit when co-doped. This is due to Yb^{3+} having the advantage to present only two metastates: the ground state level $^2F_{7/2}$ and the excited state level $^2F_{5/2}$, corresponding to the highly efficiency absorption in the range of 900-100 nm. The level structure is highly desirable for efficient absorption of commercially available laser diodes emitting around 980 nm and avoiding any undesirable excited state absorption under intense optical pumping [14].

In this chapter, we have synthesized an up-converting nanoparticles of α-Fe_2O_3 doped with an optically active sensitizer (Yb^{3+} ions) and activator (Tm^{3+} ions). The mechanisms for the up-conversion process are established and studied at three different Yb^{3+} concentration rations. In addition, we carried out density functional theory calculations to provide further insight on the electronic and optical properties of the pristine and doped α-Fe_2O_3.

7.2. Synthesis method

Microwave synthesis was used to synthesize α-Fe_2O_3:Tm,Yb. Microwave irradiation has become widely used as a rapid heating method for the synthesis of iron oxide nanoparticles. It also reduces the reaction time and increases product yield when compared to conventional heating methods [15]. Ferric chloride, Urea as fuel, Polyethylenglycol, thulium nitrate and ytterbium nitrate were used as precursors, in stoichiometric amounts, in order to achieve 0.2 mol % doping of Tm^{3+} ions, and 2, 4 and 6 mol % co-doping of Yb^{3+} ion. The mixture was dissolved in distilled water and was allowed to react inside a stainless steel vessel. The reaction was subjected to 750 W microwave power for 15 minutes. The final product precipitated at the bottom of the glass tube, and was collected by centrifugation. It was washed with deionized water and dried in air at 80℃ for 1 hours. The dried powder was further annealed inside a microwave assisted oven at 600℃ for 4 hours to obtain a red colored compound. The compound was ground into a fine powder that was characterized using XRD to obtain crystal structure, Scanning electron microscopy (SEM) to observe the surface morphology, Energy dispersive spectroscopy (EDS) for elemental analysis, UV_Vis_NIR spectrophotometer for reflectance studies, Photoluminescence Laser system (PL) for up-conversion studies.

7.3. Characterization techniques

7.3.1. Phase analysis

The structure and phase composition of the samples were investigated using RIGAKU Smart Lab X-ray diffractometer. The measured diffraction patterns are shown in Fig 7.1. The diffraction peaks are observed to be wide and less intense, indicating internal strain on the samples. The positions of major peaks correspond to the rhombohedral phase of α-Fe_2O_3 (PDF: 9000139), with peak 104 being the preferred orientation. Impurity peak corresponding to (002), (111), (020) and (021) diffraction peaks were observed and found to belong to $YbFeO_3$ (card no: 2107089). The crystallite size (D) was estimated using Debye Scherer's equation

$$D \approx \frac{0.9\,\lambda}{\beta cos\theta}, \qquad 7.1$$

where λ is the wavelength of the x-rays, θ is the diffraction angle, and β is the full width at half maximum (FWHM) of the diffraction peak [17]. The estimated D for sample (a) is about 0.32 nm and (b) 0.45 nm. The diffraction peaks are observed to be broad, which support the small crystallite size of the material.

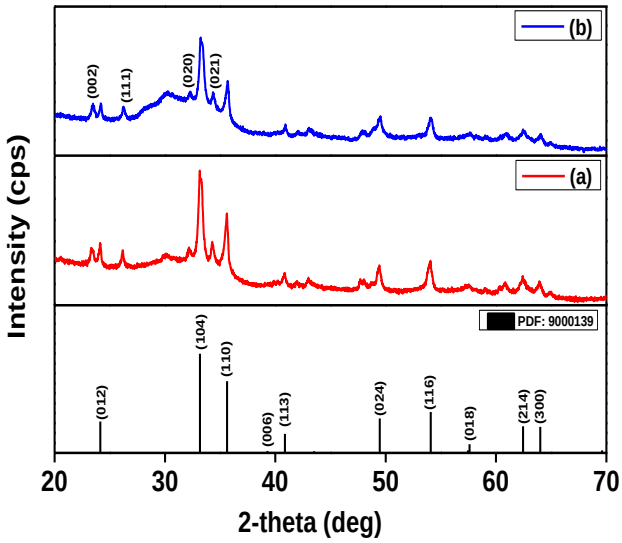

Figure 7. 1 XRD spectra of Tm:Yb co-doped α-Fe_2O_3 (a) 0.2 mol%Tm:2%Yb and (b) 0.2mol%Tm:4%Yb.

7.3.2. Structural properties

The EDS spectra and maps were employed to investigate the chemical composition of the samples, and are shown in fig 7.2 $ 7.3. Several elements were detected as displayed in the EDS spectra and maps, which include C from the carbon tape, Cu from the sample holder, Cl is a residual from the precursors during synthesis, Fe, O, and Yb were from the final product. Tm was not detected and this may be attributed to its low concentration in the sample or peak overlapping. From the maps, Fe, O and Yb appear to be more inside the sample than other elements, as observed from their positive image of the particle under analysis. The EDS spectra show an increase in the intensity of the Yb peaks with an increase in its doping concentration increases. The EDS maps show that the Yb is homogeneously distributed inside the particle, which is being analyzed.

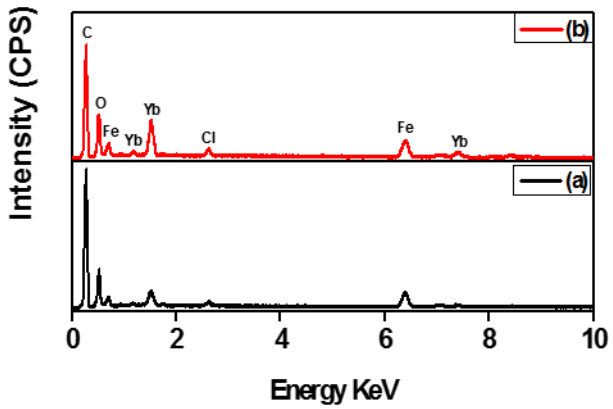

Figure 7. 2 EDS of (a) 0.2mol%Tm:2mol%Yb and (b) 0.2mol%Tm:4mol%Yb.

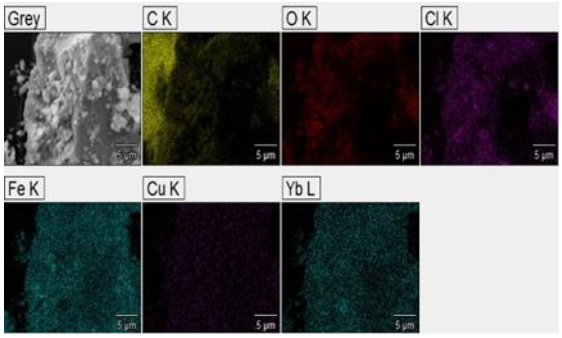

Figure 7. 3 Mapping of 0.2mol%Tm:4Mol%Yb of co-doped α-Fe_2O_3.

The SEM-CL spectra and SEM-CL image were collected by the field-emission scanning electron microscope equipped with a MonoCL4 measurement unit, illustrated in fig 7.1. The CL image and spectra were produced when the electron beam was swept across the defined area by collecting a full emission spectrum per position [18]. The CL emission intensity was high enough for CL imaging, as indicated by the glow in the bright spot. The CL spectra were measured with a PMT 960 detector, and the emission peaks observed correspond to the emission of Tm centered at 364

nm, 468 nm, 680 nm and 806 nm, corresponding to $^1D_2 \rightarrow {}^3H_6$, $^1G_4 \rightarrow {}^3H_6$, $^3f_{2,3} \rightarrow {}^3H_6$ and $^3H_4 \rightarrow {}^3H_6$, respectively.

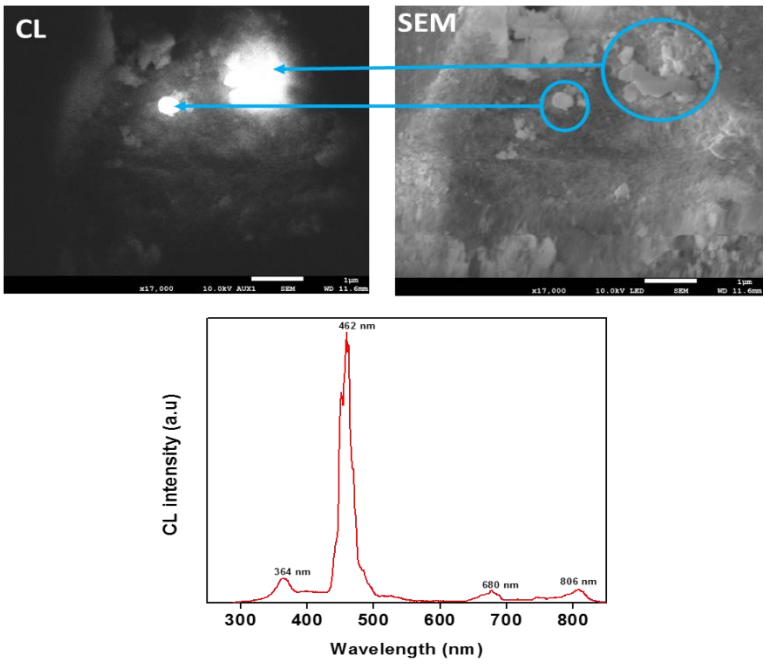

Figure 7. 3 CL images showing the luminescenet feature and spectra showignt the luminescent emission of the Tm:Yb co-doped α-Fe_2O_3.

7.3.3. Optical absorption

The diffuse reflectance spectra were recording using 1050 UV_Vis_NIR absorption spectroscopy, equipped with a BaSO4 integrating sphere. The spectra shown in fig 5(a) indicate that the sample mostly absorbs between 400 and 550 nm, with a second major absorption around between 700 nm and 1000 nm. These two major absorption may be attributed to the band to band absorption and the defect absorption transition of α-Fe_2O_3 [19]. The band at 970 nm in the near infrared is attributed to the Yb^{3+} ion $^2F_{7/2} \rightarrow {}^2F_{5/2}$ transition [20]. The intensity of this peak was observed to increase with an increase in Yb^{3+} concentration. In bio-imaging applications, the absorption of water is low and scattering is the dominant interaction in the optical range of 600 - 1000 nm. However, in this range the incident light can propagate inside highly scattered target up to a few centimeter until the diffused photons are absorbed out of the target. These photons can be re-emitted and collected in the reflectance geometry and can be used for both thin and thick targets

such as newborn and adult heads. However, the reachable depth of collecting photons is limited to less than 4 cm [21].

Figure 4. (b) Shows Kubelka-Munk function transformed from the diffuse reflectance, using (Eq 2):

$$\mathbf{F(R)} = \frac{(1-R)^2}{2R}, \qquad (2)$$

where F(R) is the diffuse reflectance factor that is transformed according to the kubelka-Munk model, from the reflectance R, which is further transformed to the Kubelka-Munk function, as detail by Wood [22]. The band gap was extrapolated from the Kubelka-Munk function plot. The estimated band gap increases from 1.86 eV to 1.97 eV with an increase in Yb^{3+} concentration. From the diffuse reflectance spectra, we observed a blue shift due to quantum confinement.

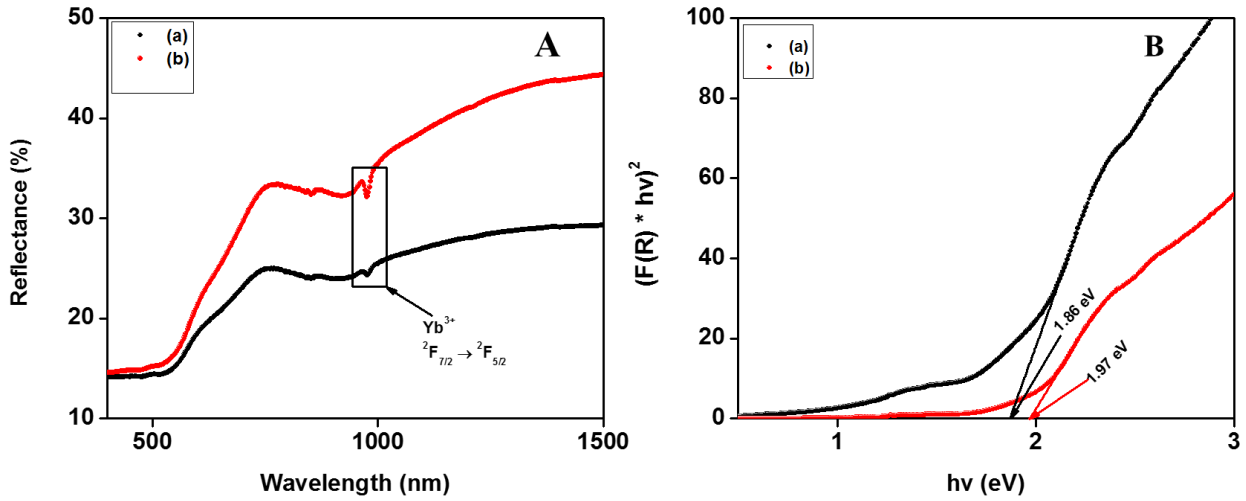

Figure 7. 4 (A) Diffuse Reflectance spectra of (a) 0.2mol%Tm:2mol%Yb and (b) 0.2mol%Tm:4mol%Yb and (B) Band gap extrapolation of (a) 0.2mol%:2mol%Yb and (b) 0.2mol%Tm:4mol%Yb co-doped α-Fe_2O_3

7.3.4. PL Up-conversion

Yb^{3+} ions have been reported to be the best sensitizers for up-conversion luminescence, when paired with Er^{3+}, Ho^{3+} and Tm^{3+} ions. This is due to its absorption cross section that is 9.11 x 10^{-21} cm^{-2} at 980 nm, which is larger than that of other Ln^{3+} ions, and this is attributed to its single excited state energy level ($^2F_{5/2}$), which matches well with the f-f transitions of Tm^{3+}, Ho^{3+}, Er^{3+} etc. [23]. Upon 980 nm laser excitation, Yb^{3+} ions are excited from the ground state $^2F_{7/2}$ level to the excited state $^2F_{5/2}$ level, which is followed by a transfer of energies to the nearby Tm^{3+} ions. The UC emission spectra and the possible mechanism are shown in figure 7.5. Figure 7.5(A) shows the emission from the range 400-850 nm, (b) 400-500 nm, (c) 650 – 750 nm and (d) from 750 – 850 nm. From fig 7.5(A), only the emission around 800 nm is observed and the others are suppressed due to their low intensities. To clearly analyze them we plotted them into spectral ranges of (b), (c), and (d). The PL emission in the visible is displayed by three emission peaks that are observed at 476 nm, 695 nm and 707 nm, which are attributed to $^1G_4 \rightarrow {}^3H_6$, $^3F_2 \rightarrow {}^3H_6$ and $^3F_3 \rightarrow {}^3H_6$ electron transitions, respectively. The $^1D_2$ level of Tm^{3+} is unable to transfer the fourth photon from energy level of Yb^{3+} to the energy of $^1G_4$ level because the population of $^1D_2$ level of Tm^{3+} ions is not restrained [24]. Two emission peaks are observed in the NIR region, a weak band centered about 786 and a strong band centered at 798 nm, attributed to electronic transitions of $^1G_4 \rightarrow {}^3H_6$ and $^3H_4 \rightarrow {}^3H_6$ of the Tm^{3+} ions, respectively. Yb^{3+} absorbs majority of the excitation photons because their excitation cross-section for $^2F_{7/2} \rightarrow {}^2F_{5/2}$ contains the full f-f oscillator strength. The visible emission occurs because the Yb^{3+} ions have no higher-lying excited state than the $^2F_{5/2}$, so the Yb^{3+} absorbed energy, is transferred to Tm^{3+}, which displays the resulting emission [25]. The emission peaks were observed to increase with an increase in Yb^{3+} concentration. We must also mention that the emission peaks were not observed for Tm^{3+} singly doped α-Fe_2O_3 under 980 nm excitation. This could be due to the Tm^{3+} low excitation cross-section at this excitation wavelength (980 nm). It then can be concluded that energy transfer is occurring between Yb^{3+} and Tm^{3+} rare earth ions.

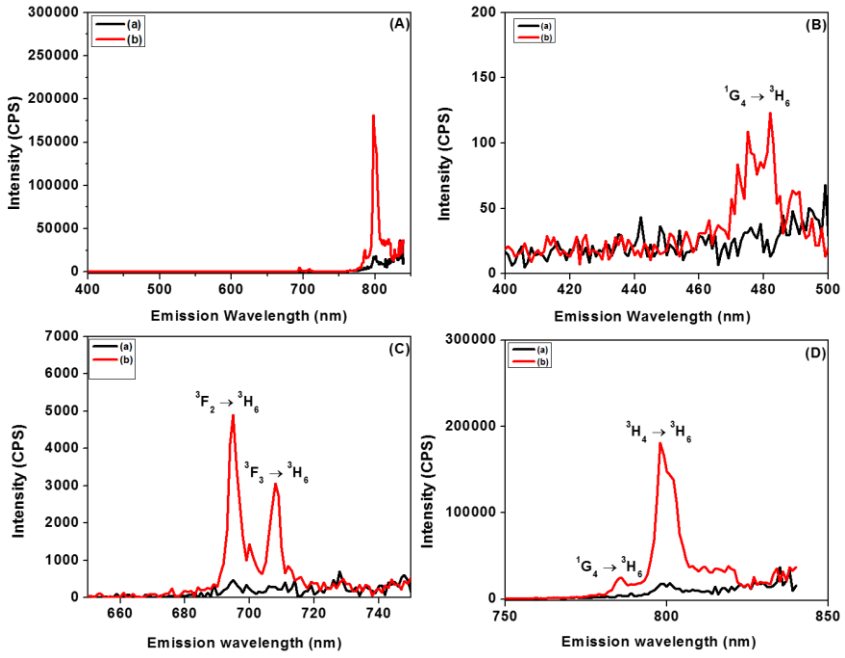

Figure 7. 5 Up-conversion emission spectrum of (a) 0.2mol%Tm:2mol%Yb and (b) 0.2mol%Tm:4mol%Yb with (A) 400-850 nm, (B) 400-500 nm, (C) 600-750 and (D) 750-850 nm.

Fig 7.6 shows the energy levels of Tm^{3+} and Yb^{3+} ions in α-Fe_2O_3 nanoparticles. The 980 nm laser excites the Yb^{3+} ions from the ground sate $^2F_{7/2}$ to the excited state $^2F_{5/2}$, from where energy is transferred to the $^1G_4$, $^3F_2$ and $^3H_5$ energy levels of Tm^{3+} ions. The energy in the latter states of Tm^{3+} ions, is pumped to the highest state, $^1G_4$. The electron relaxation from $^1G_4$ to $^3H_6$, $^3F_3$ to $^3H_6$ and $^3H_4$ to $^3H_6$ levels is radiative and results in emission peaks at 476 nm, 695 nm and 798 nm, respectively. Similar mechanism have been reported by F. Guell et. al. when exciting the Tm^{3+} ions by 940 nm laser, the emissions were from the $^1G_4$ to the $^3H_6$ and $^3F_3$ to $^3H_6$ levels, generating the emission at 476 nm and 650 nm respectively [13]. The lowest $^3H_6$ manifold consist of several stark levels (2n +1 = 7). The lowest stark level stark level comprises of a higher proportion of the density of states due to thermal equilibrium that exist between them. Since the emission could be from any of the stark level, the emission luminescence from the CL have slightly shifted from that of the up-conversion emission[26]. Additionally, the color index for the different emission peaks was determined using the International Commission on Illumination (CIE) coordinate plots. The CIE coordinates are standards reference for defining colors, which are obtained by considering the

different sensitivity of human eye to different colors. By multiplying the spectral power by each of the three color matching functions (X,Y,Z), we can obtain the CIE chromaticity coordinates, whereby, after proper normalization, only two chromaticity coordinates (X,Y) are calculated [27]. The CIE coordinates for the emission peaks of α-Fe_2O_3: Tm^{3+},Yb^{3+} (fig. 8) were (0.13:0.08) (0.12:0.08) for the range, (0.58:0.41) and (d) (0.61: 0.38), for the 400-500 nm, 550-750 nm and 750-8500 nm range, respectively. From the coordinates, it is evident that our material emits blue and red visible colors as observed from UC emission as well.

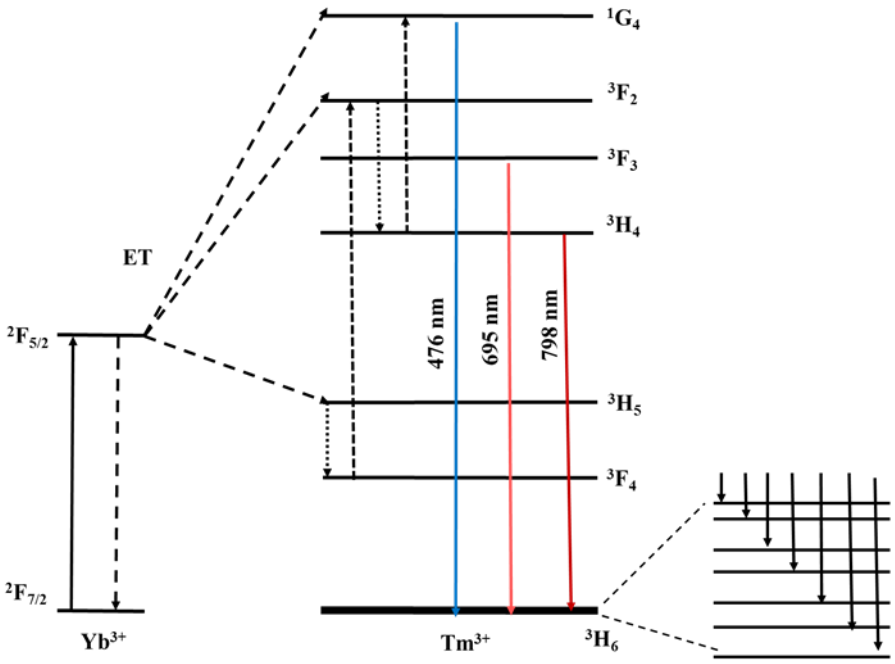

Figure 7.6 Energy transfer mechanism between Tm^{3+} and Yb^{3+} Up-conversion

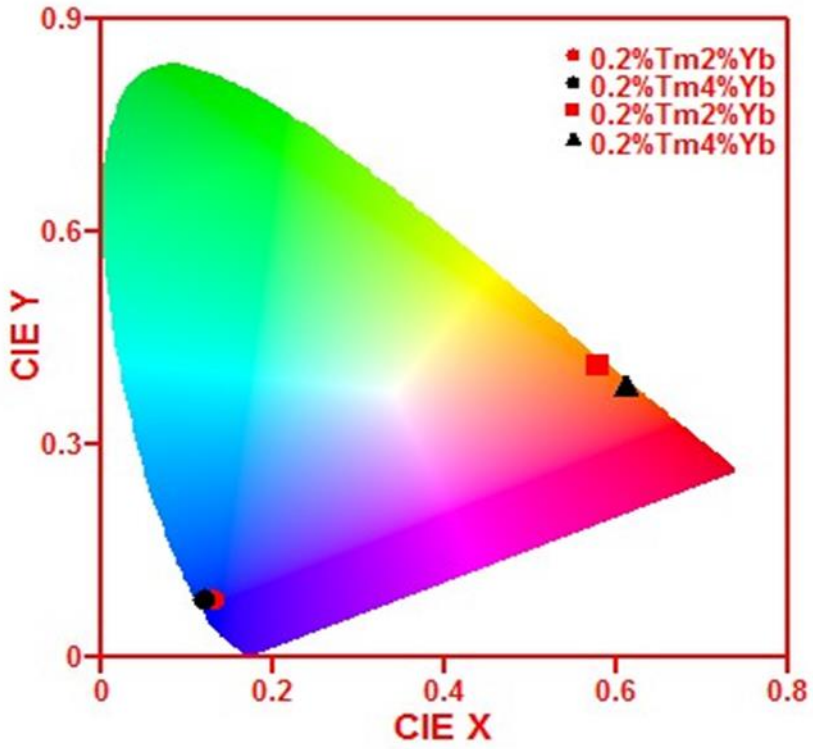

Figure 7.8 CIE chromaticity coordinates

7.4. Conclusion

Tm^{3+} and Yb^{3+} ions were successfully incorporated inside α-Fe_2O_3 host, using the microwave synthesis method. The XRD confirmed the presence of α-Fe_2O_3 phase with some impurities. The elemental analysis indicated the presence of Fe, O and Yb from the final product. The CL spectra showed the down-conversion emission from the Tm^{3+} ions. It was necessary to incorporate Yb^{3+} ions as sensitizers in α-Fe_2O_3:Tm^{3+}, in order to obtain an emission, because the singly doped phosphor was not giving any optical response. The resulting PL emission was observed at 476 nm, 695 nm and 798 nm corresponding to $^1G_4 \rightarrow {}^3H_6$, $^3F_{2,3} \rightarrow {}^3H_6$ and $^3H_4 \rightarrow {}^3H_6$ transitions of Tm^{3+}, respectively, which was induced by energy transfer from Yb^{3+} ions. The visible blue and red emission colors were confirmed by the CIE coordinates. Therefore, this material shows positive optical properties, which are very important for fluorescence imaging application.

Acknowledgements

The authors acknowledge the financial support from the National Research foundation (NRF – Grant no. 106015), Department of Science and Technology for their financial support. We are grateful to the Physics department of the University of the Free State (Bloemfontein campus) for the up-conversion measurements.

References

[1] S. S. Shinde, C. H. Bhosale, and K. Y. Rajpure, "Studies on morphological and electrical properties of Al incorporated combusted iron oxide," *J. Alloys Compd.*, vol. 509, no. 9, pp. 3943–3951, 2011.

[2] P. Mallick and B. N. Dash, "X-ray Diffraction and UV-Visible Characterizations of α-Fe_2O_3 Nanoparticles Annealed at Different Temperature," *Nanosci. Nanotechnol.*, vol. 3, no. 5, pp. 130–134, 2013.

[3] F. S. Freyria, G. Barrera, P. Tiberto, E. Belluso, D. Levy, G. Saracco, P. Allia, E. Garrone, and B. Bonelli, "Eu-doped α-Fe_2O_3 nanoparticles with modified magnetic properties," *J. Solid State Chem.*, vol. 201, pp. 302–311, 2013.

[4] Q. Liu and K. Osseo-Asare, "Synthesis of Monodisperse Al-Substituted Hematite Particles from Highly Condensed Metal Hydroxide Gels," *J. Colloid Interface Sci.*, vol. 231, no. 2, pp. 401–403, 2000.

[5] T. I. Bhuiyan, M. Nakanishi, Y. Kusano, T. Fujii, J. Takada, and Y. Ikeda, "Synthesis, morphology and color tone properties of the lanthanum substituted hematite," *Mater. Lett.*, vol. 61, no. 17, pp. 3774–3777, 2007.

[6] M. S. Dhlamini, G. H. Mhlongo, H. C. Swart, O. M. Ntwaeaborwa, and K. T. Hillie, "Concentration effect of Tm^{3+} on cathodoluminescence properties of SiO_2:Tm^{3+} and SiO_2:Ho^{3+}, Tm^{3+} systems," *Phys. B Phys. Condens. Matter*, vol. 407, no. 10, pp. 1582–1585, 2012.

[7] H. Dong, L. D. Sun, and C. H. Yan, "Energy transfer in lanthanide upconversion studies for extended optical applications," *Chem Soc Rev*, vol. 44, no. 6, pp. 1608–1634, 2015.

[8] G. Chen, H. Qiu, P. N. Prasad, and X. Chen, "Upconversion nanoparticles: Design, nanochemistry, and applications in Theranostics," *Chem. Rev.*, vol. 114, no. 10, pp. 5161–5214, 2014.

[9] L. Yanhong, L. Haiyan, S. Guoyi, and Z. Xing'ao, "Upconversion Luminescence of Er^{3+}, Tm^{3+} and Yb^{3+} co-doped $Gd_3Ga_5O_{12}$ nanocrystals," *J. Wuhan Univ. Technol. Sci. Ed.*, vol. 29, no. 1, pp. 13–18, 2014.

[10] D. A. Simpson, W. E. Gibbs, S. F. Collins, W. Blanc, B. Dussardier, G. Monnom, P. Peterka, and G. W. Baxter, "Visible and near infra-red up-conversion inTm^{3+}/Yb^{3+} co-doped silica fibers under 980 nmexcitation," *Opt. Express*, vol. 16, no. 18, pp. 13781–13799, 2008.

[11] M. A. Hahn, A. K. Singh, P. Sharma, S. C. Brown, and B. M. Moudgil, "Nanoparticles as contrast agents for in-vivo bioimaging: Current status and future perspectives," *Anal. Bioanal. Chem.*, vol. 399, no. 1, pp. 3–27, 2011.

[12] A. Akbarzadeh, M. Samiei, and S. Davaran, "Magnetic nanoparticles: preparation, physical properties, and applications in biomedicine," *Nanoscale Res. Lett.*, vol. 7, no. 1, p. 144, 2012.

[13] F. Güell, R. Solé, J. Gavaldà, M. Aguiló, M. Galán, F. Díaz, and J. Massons, "Upconversion luminescence of Tm^{3+} sensitized by Yb^{3+} ions in monoclinic $KGd(WO_4)_2$ single crystals," *Opt. Mater. (Amst).*, vol. 30, no. 2, pp. 222–226, 2007.

[14] J. Chang, G. Peng, and Q. Wang, "Ytterbium-Codoping in Thulium Doped Silica Fiber," *PIERS Online*, vol. 1, no. level 4, pp. 62–66, 2005.

[15] M. Wegman and M. Scharr, "Synthesis of Magnetic Iron Oxide Nanoparticles Magnetic," Precision Medicine: Tools and Quantitative Approaches, pp. 145-181, 2018

[16] S. A Speakman, "Basics of X-Ray Powder Diffraction," *Basics X-Ray Powder Diffr.*, no. 617, pp. 1–97, 1900.

[17] T. ART, "Basics of X-ray Diffraction," in *Introduction to powder/polyscrystalline diffraction*, pp. 1–22, 1999.

[18] R. L. Nyenge, H. C. Swart, D. Poelman, P. F. Smet, L. I. D. J. Martin, L. L. Noto, S. Som, and O.M. Ntwaeaborwa, "Thermal quenching, cathodoluminescence and thermoluminescence study of Eu^{2+} doped CaS powder," *J. Alloys Compd.*, vol. 657, pp. 787–793, 2016.

[19] J. Wang, W. B. White, and J. H. Adair, “Optical properties of hydrothermally synthesized hematite particulate pigments,” *J. Am. Ceram. Soc.*, vol. 88, no. 12, pp. 3449–3454, 2005.

[20] W. Zheng, H. Zhu, R. Li, D. Tu, Y. Liu, W. Luo, and X. Chen, “Visible-to-infrared quantum cutting by phonon-assisted energy transfer in YPO_4:Tm^{3+},Yb^{3+} phosphors,” *Phys. Chem. C hem. Phys.*, vol. 14, no. 19, pp. 6974–6980, 2012.

[21] M. Alayed and M. Deen, “Time-Resolved Diffuse Optical Spectroscopy and Imaging Using Solid-State Detectors: Characteristics, Present Status, and Research Challenges,” *Sensors*, vol. 17, no. 9, pp. 2115, 2017.

[22] B. J. Wood, “Diffuse Reflectance Spectra and Optical Properties of Some Sulphides and Related Minerals,” *Mineral. Mag.*, vol. 43, no. 5, pp. 509–518, 1979.

[23] M. K. Mahata, H. C. Hofsäss, M. K. Mahata, H. C. Hofsäss, U. Vetter, and U. Vetter, “Photon-Upconverting Materials: Advances and Prospects for Various Emerging Applications,” *Luminescence - an outlook on the phenomena and their applications*, chapter 6, pp. 109-131, 2016

[24] B. Zhou and D. Xia, “Colloidal b-KYF_4:Yb^{3+},Er^{3+}/Tm^{3+} nanocrystals: tunable multicolor up-conversion luminescence from UV to NIR regions,” *RSC Adv.*, vol. 5, pp. 66807–66814, 2015.

[25] C. R. Ronda, *Luminescence: From Theory to Applications*. 2007.

[26] S. D. Jackson, “Cross relaxation and energy transfer upconversion processes relevant to the functioning of 2 μm Tm^{3+}-doped silica fibre lasers,” *Opt. Commun.*, vol. 230, no. 1–3, pp. 197–203, 2004.

[27] T. Passuello, F. Piccinelli, M. Pedroni, M. Bettinelli, F. Mangiarini, R. Naccache, F. Vetrone, J. A. Capobianco, and A. Speghini, “White light upconversion of nanocrystalline Er/Tm/Yb doped tetragonal $Gd_4O_3F_6$,” *Opt. Mater. (Amst).*, vol. 33, no. 4, pp. 643–646, 2011.

Chapter 8: Summary and future work

The aim of this project was to synthesize and study the structural, optical, luminescence, morphological and magnetic properties or trivalent-doped α-Fe_2O_3. Two synthesis methods had been employed (1) sol-gel method which was used for the un-doped, Ho doped and Ho:Yb co-doped α-Fe_2O_3. (2) Microwave synthesis was used for Tm doped and Tm:Yb co-doped α-Fe_2O_3. All these materials were successfully synthesized by both methods and characterized.

The first part of the work was to synthesize pure α-Fe_2O_3, Ho doped and Ho:Yb co-doped α-Fe_2O_3 nanomaterials. The nanomaterials were characterized by, XRD, UV-VIS, PL, TEM, XPS and VSM. The results shows the influence of the dopants on the host matrix. However, no up-conversion emission was observed with these materials.

The second part was to synthesize Tm doped and Tm:Yb co-doped α-Fe_2O_3 nanomaterials by microwave synthesis. XRD, SEM, UV-VIS and VSM were used to characterized the nanomaterials for the structure, morphology as well as magnetic properties. From the Tm doped nanomaterials, the luminescence were intrinsic defects from the host and no emission from Tm was observed. The up-conversion was not observed due to the quenching effect of the host matrix. However, the materials showed very good magnetic properties. The hysteresis loop at room temperature showed a paramagnetic behavior. The magnetization values were observed to be higher than the reported value of the bulk materials (1.2 emu/g). This indicate the improvement of the magnetic properties of this materials which is good for the MRI application.

The CL showed a down-conversion emission from Tm^{3+} centered around 364 nm, 468 nm, 680 nm and 806 nm, corresponding to $^1D_2 \rightarrow {}^3H_6$, $^1G_4 \rightarrow {}^3H_6$, $^3f_{2,3} \rightarrow {}^3H_6$ and $^3H_4 \rightarrow {}^3H_6$, respectively. The peak at NIR was observed to be lower than that from up-conversion, thereby exhibiting a blue emission. The Tm^{3+} and Yb^{3+} co-doped showed up-conversion luminescence from Tm^{3+} ions. The observed up-conversion luminescence is attributed to the energy transfer from Yb^{3+} and Tm^{3+}, which was the main objective of the study. The luminescence spectra showed low intense emission from the Tm^{3+}. We observed the emission transition of Tm^{3+} centered at 479, 690 and 800 nm corresponding to $^1G_4 \rightarrow {}^3H_6$, $^3F_{2,3} \rightarrow {}^3H_6$ and $^3H_4 \rightarrow {}^3H_6$ transitions, respectively. The emission

was dominated by the red color, which lie in the visible range, and can be observed without difficulty in luminescence imaging application.

The proof of concept exposed in this work shows that rare earth Trivalent, can be doped into the α-Fe_2O_3 nanostructures to show an improved up-conversion luminescence. Further investigation of this work is required, to better improve the results. The major findings of this work is that we managed to incorporate the rare earth into the α-Fe_2O_3 host and observed the up-conversion luminescence. The observed luminescence was shown when Tm and Yb were added to the host. Our findings suggest that the synthesized nanomaterials can be used in optical imaging applications, due to their improved luminescence properties.

Future work

From our research finding, there is still more work to be investigated in this subject and are listed below:

- There is a need to optimizing the sol-gel method, especially when doping with rare earth
- To optimize the luminescence properties of the nanomaterials. For the samples synthesized by sol-gel, up-conversion luminescence was not observed. For the microwave synthesized materials, there was up-conversion but with low intensity.
- There is also a need to optimize the structure of these materials. For imaging application, we expect to have spherical samples with sizes ranging between 1 and 40 nm.
- Once the required nanomaterial is optimized, the microscope will be used to image the materials.
- The final step will be to do the bio-imaging in animals with our nanomaterials

Publications

- L.E. Mathevula, L.L. Noto, B.M. Mothudi, M. Chithambo, M.S. Dhlamini, Structural and optical properties of sol-gel derived α-Fe_2O_3 nanoparticles, Journal of Luminescence 192 (2017) 879–887
- L.E. Mathevula, L.L. Noto, B.M. Mothudi, M.S. Dhlamini, Structural and optical properties of α-Fe_2O_3 nanoparticles, influenced by holmium ions, Physica B: Condensed Matter, Physica B 535 (2018) 258–261.

- L.L. Noto, D. Poelman, V.R. Orante-Barrón, H.C.Swart, L.E. Mathevula, R. Nyenge, M. Chithambo, Photoluminescence and thermoluminescence properties of $BaGa_2O_4$, Physica B:CondensedMatter, PhysicaB 535 (2018) 268–271, .
- Luminescence and magnetic properties of Tm^{3+} doped α-Fe_2O_3 nanomaterials (In Preparations)
- Up-conversion luminescence properties of Tm^{3+} and Yb^{3+} co-doped α-Fe_2O_3 nanoparticles (Ready for submission)

Conference contribution

- **FluoroFest workshop, 29 June – 1 July 2015, Starnberg (Munich), Germany.** ***Optical properties of sol-gel derived α-Fe_2O_3 Nanoparticles (Poster presentation)***
- **NanoAfrica Conference, 4 – 6 April 2016, University Of South Africa, South Africa.** ***Structural and optical properties of sol-gel derived α-Fe_2O_3 nanoparticles. (Oral presentation)***
- **National Research Foundation Symposium , 27 June 2016, Council for Scientific and Industrial Research, South Africa**
- **The 61st annual conference of the SA institute of physics, 4 – 8 July 2016, University of Cape Town, South Africa.** ***Structural and optical properties of rare earth doped α-Fe_2O_3*** **nanoparticles (Oral presentation)**
- **Nanoscience's young researchers symposium, 18 November 2016, MINTEk, South Africa**
- **7th South African Conference on Photonic Materials, 27 – 31 March 2017, Amanzi Game Reserve, South Africa.** ***Structural and optical properties of α-Fe_2O_3 nanoparticles, influence by holmium ions (Poster presentation)***
- **Nanoscience's young researchers symposium, 20 October 2017, Tshwane University Of Technology, South Africa**